# ABSTRACT


| | |
|---|---|
| Title of Dissertation: | UNDERSTANDING THE RELATIONSHIPS BETWEEN ARCHITECTURE, CHEMISTRY, AND ENERGY RELEASE OF ENERGETIC NANOCOMPOSITES |
| | Jeffery Brandon DeLisio, Doctor of Philosophy, 2017 |
| Dissertation directed by: | Professor Michael R. Zachariah, Department of Chemical and Biomolecular Engineering and Department of Chemistry and Biochemistry |



Energetic nanocomposites are a class of reactive material that incorporate nanosized materials or features in order to enhance reaction kinetics and energy densities. Typically, these systems employ metal nanoparticles as the fuel source and have demonstrated reactivities orders of magnitude larger than more traditionally used micron-sized metal fuels. One drawback of using nanosized metals is that the nascent oxide shell comprises a significant weight percent as the particle size decreases. This shell also complicates the understanding of oxidation mechanisms of nanosized metal fuels.

In this dissertation, I apply a two-fold approach to understanding the relationships between architecture, chemistry, and energy release of energetic nanocomposites by 1) investigating alternative metal fuels to develop a deeper understanding of the reaction mechanisms of energetic nanocomposites and 2)

creating unique microstructures to tailor macroscopic properties allowing for customizability of energetic performance. In order to accurately study these systems, new analytical techniques capable of high heating rate analysis were developed.

The oxidation mechanisms of tantalum nanoparticles was first probed using high heating rate TEM and Temperature-Jump Time-of-Flight Mass Spectrometry (T-Jump TOFMS) and shell crystallization was found to plan an important role in the mechanism. An air-sensitive sample holder was developed and employed to analyze the decomposition and oxidation of molecular aluminum compounds, which theoretically can achieve similar energy release rates to monomolecular explosives in addition to much higher energy densities. In order to obtain simultaneous thermal and speciation data at high heating rates, a nanocalorimeter was integrated into the TOFMS system and measurements were performed on Al/CuO nanolaminates to probe the effect of bilayer thickness on energy release. An electrospray based approach to creating energetic nanocomposites with tunable architectures is also described. An in depth study on the electrospray synthesized nAl/PVDF thin film reaction mechanism was performed using T-Jump TOFMS. The nAl/PVDF system was also studied using a Molecular Beam Sampling Time-of-Flight Mass Spectrometer designed and built primarily to investigate the reaction mechanisms of energetic nanocomposites at 1 atm in both aerobic and anaerobic environments.

# UNDERSTANDING THE RELATIONSHIPS BETWEEN ARCHITECTURE, CHEMISTRY, AND ENERGY RELEASE OF ENERGETIC NANOCOMPOSITES

by

Jeffery Brandon DeLisio

Dissertation submitted to the Faculty of the Graduate School of the
University of Maryland, College Park, in partial fulfillment
of the requirements for the degree of
Doctor of Philosophy
2017

Advisory Committee:
Professor Michael R. Zachariah, Chair
Professor Zhihong Nie
Professor Bryan W. Eichhorn
Professor Efrain E. Rodriguez
Professor Peter B. Sunderland, Dean's Representative

# Dedication

To my amazing fiancée, Shana, for your love, always believing in me, and being my rock. To my parents, sister, grandparents, and friends, for your patience and support through this process.

# Acknowledgements

I am extremely grateful for everyone who helped make this dissertation a possibility. I would like to first thank Dr. Michael Zachariah for his guidance, support, and patience throughout my studies. I would also like to thank my current and former lab mates, and in particular, Dr. Garth Egan, Dr. Wenbo Zhou, Dr. Guoqiang Jian, Phillip Guerieri, Rohit Jacob, Carlos Rodriguez, Xizheng Wang, Tao Wu, Haiyang Wang, and Miles Rehwoldt for our discussions and your assistance. In addition, thank you to my many collaborators, in particular, Dr. Gregory Young, Dr. Dennis Mayo, Dr. Feng Yi, Dr. David LaVan, and Dr. Sz-Chian Liou and Dr. Wen-An Chiou of the UMD AIM Lab. This work would not have been possible without funding from our sponsors, the Army Research Office, the Airforce Office of Scientific Research, the Office of Naval Research, and the Defense Threat Reduction Agency.

Finally, I would like to acknowledge my advisory committee, Professor Zhihong Nie, Professor Efrain Rodriguez, Professor Bryan Eichhorn, and Professor Peter Sunderland.

# Table of Contents

# List of Tables

# List of Figures

# List of Abbreviations

| | |
|---|---|
| TNT | Trinitrotoluene |
| RDX | Cyclotrimethylenetrinitramine |
| MICs | Metastable Intermolecular Composites |
| MTV | Magnesium/Teflon/Viton |
| TEM | Transmission Electron Spectroscopy |
| DTEM | Dynamic TEM |
| PIR | Pre-Ignition Reaction |
| PVDF | Polyvinylidene Fluoride |
| PFPE | Perfluoropolyther |
| TGA | Thermogravametric Analysis |
| DSC | Differential Scanning Calorimetry |
| T-Jump | Temperature Jump |
| TOFMS | Time-of-Flight Mass Spectrometer |
| MCP | Microchannel Plate |
| ASSH | Air Sensitive Sample Holder |
| KF | Klein Flansche |
| PEEK | Polyether Ether Ketone |
| DSA | Dynamic Signal Acquisition |
| Na-TZ | Sodium Azotetrazolate |
| AP | Ammonium Perchlorate |
| RTOFMS | Reflectron Time-of Flight Mass Spec |
| MBMS | Molecular Beam Sampling Mass Spec |

| | |
|---|---|
| nAl | Aluminum Nanoparticles |
| nTa | Tantalum Nanoparticles |
| MEMS | Microelectromechanical Systems |
| NC | Nitrocellulose |
| SEM | Scanning Electron Microscopy |
| XRD | X-Ray Diffraction |
| E-gun | Electron Gun |

# Chapter 1: Introduction

## *1.1. Energetic Materials*

Energetic materials is a broad term describing compounds that release large amounts of stored chemical energy when an activation energy barrier is overcome. They are most commonly used for explosive, propellant, pyrotechnic, and fuel applications. Energy release is typically facilitated through the oxidation of a fuel where reaction kinetics are closely related to the distance between the fuel and oxidizer. To maximize reaction kinetics, characteristic reaction distance can be minimized by having both the fuel and oxidizer contained in a single molecule. This is referred to as a monomolecular energetic material where carbon and hydrogen are typical fuels that react with oxygen within the molecule.[1] Two examples of commonly used monomolecular energetic materials are trinitrotoluene (TNT) and cyclotrimethylenetrinitramine (RDX).[2]

Composite energetic materials follow a heterogeneous reaction mechanism where the fuel and oxidizer are not part of the same molecule. One of the earliest employed composite energetic materials is black powder, which was first described in texts from the 11$^{th}$ century, and consists of a physical mixture of charcoal and sulfur as the fuel and potassium nitrate as the oxidizer.[3] One advantage of composite energetic materials is that alternative fuel sources, such as metals, can be employed.[4] As shown in Figure 1, metal fuels have much higher energy densities on a per mass and per volume basis compared to standard monomolecular energetic materials.[5]

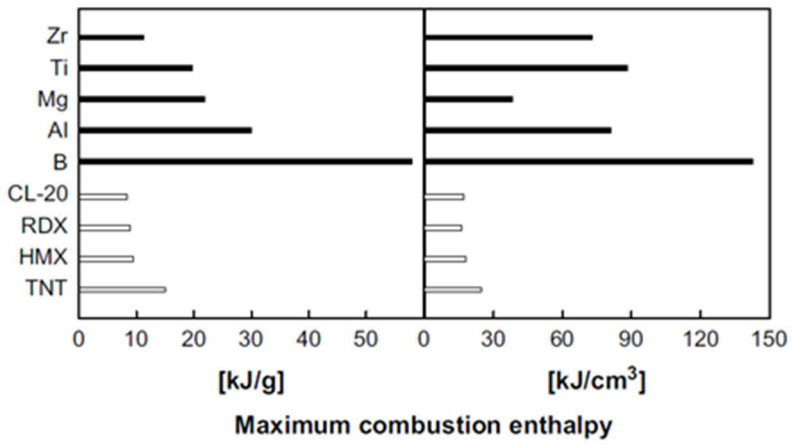


***Figure 1.1.*** *Comparison of the maximum combustion enthalpies on a per mass and per volume basis for commonly used metal fuels and organic energetic materials. Reprinted from Progress in Energy and Combustion Science, 35, Dreizin, E. L., Metal-based reactive nanomaterials, 147-167, 2009.[5]*

Of all the metal fuels listed in Figure 1.1, aluminum has been the most extensively studied due to its low cost, favorable energy density, and ignition characteristics. Aluminum has been added to numerous types of rocket propellants and pyrotechnic mixtures. Most commercial and defense applications use micron sized aluminum particles such as in the HTPB/AP/Al propellant formulation.[6] The oxidation of aluminum with pure molecular oxygen has the greatest theoretical energy output of any oxidizer as shown in the equation below:

$$4Al + 3O_2 \rightarrow 2Al_2O_3$$

This reaction has a theoretical maximum energy output of -830 kJ/mol, but the kinetics of this reaction are very slow. Though the energy density of fuel is high, the overall density of the system is low because oxygen is a gaseous reactant. Very high pressures are needed to speed up the reaction making the system less than ideal for many applications.

Initiation of these reactions has previously been enhanced by adding solid oxidizers to the system. These systems typically have adiabatic flame temperatures in the 2000 K to

3000 K range and large energy densities.[7] A generic metal/metal oxide reaction would mirror the following:

$$A + \frac{y}{x}BO_x = \frac{y}{x}B + AO_y + Q$$

where $Q$ is the large amount of heat released, $A$ and $B$ are two different metals, and $AO_y$ is a more stable metal oxide than $BO_x$. The intense exothermic metal/metal oxide reaction, commonly referred to as a thermite reaction, was patented in 1895 and was commercially applied starting in 1899 in the welding of train tracks. This reaction is self-propagating once the ignition temperature is reached. As stated above, when compared to commonly used monomolecular energetic materials such as TNT and RDX, metal fuels have much higher specific energy densities, but these reactions are kinetically limited.[5] Monomolecular energetic compounds contain a fuel and oxidizer within the same molecule whereas metal fuels depend on an outside source of oxygen. This greatly slows down these heterogeneous reactions making them less ideal for explosive, propellant, and pyrotechnic applications. However, decreasing the particle size of the fuel and oxidizer in metal fuel based systems can create more intimate contact with fuel and oxidizer particles and help to speed up the inherently slow energy release of these systems.[8]

### *1.2. Energetic Nanocomposites*

The first experiments showing benefits from nanosized metal fuels in relation to micron sized particles occurred in 1995.[9] The limiting factor in the oxidation of metal fuels is the diffusion of species between the fuel and oxidizer. In the case of nanosized components, their high specific surface area and decreased diffusion distances result in a drastic increase in reaction kinetics. For example, thermites composed of nanosized metals and metal oxides have shown reaction rates ~1000 times faster than micron sized thermites

in addition to significantly decreased ignition temperatures.[4, 10, 11] These materials have been referred to as metastable intermolecular composites (MICs), superthermites, nanothermites, and nanocomposite thermites.

As stated above, traditional thermite systems employ a metal oxide as the oxygen source. Recent work has shown increased performance using oxysalts such as potassium periodate ($KIO_4$) and potassium persulfate ($K_2S_2O_8$) in nanothermite systems.[12-14] Oxysalt containing systems have previously employed micron scale aluminum with an ammonium perchlorate ($NH_4ClO_4$) oxidizer for solid rocket propellant applications.[6] More recently, biocidal applications have targeted this class of energetic nanocomposites has been targeted for biocidal applications due to its combined pressurization rates, high reaction temperatures, and biocidal agent release (ex: release of iodine in iodine containing oxysalts).[13, 15, 16]

While it is most common for energetic nanocomposites to employ oxygen containing oxidizers, fluorine containing compounds such as polytetrafluoroethylene (PTFE), also known as Teflon, can also be employed.[17-20] The magnesium/Teflon/Viton (MTV) composite has a high reaction enthalpy of -1438 kJ/mol and has been used for aerial decoy flare applications.[17] Aluminum/fluoropolymer based energetic composites are of particular interest for propellant applications because the fluoropolymer can act as both an oxidizer and a binder to give the fuel mechanical integrity.[21]

### *1.3. Nanoparticle Oxidation Mechanisms*

Various mechanisms of initiation/oxidation in nanothermite systems have been previously proposed, but conclusive models on how a metal oxide will perform have not

yet been developed. Although many different thermites have been investigated throughout history, there has been no viable method to accurately predict the ignition temperature for a new metal/metal oxide composition. Previous work has studied whether gas phase oxygen is a pre-requisite for ignition, and it seems to be dependent on the oxidizer.[22] In particular, most research has focused on understanding the oxidation of aluminum nanoparticles. The oxidation mechanism of aluminum nanoparticles is complicated by the nascent 2-5 nm thick $Al_2O_3$ shell surrounding the particle. The presence of this shell may explain the heating rate dependence on the oxidation of aluminum nanoparticles.[23]

The oxidation of Al nanoparticles can occur through three generalized pathways as depicted in Figure 1.2.

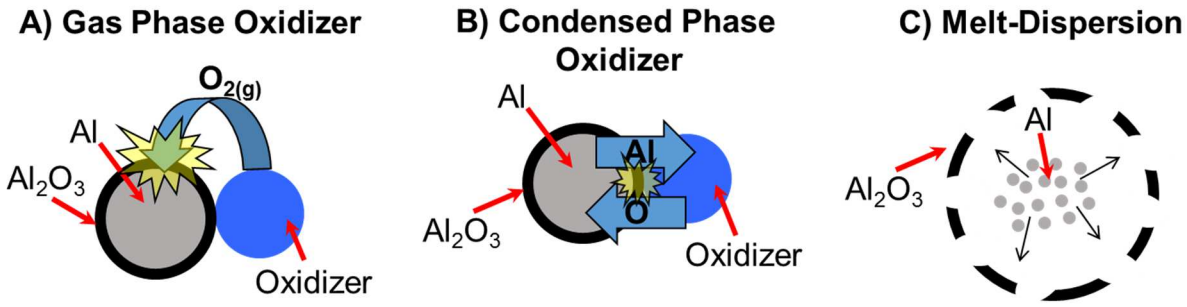


***Figure 1.2.*** *Cartoon of nanoparticle oxidation mechanisms proceeding via a gas phase oxidizer (A), condensed phase oxidizer (B) and melt dispersion (C).*

The oxygen transfer mechanism in Al based systems is typically thought to be dependent on the properties of the employed oxidizer.[22] A two-stage reaction mechanism in which the oxidizer first decomposes, releasing gaseous $O_2$ that goes on to oxidize Al is illustrated in Figure 1.2A. Many Al based energetics that contain oxysalts are proposed to react via this mechanism as their reactivity is severely reduced in low pressure environments where oxygen can rapidly escape the reaction front.[12] In Figure 2B, a single step initiation occurs through the condensed phase transfer of oxygen to the Al. This has been experimentally observed in aluminum based nanothermites where a reactive

sintering based mechanism is apparent in high heating rate TEM studies.[24] This reaction mechanism also helps to explain the lower than expected energy release rates for nanoaluminum. The enhanced surface area of aluminum nanoparticles is effectively reduced due to sintering of aluminum nanoparticles prior to combustion. Experimental studies using high heating rate dynamic TEM (DTEM) have shown that sintering can happen much faster than combustion timescales validating pre-reaction sintering of nanoaluminum.[25, 26]

Ignition via gas or condensed phase oxygen transfer requires either outward diffusion of Al or the inward diffusion of oxygen through the $Al_2O_3$ shell as depicted in Figure 1.2A and 1.2B. Diffusion coefficients for bulk $Al_2O_3$ are too low to explain the reaction rates observed in aluminum nanothermites, but phase changes of the oxide shell during rapid heating may be a contributing factor to the ignition mechanism.[27] In addition, theoretical models have shown that intrinsic electric fields may accelerate outward aluminum diffusion through the oxide shell during rapid heating.[28]

Figure 1.2C depicts aluminum oxidation via the melt-dispersion mechanism, which is theorized to only occur at high heating rates. This theory states that pressure build-up from the melting of the constrained aluminum core results in the fracturing of the $Al_2O_3$ shell and spallation of molten Al explaining the high burn rates.[23, 29] Melt-dispersion has recently been challenged by the lack of visible evidence of shell rupturing during rapid heating of aluminum nanoparticles in high heating rate TEM studies.[24, 25]

Previous studies have shown that the nanoaluminum's $Al_2O_3$ shell plays a unique role in the Al/fluoropolymer reaction mechanism. The most extensively studied Al/fluoropolymer system is the Al/PTFE (Teflon) system. In this system, a pre-ignition

reaction (PIR) has been observed and is thought to play an important role in the oxidation mechanism.[18] The PIR for this system arises from an exothermic reaction between the fluorine in the PTFE and the $Al_2O_3$ passivation shell. Studies have shown increased exothermicity of the PIR with decreased particle sizes and high heating rates.[18, 30] A PIR has also been observed in the Al/perfluoropolyther (PFPE) and Al/$I_2O_5$ systems.[31, 32] Probing the importance of the PIR in these systems at high heating rates requires the use of custom-built instrumentation, as described in Chapter 2. In Chapter 9, I explore the influence of a PIR in the reaction mechanism of an Al/polyvinylidene fluoride (PVDF).

Although numerous studies have investigated the reaction of nanoaluminum with various oxidizers, it is not the only commercially available nanosized metal fuel. Investigating fuels with different properties can help determine what is going on in these reactions and also investigate how microstructure effects the reaction mechanism of the system. In Chapter 3, I examine the oxidation of tantalum nanoparticles and nanothermites because of their similar particle morphology to nanoaluminum. However, these particles have much higher melting temperatures.

### *1.4. Molecular Aluminum Compounds*

As stated above, decreasing the particle size drastically enhances the reactivity of energetic nanocomposites. Unfortunately, this enhanced reactivity comes at the cost of decreased energy output on a per mass basis. This is due to the nascent oxide shell of metal fuels making up a significant portion of the particle's mass as the primary particle size is decreased. One approach to decreasing particle size is by creating near zero oxidation state molecular aluminum clusters. Theoretically, this class of compounds can react at speeds

on the order of traditional monomolecular explosives, in addition to much higher energy densities due to the incorporation of metal atoms in the molecule.

Aluminum has two thermodynamically stable oxidation states, 0 and +3. Molecular aluminum compounds take advantage of the metastable monovalent oxidation state of aluminum ($Al^{+1}$). Aluminum halide solutions (AlX; X = Cl, Br, I) are typically used as the starting material to create low-valent aluminum clusters.[33] However, while various Al cluster materials have been successfully synthesized, these materials are extremely sensitive to air and moisture and have very low production yields.[34] These drawbacks make analysis of molecular Al compounds challenging and evaluating their performance in actual energetic formulations borderline impossible with current analysis methods. New analytical techniques are needed to develop a deeper understanding of this class of materials and to evaluate their viability in practical applications. In Chapter 2, I discuss a new technique for analyzing air/moisture sensitive compounds at high heating rates representative of combustion timescales. The results of these experiments are shown in Chapters 4 and 5, while Chapter 5 also uses this technique to evaluate the effectiveness of coatings on the preservation of Al clusters exposed to ambient conditions.

### *1.5. Microstructure of Energetic Nanocomposites*

One way of enhancing the bulk reactivity of energetic nanocomposites is through tailoring the microstructure of the composite. One of the simplest examples in microstructure effecting reactivity is in the study of nanothermites where the density of the composite has a strong effect on burn speed with less dense powders burning much more rapidly. Characterizing the effects of microstructure can also deepen the understanding of reaction mechanisms of energetic nanocomposites on a broader scale. A laminated

composite is a simple microstructure that can be used to investigate the relationship between interfacial area and reactivity. Laminated composites composed of reactive materials with nanoscale features are commonly referred to as reactive nanolaminates. These composites are typically created using sputter deposition methods that have highly controlled deposition rates.

Various types of reactive nanolaminates have been developed that utilize alloying or reduction/oxidation reactions between the individual layers.[35-38] Two of the most common systems are Al/Ni and Al/CuO reactive nanolaminates. Figure 1.3 shows cross-sectional images of magnetron sputtered Al/CuO multilayers.

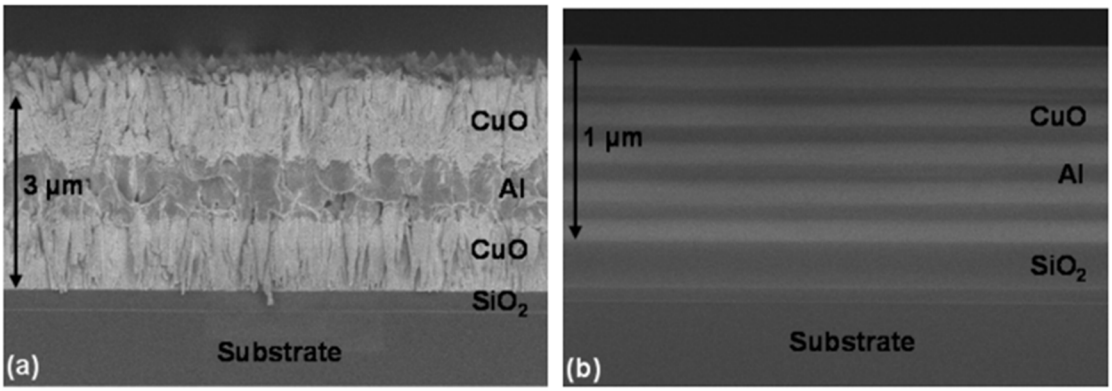


***Figure 1.3.*** *SEM cross-section images of magnetron sputtered multilayers. (A) 3 layers CuO (1 µm)/Al (1 µm) /CuO (1 µm). (B) 10 layers of CuO (100 nm)/Al (100 nm). Reprinted from the Journal of Applied Physics, 108, 8, Rossi, C.; Salvagnac, L.; Conedera, V.; Esteve, A., Multilayered Al/CuO thermite formation by reactive magnetron sputtering: Nano versus micro, 2010.[39]*

The Al/CuO reaction mechanism proceeds at different rates depending on both the stoichiometry and bilayer thickness demonstrating how the microstructure of the nanocomposite can be tailored for a specific application.[39] Understanding the chemistry at the interfaces is vital to understanding the mechanism of oxygen transfer during reaction. Typically, these materials are studied using standard thermogravimetric analysis and differential scanning calorimetry (TGA/DSC) techniques that are only capable of slow

heating rate analysis. Unfortunately, slow heating rate analytics do not accurately represent combustion events and thus new analytical techniques capable of analyzing these reaction mechanisms at relevant timescales are needed. Chapter 2 describes such a technique that is capable of simultaneous temporal speciation and thermal analysis at high heating rates. In Chapter 6, I apply this technique to the study of sputter deposited Al/CuO nanolaminates like those in Figure 1.3.

More intricate microstructures have been created using techniques such as chemical etching and 3D printing.[40-42] Figure 1.4 shows two examples of architectures that have demonstrated enhanced combustion properties of energetic nanocomposites.

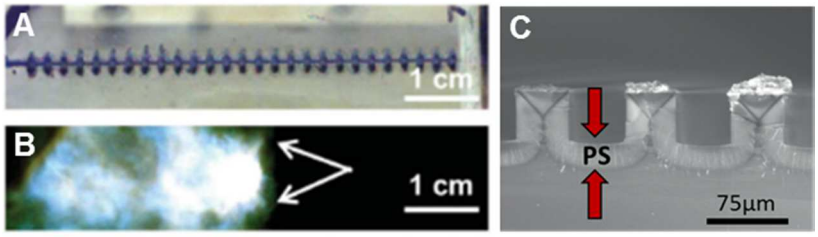


***Figure 1.4.*** *3D printed perpendicular hurdles coated with Al/CuO nanothermite before (A) and during (B) combustion.[40] Cross-sectional view of parallel channels with porous silicon film after hydrofluoric acid etch (C).[43] Reprinted from Advanced Materials, 28, Sullivan, K. T.; Zhu, C.; Duoss, E. B.; Gash, A. E.; Kolesky, D. B.; Kuntz, J. D.; Lewis, J. A.; Spadaccini, C. M., Controlling Material Reactivity Using Architecture, 2016 and Combustion and Flame, 161, Piekiel, N. W.; Morris, C. J.; Currano, L. J.; Lunking, D. M.; Isaacson, B.; Churaman, W. A., Enhancement of on-chip combustion via nanoporous silicon microchannels, 2014.*

Figure 1.4A and 1.4B, show 3D-printed perpendicular hurdles coated with Al/CuO nanothermite that could be tailored to decrease propagation velocities below 50% or increase them by 300% based on the printed architecture.[40] The etched porous silicon channels depicted in Figure 4C enhanced propagation speeds up to 1.2 km/s faster than similar neat porous silicon films.[42] A maximum propagation speed of 3660 m/s was recorded, which is the highest reported flame speed of this class of materials to date.[42]

In Chapter 7, I describe an electrospray based deposition method used to create unique microstructures. This work was done collaboratively, mainly with visiting students in the Zachariah lab. Chapter 8 discusses the reaction mechanism of an Al/fluoropolymer thin film created using this technique, while Chapter 9 explores the effect of the combustion environment and the effect of additives in the film on the reaction mechanism.

### *1.6. Research Plan*

The work described in this dissertation takes a two-fold approach to understanding the relationships between architecture, chemistry, and energy release of energetic nanocomposites by 1) investigating alternative metal fuels to develop a deeper understanding of the reaction mechanisms of energetic nanocomposites and 2) creating unique microstructures to tailor macroscopic properties allowing for customizability of energetic performance. While pursuing both of these goals, one major point of emphasis has been to make sure the employed analytical techniques will accurately probe what happens during combustion to further the understanding of these reaction mechanisms. Chapter 2 will outline the new analytical techniques developed to achieve these goals. Chapters 3-5 investigate the oxidation mechanisms of tantalum and molecular aluminum clusters while Chapters 6-9 focus on creating and studying unique microstructures.

# Chapter 2: High Heating Rate Experimental Methods

*"It doesn't matter how beautiful your theory is, it doesn't matter how smart you are. If it doesn't agree with experiment, it's wrong."*

*-Richard Feynman*

*Summary*

In order to properly study the reaction mechanisms of energetic nanocomposites, high heating rate analytics are needed. One recently developed commercial technique, a TEM/SEM based system capable of *in situ* heating at rates up to $10^6$ K/s, is discussed in this chapter. However, the lack of commercial systems capable of high heating rates and relevant measurement timescales has led to the creation of various home-built systems used to study these reactions. The previously employed T-jump TOFMS technique has a comparatively large error in the temperature measurement and the inability to gain information on the energetics of reaction. Another limitation of the current system is that the sample is held on a thin platinum wire coated under ambient conditions and ignited in the low pressure environment of the TOFMS. Two new modifications to the T-Jump TOFMS system, creation of an air-sensitive sample holder and integration of a nanocalorimeter, and one entirely new home-built instrument, a molecular beam sampling TOFMS, are described in this chapter that will overcome these boundaries and add more functionality to TOFMS based analysis.

## *2.1. High Heating Rate Analytics*

As mentioned in Chapter 1, the reaction mechanism of aluminum containing energetic nanocomposites is highly dependent on heating rate.[1, 2] Therefore, it is important that experimental methods simulate heating rates that occur during combustion events. Slow heating rate analytics such as traditional thermogravimetric analysis (TGA)

and differential scanning calorimetry (DSC) still have their place in examining properties such as thermal stability of a system and can be used to help describe some mechanistic processes, but high heating rate analytics are still a necessity in the deeper understanding of these reaction mechanisms.

### *2.1.1. Protochips E-Chips*

Protochips Inc. has recently developed a thermal E-chip capable of rapidly heating samples at high heating rates inside of a TEM or SEM. These chips can reach a maximum temperature of 1473 K at heating rates up to $10^6$ K/s. The Aduro style thermal E-chip can be used with either a Protochips TEM sample holder or SEM stage as shown in Figure 2.1.

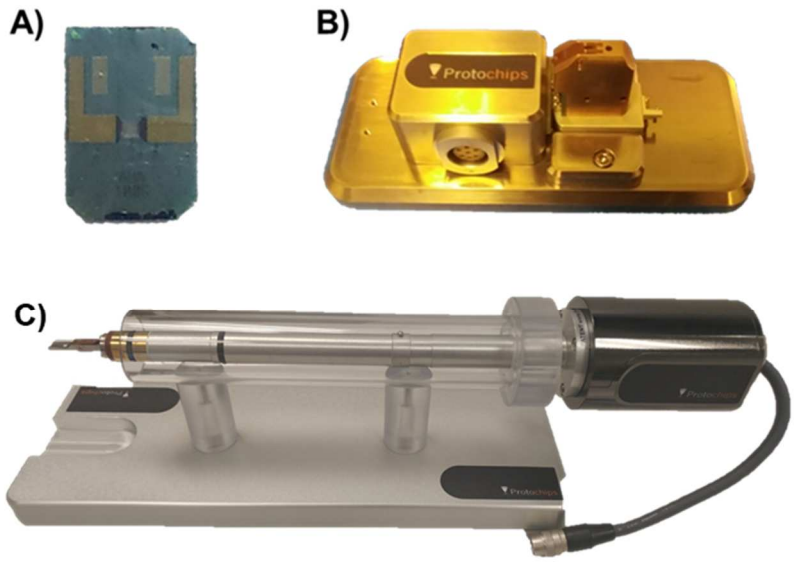


***Figure 2.5.*** *Protochips Aduro E-chip (A), SEM heating stage (B), and TEM heating holder (C).*

The E-chips are joule heated using a DC power supply and can be purchased with either a silicon nitride or carbon film. Detailed information on this system can be found on the Protochips Inc. website.

Previously, our group used this technique to probe the initiation of reactions in nanoaluminum based thermites at high heating rates.[3] Samples were rapidly heated within the vacuum environment of a TEM and particles before and after heating were imaged. The results of this work support the diffusion based mechanism of aluminum oxidation in nanothermite systems. In Chapter 3, a similar study was performed investigating the reaction mechanism of tantalum based nanothermites. Customized E-chips were purchased from Protochips that were calibrated in both 1 atm of air and under vacuum to allow for imaging of tantalum nanoparticles before and after rapid heating in an aerobic environment. Silicon nitride based chips were used for this study as they can reach a higher maximum temperature than carbon film without undergoing oxidation in aerobic conditions. A detailed procedure for performing high heating rate TEM experiments can be found in Appendix A.

### *2.2. Temperature Jump (T-Jump) Ignition*

Throughout this dissertation, the temperature jump (T-Jump) ignition method was employed in various ways as described in subsequent sections. Using this technique, heating rates of up to 5 x $10^5$ K/s are achieved by joule heating a thin (76 μm diameter) platinum (Pt) filament. The filament (~8-12 mm in length) is soldered to two copper leads connected to a custom-built DC power supply capable of producing a ~2-20 ms high current pulse. This DC pulse resistively heats the Pt filament to a maximum temperature of ~1200 $^{o}$C. The temporal voltage and current during heating can be recorded using an oscilloscope to measure the resistance of the wire during heating. The time resolved wire temperatures can be calculated from this resistance data using the Callendar-Van Dusen equation, which relates resistance and temperature of a Pt filament.[4] In this dissertation,

samples were coated on T-Jump filaments by either pipetting suspended particles or directly electrospraying a composite onto the filament. The electrospray deposition technique is discussed, in detail, in Chapter 7.

T-jump ignition can be coupled with other analytical techniques to further probe reaction mechanisms. To determine the ignition temperature of an energetic nanocomposite, high-speed videography (Phantom v12.0) is used to measure the time in which ignition occurs. The ignition temperature is defined as the wire temperature at this time from the T-Jump data. Typically, a camera resolution of 256x256 was used allowing for a frame rate of 67,000 fps. The camera and T-Jump power supply are triggered simultaneously using an external pulse generator allowing for synchronization of optical and wire temperature data. Ignition temperatures can be recorded in a multitude of different environments using this technique. The sample chamber can be evacuated and re-filled in argon to measure anaerobic ignition temperatures. In addition, the sample chamber can also be pressurized to investigate the effect of gas phase species on the ignition mechanism.

### *2.3. Temperature Jump Time-of-Flight Mass Spectrometry (T-Jump TOFMS)*

The gas phase species released during the course of heating can be analyzed using mass spectrometry. Temperature jump time-of-flight mass spectrometry (T-Jump TOFMS) integrates the aforementioned T-Jump heating technique with a R. M. Jordan style linear time-of-flight mass spectrometer. A window opposite the T-Jump probe allows for high speed imaging coupled T-Jump ignition experiments to be performed within the TOFMS. This specific type of mass spectrometry is employed because these systems can be pulsed at high rates (10 kHz) allowing for sufficient temporal resolution between spectra. A schematic of this system is shown in Figure 2.2.

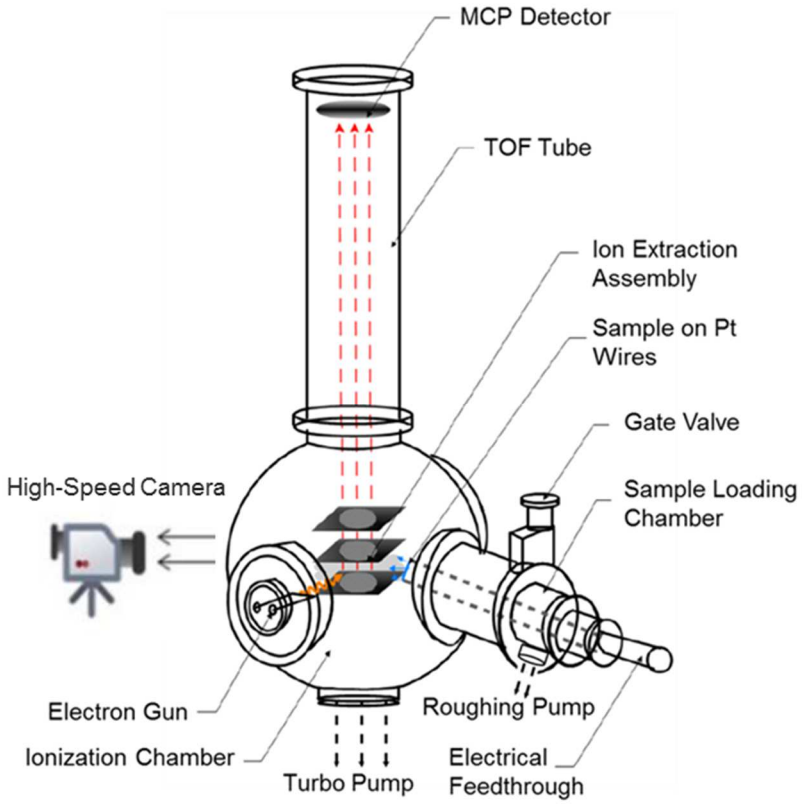


***Figure 2.6.*** *Schematic of T-Jump TOFMS. This figure is a modified version of a figure in reference [5].*

This system functions through the ionization of gas phase species produced during rapid heating within the ionization/extraction region of the TOFMS. Gases are ionized by an electron gun, typically operating at 70 eV and 1 mA. An "electronic gate" is pulsed at 10 kHz, accelerating ions into the electric field-free region (flight tube) of the TOFMS every 100 µs. Ions are detected using a microchannel plate detector (MCP) and data is recorded on an oscilloscope operating in sequence mode (1 full MS per sequence) at a sampling rate of 100 MS/s. The following equation is used to correlate an ion's time of flight to its mass-to-charge ratio:

$$\frac{m}{z} = Kt^2$$

where $\frac{m}{z}$ is the mass-to-charge ratio of the ion, K is a proportionality constant representing factors related to the instrument settings and characteristics, and t is the measured time-of-flight of the ion. MATLAB scripts were written, as described in Appendix B that allow for instantaneous data processing directly on the oscilloscope. This technique allows for the collection of a full mass spectrum each time the system is pulsed (every 100 μs).

T-Jump TOFMS has been extensively employed to examine the reaction mechanisms of various energetic materials.[6-11] In addition, effective activation energies for decomposition of nanosized oxidizers can be measured using this system and the Flynn–Wall–Ozawa isoconversional method.[12] This technique was used, as described, throughout this dissertation to investigate the reaction mechanism of various energetic nanocomposites. In addition to using the previously published technique, modifications to the system were made to allow for further investigation of these systems.

### *2.4. Air Sensitive Sample Holder (ASSH)*

The first modification of the T-Jump TOFMS system was a T-Jump enabled sample holder capable of analyzing air-sensitive samples. As described in Chapter 1, molecular aluminum clusters have the potential to revolutionize the energy density of monomolecular energetics, but these compounds are extremely air and moisture sensitive. A custom-built air-sensitive sample holder (ASSH) was designed and fabricated to allow for T-Jump TOFMS analysis of these materials. This holder was designed so that it could be cycled into a glove box to enable sample preparation in an anaerobic environment.

The ASSH was fabricated from a Klein Flansche (KF) custom reducing nipple, steel tubing, quick-connect coupling, and a 3D printed collar. The KF reducing nipple, steel

tubing, and quick-connect coupling were welded together to create a sheath that would house the T-Jump probe used in the TOFMS as shown in Figure 2.3.

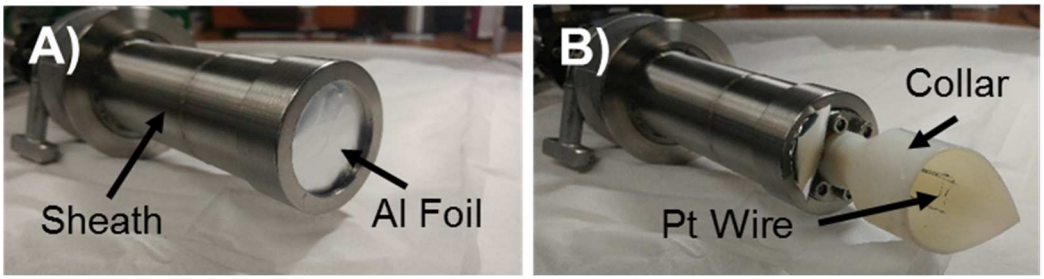


***Figure 2.7.*** *Air-sensitive sample holder (ASSH) with T-Jump probe sealed in argon environment (A) and after extending through Al foil (B).*

A ~25 μm thick aluminum foil membrane is placed into the opening of the quick-connect coupling and sealed via compression of a gasket when the threaded cap of the quick-connect is tightened onto the sheath. A standard glove box indicator solution that changes color in the presence of oxygen was used to demonstrate the effectiveness of the membrane in maintaining an anaerobic atmosphere after removal from the glove box. The indicator maintained its color even after the ASSH sat in ambient conditions for 1 hour. In a typical experiment, the ASSH is transferred from the glove box to the TOFMS in less than 10 minutes.

The aforementioned collar was designed in SolidWorks and 3D printed using a Stratasys Objet30 Pro. The collar was then press fit onto the electrical feedthrough of the T-Jump probe and fixed with a set screw. The purpose of this collar is to controllably and reproducibly cut and fold the foil membrane during insertion of the T-Jump probe into the TOFMS as shown in Figure 2.3. It is extremely important that the membrane remains intact within the TOMFS to avoid pieces of the foil getting sucked into the turbo pumps used to maintain the high vacuum environment in the TOFMS. The ASSH was used for the work done in Chapters 3 and 4 on the high heating rate reaction mechanisms of air-sensitive

aluminum clusters. A detailed procedure for a typical experiment using the ASSH where a sample is loaded in a glove box and transferred to the TOFMS is described in Appendix C.

### *2.5. Nanocalorimetry Coupled Time-of-Flight Mass Spectrometry*[*]

Numerous studies have been conducted using T-Jump TOFMS to investigate the reaction mechanism of various materials at high heating rates, but one major flaw in this technique is that T-Jump heating does not yield any data on the energetics of the studied reactions. In addition, the T-Jump technique has a relatively large error in the temperature measurement (±50 $^{o}$C). In order to increase the precision of the temperature measurement and obtain simultaneous thermal and speciation data at high heating rates, a nanocalorimeter sensor was integrated into the TOFMS. The nanocalorimeter sensor was incorporated into the extraction region of the TOFMS system to provide sample heating and thermal information simultaneously with evolved species identification. This approach can be used to measure chemical reactions and evolved species for a variety of materials. Furthermore, since the calorimetry is conducted within the same proximal volume as ionization and ion-extraction, evolved species detected are in a collision-free environment, therefore intermediate and radical species can be detected. To demonstrate the capabilities of this system, I will present measurements showing the decomposition of ammonium perchlorate, copper oxide nanoparticles and sodium azotetrazolate. The rapid, controlled and quantifiable heating rate capabilities of the nanocalorimeter coupled with the 0.1 ms temporal resolution of the TOFMS provides a new measurement capability and insight into

[*] The results presented in this chapter have been previously published and are reprinted with permission from: Yi, F.; DeLisio, J.B.; Zachariah, M.R.; LaVan, D.A., Nanocalorimetry-Coupled Time-of-Flight Mass Spectrometry: Identifying Evolved Species during High-Rate Thermal Measurements, *Anal. Chem.,* **2015**, 87, 9740. Copyright 2015 American Chemical Society. My role in this work was to integrate the nanocalorimeter into the TOFMS, synchronize data acquisition, and combine nanocalorimeter and TOFMS data.

high rate reactions, such as those seen with energetic nanocomposites. The copper oxide nanoparticles and ammonium perchlorate used in this study were obtained from Sigma Aldrich. The copper oxide nanoparticles had a nominal particle size of less than 50 nm. Sodium azotetrazolate was synthesized in house using a previously reported procedure.[13]

### *2.5.1. Chip Based Calorimetry*

Microfabricated nanocalorimeter sensors are capable of making thermal measurements on small amounts of sample (micrograms to nanograms), and at very fast heating and cooling rates.[14-18] Nanocalorimetry has previously been applied for measurements of a wide variety of types and forms of materials.[19] These dynamic thermal measurements can be made at rates up to 5 orders of magnitude faster than traditional differential scanning calorimetry (DSC). A typical nanocalorimeter sensor can heat at rates up to $10^6$ K/s, and has sensitivity, in terms of heat capacity, on the order of 1 nJ/K. Figure 2.4A shows an image of the front of a typical nanocalorimeter that has a 100 nm thick platinum heater suspended on a 100 nm thick silicon nitride membrane in a silicon frame. The heating rate is sufficiently fast to take advantage of the rapid temporal resolution of the TOFMS.

### *2.5.2. System Integration Details*

The nanocalorimeter sensors were inserted, using a custom holder, into the vacuum chamber of the mass spectrometer adjacent to the electron impact ionization region, as shown in Figure 2.4B.

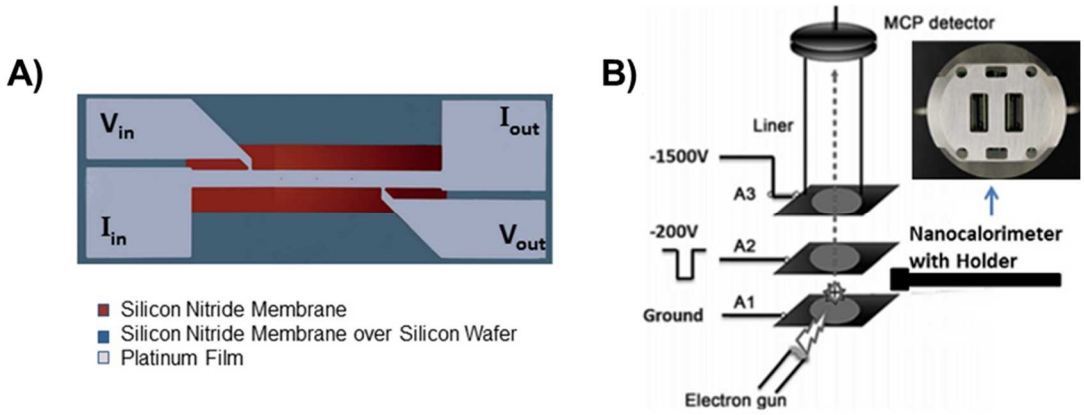


***Figure 2.4.*** *(A) top view of a typical microfabricated nanocalorimeter sensor (13.7 mm long overall), (B) schematic diagram of the nanocalorimeter integrated into the TOFMS with a photograph of the front face of the holder.*

The holder for the nanocalorimeter sensor was designed using commercially available ultra-high vacuum electrical and linear motion feedthrus and a 3D-printed adapter and sensor cover. The thermoplastic material from the 3D printer provided little additional background signal and was satisfactory for initial measurements under high vacuum conditions. Subsequent designs used components machined from polyether ether ketone (PEEK) or aluminum. For TOFMS, the electron beam is normally operated at 70 eV and 1 mA, with the background pressure in the TOF chamber at $\approx 7 \times 10^{-5}$ Pa ($\approx 5 \times 10^{-7}$ Torr).[6, 7] The linear TOFMS described above was used for these experiments. Specific details of the TOFMS system used have been previously described.[6, 7, 20] A 600 MHz oscilloscope (Teledyne Lecroy Waverunner 606Zi) was used for data acquisition in the TOFMS system. The oscilloscope was triggered at 10 KHz and ran using sequence mode with 95 segments, where each segment represents a mass spectrum. 50 us of each segment was recorded with a 100 MSamples/s sampling rate.

The nanocalorimetry system can measure thermal signals at heating rates up to $10^6$ K/s. The fabrication and calibration of the nanocalorimeter chips used in this work has been

previously described in detail.[21] In brief, the calibration is based on resistive heating of the platinum heater/thermometer and optical pyrometry to record temperature. When using a Gaussian fit to identify peak centers, the melting temperature for pure aluminum can be measured within 1 K (at 933.5 K). The error associated with the temperature measurement is small and would be illegible if represented graphically on the plots presented here. Measurements were performed by applying a current pulse and measuring the current and the voltage drop to provide an instantaneous measure of chip resistance and power. Based on the temperature coefficient of resistance from calibration, chip temperature is calculated at each data point (204 kSamples/s ≈ 5 μs intervals). The acquired data is post-processed to calculate apparent heat capacity by subtracting the heat losses found by examining the power needed to heat the bare chip. The term "apparent heat capacity" is used as this value includes contributions from the heat capacity of the sample and the enthalpy of the transformation(s) observed. Appendix D provides details on the heat loss correction calculations and methods to calculate heat capacity and enthalpy in a nanocalorimetry experiment.

Synchronization between the TOFMS and nanocalorimetry system is critical in correlating the evolved species to the acquired thermal data. As shown in Figure 2.5, serial pulses generated from a pulse generator are used to trigger a high voltage pulser so that the ionization and extraction processes occur continuously.

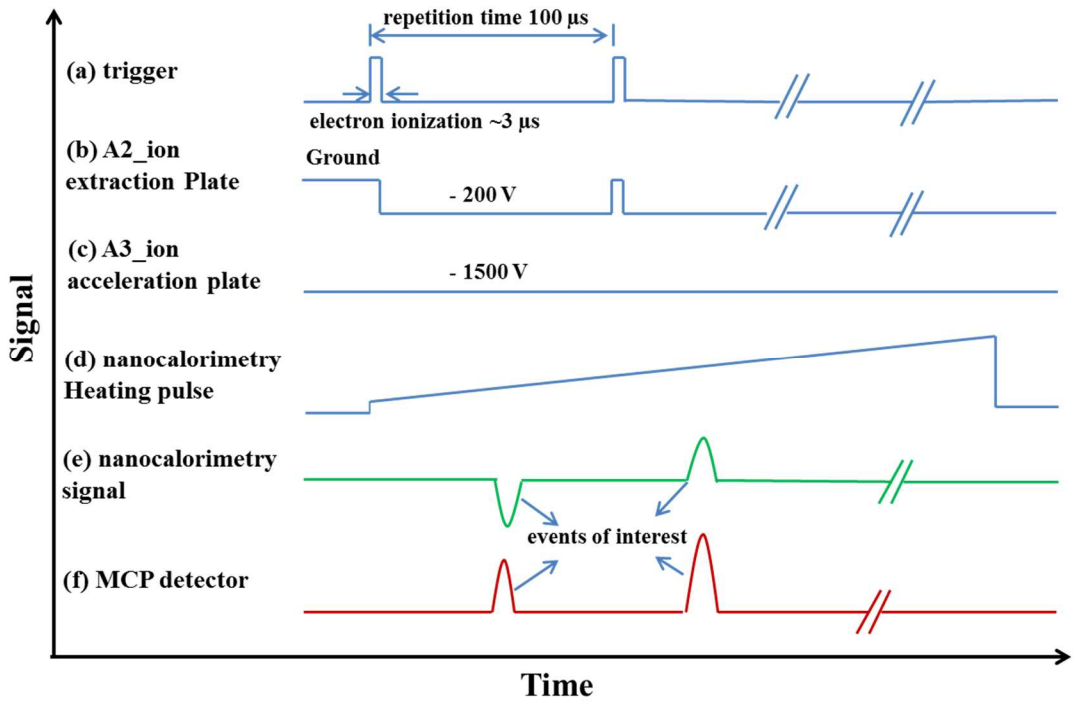


***Figure 2.5.*** *Synchronization scheme for integrated TOFMS and nanocalorimetry system.*

The data acquisition system for nanocalorimetry uses a PXI chassis with an embedded controller and two high-precision dynamic signal analysis cards (NI PXI-4461 and NI PXI-4462). This system can simultaneously generate 2 analog outputs and measuring 6 analog inputs with 24-bit resolution at speeds up to 204 kS/s. The PXI platform is also equipped with a precision clock for timing signals and triggering lines so that signal generation and measurement tasks can be synchronized with each other and external equipment like the TOFMS. The nanocalorimetry system does not start until the first trigger pulse is applied. Dynamic signal acquisition (DSA) devices use a digital filter to remove frequency components above the Nyquist frequency which introduces a filter delay, which for this hardware is 63 samples on inputs and 32 samples on outputs. Because we are synchronizing with another instrument, the filter delay for input has to be considered, so the delay is accounted for in recorded signals.

### *2.5.3. Results and Discussion*

To demonstrate the capability of the integrated instrument, three different materials were measured including an organic salt, sodium azotetrazolate (Na-TZ), an inorganic compound, ammonium perchlorate (AP) and a metal oxide nanoparticle - copper oxide (CuO). The samples were deposited onto the nanocalorimeter sensor using electrospray.[22] During these experiments, the sample is heated for 8 ms and approximately 1600 data points are acquired at 5 μs intervals. Simultaneously, a sequence of 95 spectra with mass to charge ratio (m/z) up to 380 are recorded at 100 μs intervals. Trace background species observed when no samples were present in the TOFMS consist of $H_2O^+$, $OH^+$ (due to fragmentation of $H_2O$), $N_2^+$, and $O_2^+$.

Na-TZ is an energetic tetrazole salt that is fairly insensitive as a pentahydrate, but is extremely sensitive and dangerous when it is dried.[13] These experiments were performed using the hydrated form of the salt. As shown in Figure 6, the mass spectrum shows the signal intensity of m/z ratios evolving with time (a) and the nanocalorimetry results show temperature and apparent heat capacity/heating rate profiles of Na-Tz with time (b). No high mass ions were observed and major ions were only seen for $m/z < 30$. The mass spectra between 1 ms and 7 ms were plotted in Figure 2.6a. Three major species were observed: water, nitrogen and sodium. The nanocalorimeter sensor (Figure 2.6b) measured three thermal signals. The most prominent feature is a large exotherm appearing at 4.3 ms, and 514 °C. At both 2.7 ms and 5.8 ms, there are endotherms with corresponding temperatures of 238 °C and 774 °C respectively. This measurement allows us to directly match the thermal results with the detected gas phase species. As shown in Figure 2.6c, the first thermal signal at 2.7 ms (238 °C) is water from the dehydration of Na-Tz, which is an

endothermic process. The large exotherm observed at 4.3 ms (514 °C) corresponds to the evolution of molecular nitrogen, from decomposition of Na-TZ. The proposed net decomposition reaction is shown below:

$$Na_2C_2N_{10} \rightarrow 5N_2 + 2C + 2Na$$

This decomposition is followed by an endotherm at 5.7 ms (770 °C) associated with the appearance of sodium. It should be noted that this temperature is significantly lower than the bulk boiling point of sodium, (883 °C) likely due to volatilization under reduced pressure

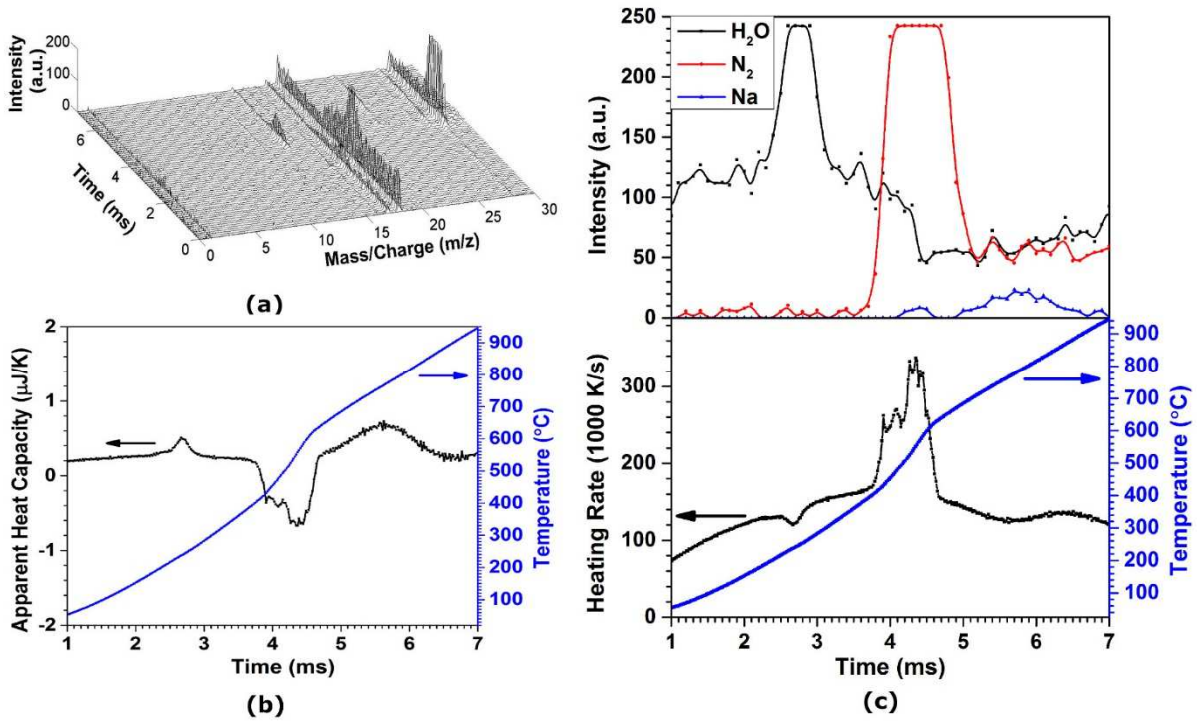


***Figure 2.6.*** *Results for sodium azotetrazolate (Na-TZ). (a) mass spectra, (b) nanocalorimetric thermal signals, (c) synchronized results of mass spectra and thermal analysis.*

As a second example, ammonium perchlorate ($NH_4ClO_4$) was studied, which is one of the most common oxidizers used in various propellants and pyrotechnics. Understanding the thermal decomposition of AP under combustion like heating conditions is critical to

understanding its behavior in energetic applications. However, the thermal decomposition is complicated and strongly depends on experimental conditions such as whether it occurs in an open or closed system. This integrated instrument provides a new tool to measure and study thermal decomposition of AP. This experiment was performed under high vacuum (not an oxidizing environment); it reports on the initial decomposition, which would be one step to understanding the decomposition mechanism and subsequent reaction under oxidizing conditions.

In Figure 2.7A, we show results from rapid heating of AP. The endothermic peak at 2.5 ms (267 °C) in the AP results is attributed to the crystal transformation from orthorhombic to cubic form. After the phase transformation, a large endothermic signal appears which corresponds to evolution of $ClO_2$, $HClO_4$, $ClO_3$, ClO and Cl as products of decomposition, which is similar to data recorded for the thermal decomposition of AP at approximately 400 °C.

As mentioned above, measurements on AP are highly sensitive to experimental conditions and material form. Under conditions where the reactants are readily transported away from the reaction (such as the measurement here, where a small sample is open to the vacuum chamber), the decomposition will be seen as endothermic, while exothermic decompositions will be seen for larger samples and those held in a sealed crucibles or under pressure. A difference that varies with test conditions, such as when using an open pan or sealed pan, has been reported previously for related macro scaled measurements.[23]

Ammonium perchlorate is known to have an exothermic decomposition at temperatures above 380 °C that proceeds as follows.[24]

$$2NH_4ClO_4 \rightarrow Cl_2 + 2NO + O_2 + 4H_2O$$

In this experiment, it is proposed that gas phase reactions are not occurring on the nanocalorimeter chip due to the nanocalorimeter being an open system at low pressure ≈ 1 × $10^{-4}$ Pa (≈ $10^{-6}$ Torr). These results agree with the previously proposed proton transfer based mechanism for decomposition of AP.[24] In the first step of this mechanism, there is proton transfer from cation to anion to form gaseous $NH_3$ and $HClO_4$. This is an endothermic, entropy driven process. These gaseous species can then react to form the stable gaseous products described in the net equation above. Calculations using the National Aeronautics and Space Administration (NASA) Chemical Equilibrium with Applications (CEA) code were performed to validate that these gas phase reactions are what make the overall decomposition reaction exothermic. For measurements in vacuum in an open calorimeter system, the gaseous species are unable to react and are ionized by the electron gun resulting in the mass spectrum and calorimeter results observed in this experiment.

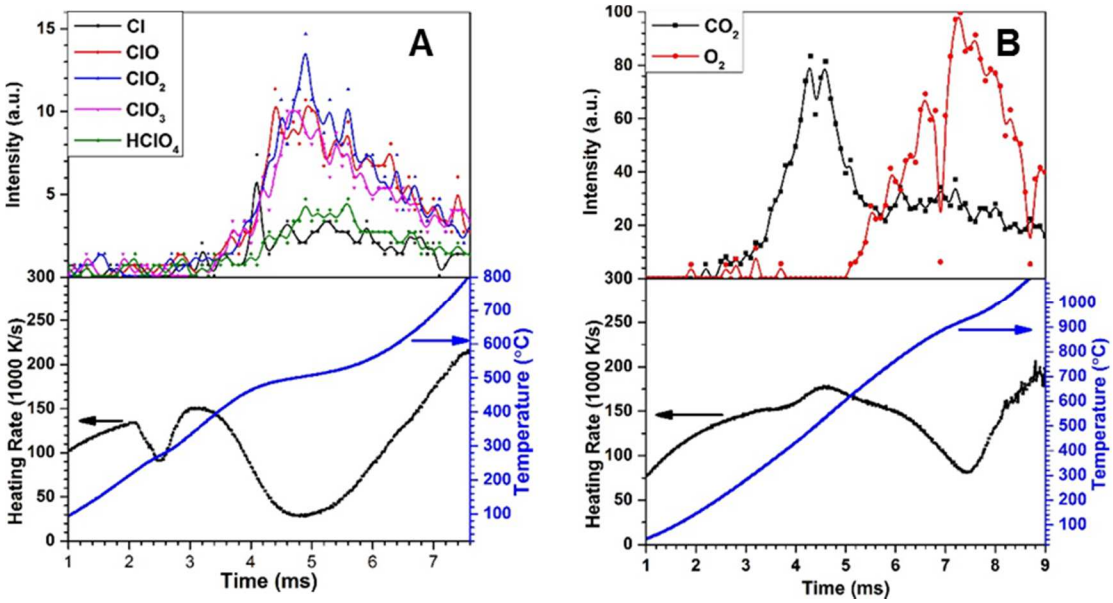


***Figure 2.7.*** *Mass spectra and nanocalorimeter data of ammonium perchlorate (A) and copper oxide (B).*

Metal oxides, often in nanoparticle form, are often used as thermistors, chemical sensors, catalysts, and oxygen carriers for combustion reactions, such as in thermites or for chemical looping.[20, 25-28] Here, copper oxide nanoparticles are electrosprayed onto the active area of the nanocalorimeter. Figure 2.7B shows the temporal speciatiation and thermal results. Two endothermic signals and the evolution of two species ($CO_2$ and $O_2$) were observed. At 3.8 ms (402 °C) an endothermic signal is observed corresponding to the release of $CO_2$ from decomposition of basic copper carbonate.[29] The second significantly larger endotherm at 7.4 ms (931 °C), shows significant evolution of molecular oxygen and indicates the decomposition of CuO. A large exothermic signal was also observed over 1100 °C accompanied with nitrogen release (data not shown), which may be related to the interaction between the released oxygen and sensor membrane.

Additional measurements on the same sample performed without breaking vacuum show a higher temperature peak corresponding to the melting of copper, which confirms the complete decomposition of copper oxide in the first cycle. The onset of the decomposition of copper oxide is at 5.0 ms (600 °C), which is slightly lower than a recent report[30] on the decomposition of copper oxide investigated using a T-jump TOFMS system that found the onset of oxygen release increases as the heating rate increases from $\approx 1.5 \times 10^5$ K/s to $\approx 6.5 \times 10^5$ K/s. The corresponding onset temperature from that work would be at 650 °C, which is higher than the value reported here. There are slight differences in our method compared to this previous result – this sample is deposited in a more uniform, thin layer and we individually calibrate each sensor, as the sensors are made from deposited platinum films. [31]

### 2.5.4. *Nanocalorimetry Coupled Time-of-Flight Mass Spectrometry Summary*

In summary, this section presented the combination of nanocalorimetry and TOFMS as a novel integrated system capable of simultaneously measuring thermal properties and evolved gas-phase species. This new technique expands on the previously described T-Jump TOFMS technique by adding calorimetry capabilities while maintaining desirable high heating rates. Measurements for three different types of materials were presented to demonstrate the capability of the new instrument. A highly exothermic decomposition corresponding to the release of nitrogen gas was observed for the tetrazole salt, Na-TZ. CuO nanoparticles were also used as a test sample in which a measured endotherm could be coupled with the time resolved TOFMS spectra to determine an oxygen release temperature. This system was also capable of probing the initial step in decomposition of AP where an endotherm and various gaseous species were identified. This method accelerates the investigation of material properties and the development of new applications, especially for energetic reactions and thermal desorption of catalytic materials. This technique was applied to the investigation of Al/CuO reactive nanolaminates in Chapter 6.

## *2.6. Molecular Beam Sampling Reflectron Time-of-Flight Mass Spectrometry*

Unfortunately, T-Jump TOFMS can only probe reaction mechanisms at low pressures because the T-Jump probe must be directly inserted into the ionization/extraction region of the TOFMS. In addition, samples must be coated on the thin (76 μm) Pt filament of the T-Jump probe, therefore the types of samples than can be analyzed are limited. To investigate the effect of architecture on the reaction mechanisms of energetic nanocomposites, much larger samples with unique microstructures are needed. In order to

add more versatility to the sampling environment and types of samples that can be analyzed, I have designed and constructed a molecular beam sampling system coupled with a reflectron time of flight mass spec system (RTOFMS). The molecular beam sampling time-of-flight mass spectrometer (MBMS) system has the ability to directly sample free standing material that has been created using electrospray deposition methods. With the sampling region located outside of the vacuum chamber, there are very few limitations on types of samples and sampling conditions. This technique allows us to probe the reaction mechanism in different environments and compare microstructural features to optimize performance of the energetic material, whether it be for propellant, explosive, or other applications.

*2.6.1. Designing the MBMS*

A reflectron time of flight mass spectrometer (RTOFMS) of R. M. Jordan make is used in this instrument. The operating principle of the RTOFMS system is identical to the TOFMS above, but with two exceptions: 1) RTOFMS employs a single-stage reflectron region that effectively doubles the focal length of the TOFMS improving mass resolution and 2) A much larger active diameter MCP detector (40 mm vs the 18 mm) is used in the RTOFMS than the TOFMS above resulting in improved signal intensity. The RTOFMS was first assembled and tested using a precision leak valve to ensure the MS system was functioning properly.

The most crucial part of the MBMS system is the differentially pumped sampling chamber mounted on the RTOFMS. In this chamber, gas is rapidly expanded through a sampling orifice into a low pressure region. This rapid expansion creates a shock wave that can be probed with a skimmer cone leading into an even lower pressure region to form a

molecular beam. This beam then passes through the ionization region of the RTOFMS and exits the system through a "beam dump" into a turbomolecular pump. The essential feature of the MBMS relies on the sudden transition from a continuum environment (reaction event) to one which is collision-less (E-gun ionization region/flight tube). The sudden transition in tandem with the creation of an ultra-cold supersonic molecular beam enables the preservation of the sample until reaching the detector of the mass spectrometer.

The key design parameter in the construction of this chamber was to maximize pumping speed between the sampling orifice and skimmer cone while minimizing the distance between them. Preliminary calculations of flow rate through a critical orifice were used to estimate the pumping speeds necessary to obtain the desired pressure differentials. The equation used for these calculations is as follows:

$$Q = \frac{0.58 k A_o}{\rho_a} (\gamma \rho_1 P_1)^{1/2}$$

where Q is the flow rate, $\gamma$ is the ratio of the specific heats, k is the discharge coefficient, $A_o$ is the annular area, $\rho_1$ is the upstream gas density, $P_1$ is the upstream pressure, and $\rho_a$ is the ambient-air density.[32] The chamber that will allow for differential pumping was designed and fabricated with assistance from Ardara Technologies L.P. A 3D model of the fabricated differential pumping chamber can be seen in Figure 2.8.

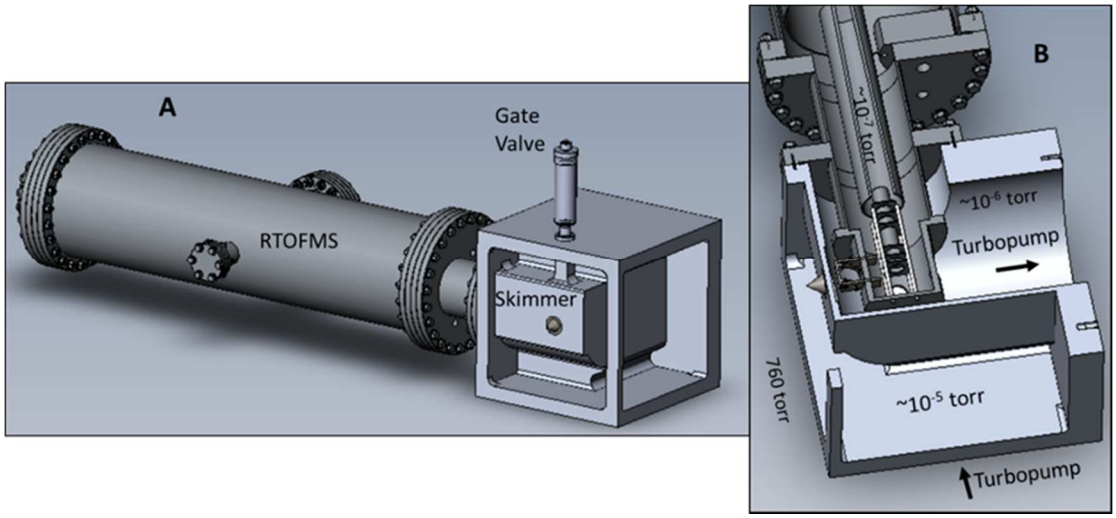


***Figure 2.8.*** *3D model of full Molecular Beam Sampling RTOFMS system (A) and cutaway view of differential pumping chamber (B).*

A custom gate valve was incorporated into the system behind the skimmer cone that is used to isolate the RTOFMS from the sampling chamber to aid in troubleshooting of the system. Initially, the system was designed with a sampling cone that had a 100 μm orifice and a fixed 1 cm sampling orifice to skimmer cone distance. The sampling cone was later replaced with a home-built quartz reactor tube with a 100-300 μm orifice. The quartz reactor allows for alignment and sampling orifice to skimmer cone distance adjustments to be made during MS acquisition.

*2.6.2. MBMS Operation*

Figure 2.9 shows a schematic of the current functioning MBMS setup during energetic nanocomposite film burning studies.

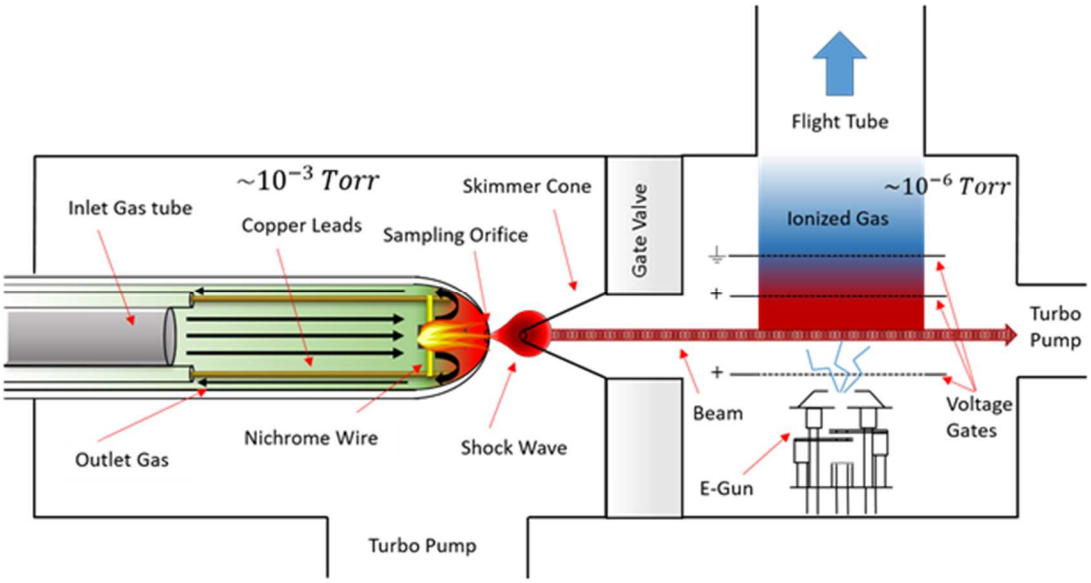


***Figure 2.9.*** *MBMS schematic of flame sampling during combustion of an energetic thin film.*

The reactive thin film is held between two nichrome wires that can be resistively heated to ignite the sample. As the sample burns, gas phase reaction products are sampled via the formed molecular beam. A mirror was inserted into the sampling region that can be seen through a window on the chamber to enable high-speed videography of the combustion event. In a typical experiment, roughly 3.5 seconds worth of time resolved MS data are captured utilizing a 600 MHz Teledyne LeCroy Oscilloscope at a sampling rate of 1-3 full mass spectra per millisecond (1-3 kHz). This system was used to analyze the combustion of nAl/PVDF thin films in Chapter 9.

In order to ensure the formation of a molecular beam, the gate valve was partially closed to deflect the beam and the background spectrum was recorded. This spectrum was then compared to the signal intensity of the carrier gas when the gate valve was fully opened. An example of a blocked beam and full beam mass spectrum with a nitrogen filled sampling region is shown in Figure 2.10.

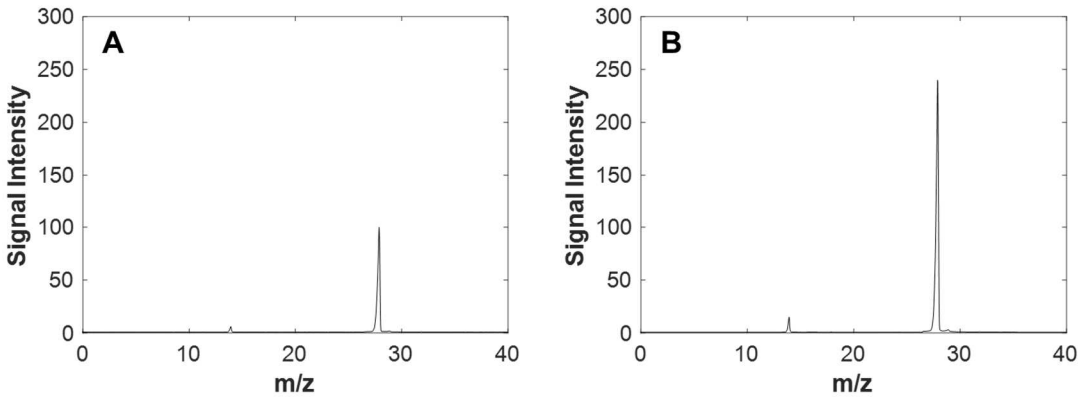


***Figure 2.10.*** *Mass spectra of blocked (A) and full (B) molecular beam formed from a nitrogen filled sampling region. The signal intensities are normalized to the $N_2$ (m/z = 28) maximum signal intensity in the blocked beam case.*

The comparison of the full beam to blocked beam signal intensity is referred to as the beam to background ratio and can be used as a measure of beam fidelity. This ratio varied between experiments as the quality of the formed beam is dependent on alignment of the sampling orifice with the skimmer cone and ionization region. The full beam intensity typically ranges from 200-400 % of the blocked beam.

A custom triggering circuit was designed and fabricated in order to synchronize wire heating with data collection from the MBMS and high-speed imaging. This circuit was used to convert the 1-10 kHz pulse required for TOFMS operation into a longer pulse (1-8 seconds) that closed a relay initiating heating of a resistively heated nichrome wire. Figure 2.11 shows the circuit diagram for the constructed triggering system.

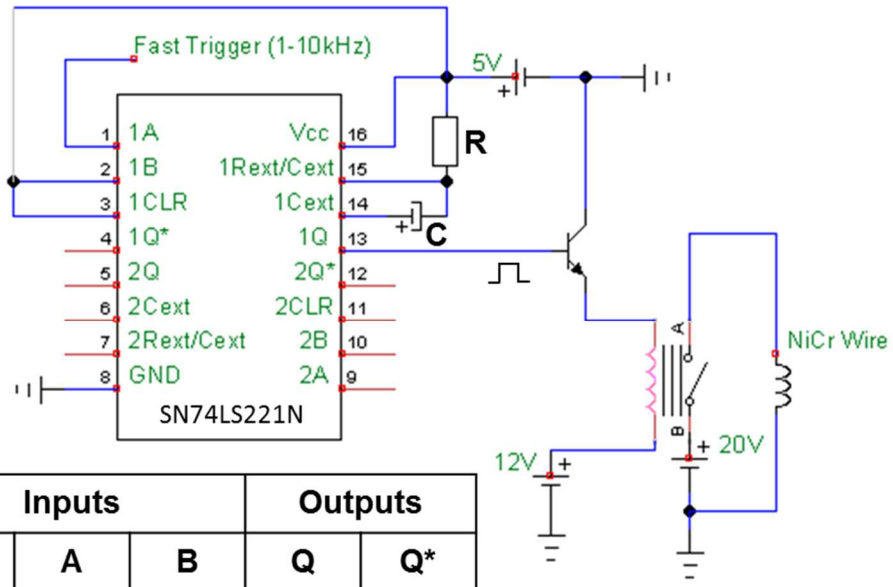


| Inputs | | | Outputs | |
|---|---|---|---|---|
| CLR | A | B | Q | Q* |
| H | ↓ | H | ⎍ | ⎏ |

***Figure 2.11.*** *Circuit diagram for MBMS timing circuit to synchronize data acquisition with ignitor wire heating.*

The falling edge of the first pulse from the 1-10 kHz signal triggers a monostable multivibrator that creates the 1-8 second pulse depending on the resistance (**R)** and capacitance (**C**) used in the circuit. The pulse width is equal to 0.7***C*R**. A detailed procedure for operation in addition to details on system construction can be found in Appendix E.

# Chapter 3: Role of Oxide Shell Crystallization in the Oxidation Mechanisms of Tantalum Nanoparticles and Nanothermites*

*Summary*

Previous studies on the oxidation of aluminum nanoparticles have shown the importance of oxide shell crystallization, but analyzing its effect at relevant timescales to combustion is difficult due to aluminum melting during oxide crystallization. In this work, tantalum nanoparticles were studied using TGA/DSC, temperature jump ignition, and high heating rate TEM analysis to probe the role of oxide shell crystallization in the oxidation mechanism of tantalum nanoparticles and nanothermites due to the high melting point of tantalum (3017 $^{o}$C) in relation to that of aluminum (660 $^{o}$ C). When oxidized by gas phase oxygen, the oxide shell of the tantalum nanoparticles rapidly crystallized creating cracks that may attribute to enhanced oxygen diffusion into the particle. In the case of tantalum based nanothermites, oxide shell crystallization was shown to induce reactive sintering with the metal oxide resulting in a narrow range of ignition temperatures independent of the metal oxide used.

## *3.1. Introduction*

Metal fuels possess higher energy densities than standard CHNO based energetics, but traditionally suffer from slow reaction kinetics.[1-3] However, reduced diffusion length scales and increased specific surface areas of nanosized components have recently demonstrated increased reaction rates for these systems. [1, 4] Most metal nanoparticles are passivated by a thin (typically 3-5 nm) nascent oxide shell, creating a barrier between

* The results presented this chapter are in preparation for journal submission with authors Jeffery B. DeLisio, Xizheng Wang, Tao Wu, Garth C. Egan, Rohit J. Jacob, and Michael R. Zachariah.

the metal fuel and any oxidizer.[5] As the particle size decreases, the mass fraction of metal oxide makes up a significant percentage of the particle. Understanding the interaction between the metal core and the metal oxide shell is crucial in understanding the oxidation mechanism of the system.[6, 7] Despite increased interest in energetic nanocomposites, only recently has a global mechanism been developed for the reaction between Al and CuO nanoparticles.[8] Currently, there lacks significant experimental results using other metal nanoparticles in nanothermite compositions to evaluate the validity of this model for other systems.

Aluminum is the most commonly used metal fuel due to its favorable energy density, low cost, and ignition characteristics.[2] Its oxidation mechanism has been extensively studied and two prominent mechanisms for the ignition of Al nanoparticles (nAl) have been proposed: a diffusion based mechanism where oxidizer and aluminum diffuse through the oxide shell boundary [9-11] and a melt dispersion based mechanism [12] where there is a violent rupturing of the oxide shell followed by spallation of the aluminum core. Previous studies have shown that decreasing the particle size of the fuel can dramatically decrease the ignition temperatures of Al based nanocomposites with the minimum recorded ignition temperatures being near the aluminum melting point.[11, 13] High heating rate experiments have also shown that sintering of Al can occur on similar timescales as chemical reaction.[14, 15]

Due to scientific advancements in the field of nanotechnology, nanopowders of a wide variety of metals are now commercially available. In order to understand the contributions of key properties of nanosized metal fuels in their oxidation mechanisms, tantalum (Ta) nanopowder was chosen due to its high melting point in comparison to Al,

3017 ºC vs 660 º C, respectively. It is known that the crystallization of aluminum's oxide shell ($Al_2O_3$) is an important part of the Al ignition mechanism. [7, 16, 17].Unfortunately, this is a difficult process to thoroughly investigate because oxide crystallization occurs at a temperature very close to the melting point of Al.[7] Analogously, it has been observed that amorphous to crystalline transition in $Ta_2O_5$ thin films beginning at ~500 ºC with crystallization occurring rapidly at higher temperatures [18], however unlike Al, the effect of the oxide shell crystallization on ignition of tantalum nanopowders (nTa) can be probed without interference from melting.

Ta/tungsten oxide ($WO_3$) thermite composites prepared by sol-gel synthesis and spark plasma sintering have been previously studied, but these composites employed micron-sized (5 μm average particle size) tantalum.[19-21]. In our work, the oxidation of nTa (<50 nm average particle size) in an aerobic environment at both low and high heating rates was studied in addition to the reaction mechanisms of several tantalum based nanothermites at high heating rates. These experiments were used to examine the oxidation of nTa strictly by a gas phase oxidizer ($O_{2(g)}$) in addition to a condensed phase oxidizer (metal oxide) in a nanothermite mixture. Thermogravametric analysis and differential scanning calorimetry (TGA/DSC) were employed to investigate the oxidation of Ta and Al nanopowders at slow heating rates. Temperature jump (T-Jump) ignition and high heating rate TEM experiments were performed to examine the ignition behavior of Ta nanopowders (nTa) in the presence of oxygen, in addition to Ta based nanothermites in vacuum. Ta ignition was observed well below the melting points of Ta and tantalum oxide ($Ta_2O_5$), 3017 ºC and 1872 ºC respectively. The experimental results allude to an oxygen diffusion dominated oxidation mechanism as the metal fuel is immobile prior to measured

ignition temperatures. High heating rate TEM experiments also show two distinct oxidation mechanisms occurring depending on the maximum temperature achieved in the respective experiment.

### *3.2. Experimental*

#### *3.2.1. Materials*

nAl (~50 nm) was purchased from Novacentrix with an active Al content of 81 % by mass, determined by thermogravimetric analysis (TGA) as stated by the manufacturer. The nTa (<50 nm) used in this study was purchased from Global Advanced Metals. All metal oxide nanopowders (< 50 nm) used in Ta based thermite mixtures for T-Jump and TEM analysis were purchased from Sigma Aldrich. Thermite suspensions were prepared by physically mixing Ta with the corresponding metal oxide in hexane (T-Jump) or ethanol (TEM) and sonication for 30 minutes.

#### *3.2.2. TGA/DSC Characterization*

Thermogravametric analysis and differential scanning calorimetry (TGA/DSC) was performed using a TA Instruments SDT Q600. For both nTa and nAl oxidation analysis runs, a heating rate of 20 $^{o}$C/min and $O_2$ flow rate of 100 mL/min were employed.

#### *3.2.3. T-Jump Ignition*

A home built temperature jump (T-Jump) thin platinum (Pt) wire ignition source was used with a heating rate of ~$10^5$ K/s.[22, 23] The 76 μm diameter Pt wire was rapidly joule heated with a 3 ms current pulse while high-speed video was taken at 67000 frames per second using a Phantom v12.0 digital camera running Phantom 692 software. Ignition time and temperature were then determined by mapping against the Callendar-Van Dusen temperature extrapolation from the temporal resistance of the Pt wire. T-Jump ignition

experiments were performed in a pure $O_2$ environment at pressures ranging from 0.2 to 18.7 atm and under vacuum (~$10^{-6}$ torr).

*3.2.4. Ex Situ and In Situ High Heating Rate TEM*

High heating rate studies in a TEM were conducted with Protochips Arduro heating chips with a Protochips TEM holder in a JEM 2100 FEG TEM/STEM, equipped with Oxford EDS and Gatan Tridiem EELS systems, with an accelerating voltage of 200 kV. Ta nanopowders were deposited onto an Arduro chip and heated in air whereas the Ta based nanothermites were heated under vacuum within the TEM. All samples were heated at $10^5$ K/s and held for a period between 1 and 100 ms.

*3.2.5. Combustion Cell Characterization*

Ta/CuO nanothermite was evaluated using a previously described combustion cell.[24] 25 mg of sample was placed in the ~13 $cm^3$ cell and ignited by a resistively heated nichrome wire. An oscilloscope was used to record simultaneous pressurization and optical emission from a pressure transducer and a photomultiplier tube, respectively.

*3.3. Results and discussion*

*3.3.1. Oxidation of nTa by Gas Phase Oxygen*

*TGA/DSC Oxidation Analysis*

The oxidation of nTa was first studied using standard slow heating rate TGA/DSC under an $O_2$ flow (Fig. 3.1).

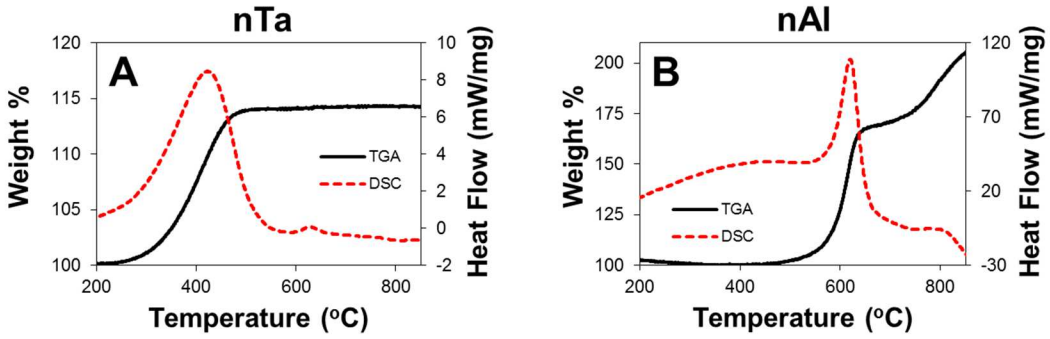


***Figure 3.8.*** *TGA/DSC of nTa (A) and nAl (B) under 100 mL/min of $O_2$ at a heating rate of 20 °C/min.*

In the case of nTa, oxidation is a 1 step process beginning at ~300 °C and ending at ~500 °C. The exotherm occurring slightly above 600 °C possibly corresponds to the crystallization of $Ta_2O_5$ as the mass stays constant during this event. Complete oxidation of the nTa would result in a final weight percent of ~115 %, indicating the nTa contains ~70% unoxidized Ta before heating, as shown in Figure 3.1A. The onset temperature for oxidation is much lower for nTa (~300 °C) than nAl (~600°C), but the initial exotherm corresponding to oxidation occurs much more rapidly in the nAl case. This can be attributed to the outward diffusion of Al from the core when near the melting point of Al (660 °C). Trunov et al., have described the oxidation of nAl at slow heating rates as being a 4 step process with the predominant mass increases occurring in steps 3 and 4 corresponding to the growth of γ and α phase $Al_2O_3$ respectively.[7] nTa does not appear to follow this multi-step oxidation mechanism as there is only a single stage of mass gain during the course of heating.

In the TGA/DSC analysis of nTa oxidation, the fuel and metal oxide product are both immobile in the temperature range of the experiment. Al begins to rapidly oxidize near the Al melting point (660 °C) due to the increased diffusion rates of liquid Al. With Ta and $Ta_2O_5$ being immobile during the course of heating, oxidation must occur strictly

by diffusion of $O_2$ through the oxide shell at slow heating rates. However, nTa undergoes a rapid self-sustaining oxidation when heated quickly that is not well captured using slow heating rate analytics such as TGA/DSC.

*T-Jump ignition in oxygen*

The ignition behavior of pure nTa at various pressures of $O_2$ was analyzed using the T-jump heating technique coupled with high speed videography. The measured ignition temperatures as a function of $O_2$ pressure are shown in Figure 3.2.

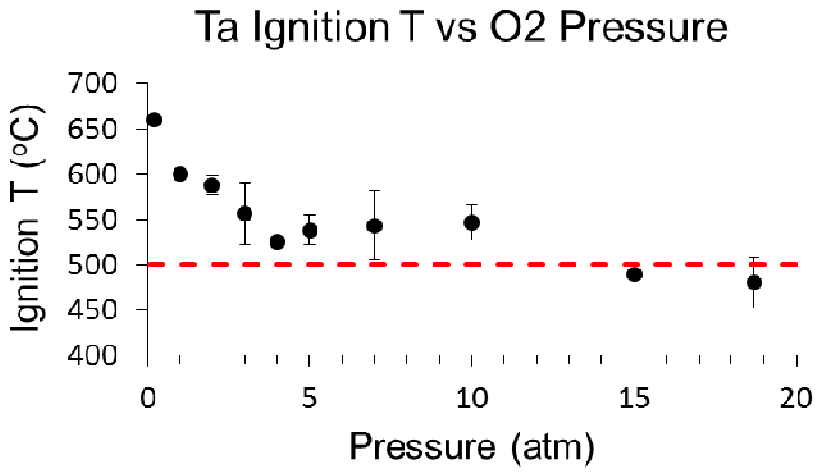


***Figure 3.9.*** *Ignition temperature of nTa measured using the T-Jump ignition technique at varying $O_2$ pressures.*

The measured ignition temperatures are much lower than those of nAl at the same pressures using an identical technique.[13] With the Ta having such a high melting temperature, the reaction must be heavily dependent on the diffusion of oxygen through the oxide shell to the Ta core. The nascent $Ta_2O_5$ shell on the nTa has a melting point of 1872 °C, which is more than 1000 degrees higher than the measured ignition temperatures. This suggests that something must happen to this shell to allow for enhanced diffusion rates of gaseous oxygen and the ignition event leading to self-sustained oxidation of the Ta core. As stated above, Kim et al. have shown that amorphous $Ta_2O_5$ films will crystallize above 500

$^{o}$C.[18], thus it is reasonable to conjecture that the exothermic crystallization of the $Ta_2O_5$ allows for enhanced diffusion of oxygen to the Ta across the $Ta_2O_5$ boundary. This can be thought of as being similar to the hot spot ignition theory for CHNO energetics where localized points can begin to react exothermically leading to a self-propagating reaction of the bulk material.[25] Potentially, only one point may rapidly crystallize, exposing the Ta core aiding in the rapid oxidation of Ta. The heat generated during the rapid oxidation will contribute to the further crystallization, and at potentially a temperature spike to enable melting of the $Ta_2O_5$, exposing more of the Ta core. This theory was further explored using high heating rate TEM.

*High heating rate TEM of nTa*

In order to probe the oxidation mechanism of nTa, the growth of the $Ta_2O_5$ oxide shell was investigated by depositing nTa onto Protochips Arduro heating chips. First, the chip was inserted into the Protochips TEM holder and multiple particles were imaged and positions were recorded. In order to oxidize the nTa, the holder was removed from the TEM and rapidly heated in air to 500 $^{o}$C at a heating rate of $10^5$ K/s, and held at this temperature for 10 ms. This process was repeated 4 times with re-insertion of the holder into the TEM to image the particles after each stage of heating. During the last heating run, the chip was held at 500 $^{o}$C for 100 ms. Results in Figure 3.3 show oxide shell thickness growth for 7 different locations on a single Ta aggregate. It is apparent that there is a difference in growth rate depending on the location on the aggregate.

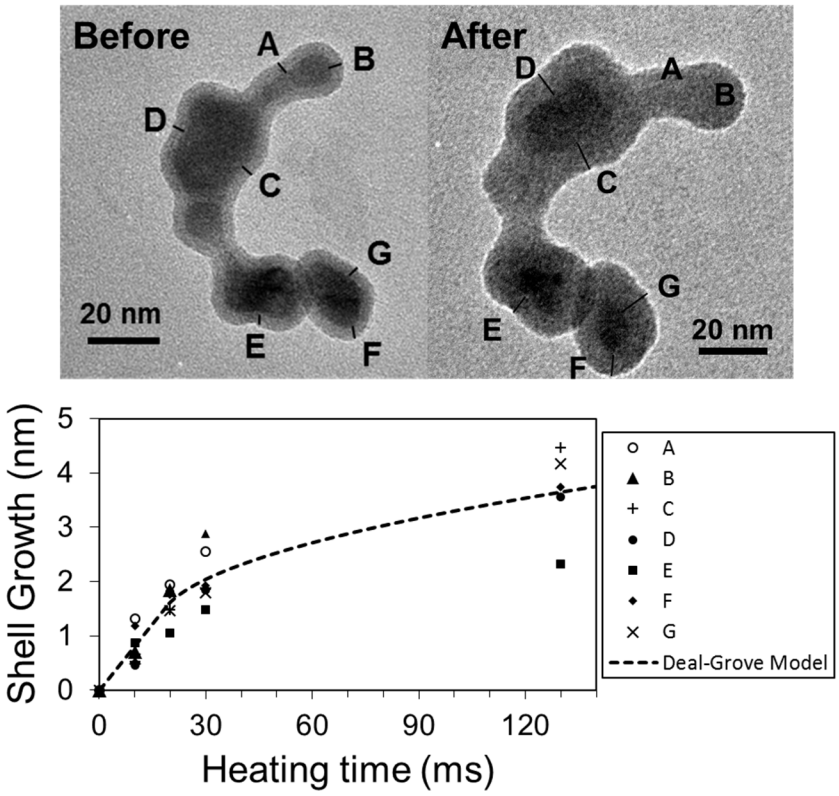


***Figure 10.3.*** *TEM image of Ta aggregate with labeled locations where oxide shell was measured before and after heating, and the corresponding heating time vs. oxide shell growth for each location along with a linear-parabolic fit of average shell growth following the Deal-Grove model.*

No crystallization of $Ta_2O_5$ is observed after any of the consecutive heating ramps, which agrees with the results seen in the TGA/DSC experiment above. In the TGA/DSC, the $Ta_2O_5$ crystallization exotherm occurs above 600 ºC.

Slow heating rate studies on the oxidation of bulk tantalum in air indicate that oxidation follows a linear rate law in the 500 ºC to 800 ºC temperature range.[26] The experimental results for the average oxide shell growth over time in Figure 3.3 appear to follow a linear-parabolic trend similar to the Deal-Grove (D-G) model for the oxidation of silicon.[27] The Deal-Grove model originally developed for oxidation of silicon shows growth following a linear growth rate at short timescales (thin oxide layer) and a parabolic growth rate for long oxidation times (thick oxide layer). This implies that oxidation is

kinetically limited in the initial stages, but once the shell reaches a certain thickness, oxidation is diffusion limited as shown below:

$$\text{Linear Region:} \qquad Z = kC_s\tilde{v}t$$

$$\text{Parabolic Region:} \qquad Z^2 = 2DC_s\tilde{v}t$$

where $Z$ is the oxide shell thickness, $C_s$ is the molar concentration of oxygen at the surface of the material, $\tilde{v}$ is the molar volume of the formed metal oxide, $t$ is time, and $k$ and $D$ represent the rate constant in the linear region and diffusion coefficient of $O_2$ in the formed metal oxide, respectively. Since both Si and Ta are immobile during the temperature range of oxidation, and presuming no other factors come into play, the D-G should be applicable to the Ta system. For the rapid heating of nTa in air to 500 $^oC$ shown in Figure 3.3, the linear to parabolic transition occurs after ~1.62 nm of shell growth (20 ms of total heating). The rate constant for the linear region, k, is determined to be 160.4 nm/ms. A diffusion coefficient, D, of 52 $nm^2/ms$ (5.2 x $10^{-14}$ $m^2/s$) was extrapolated from the parabolic portion of the plot.

A previous study on the diffusion of oxygen in amorphous $Ta_2O_5$ thin films (100 nm thickness) report a diffusion coefficient of 2.5 x $10^{-19}$ $m^2/s$ at ~525 $^oC$.[28] Our extrapolated value for oxygen diffusion through the oxide shell of nTa is more than 5 orders of magnitude larger. This is most likely due to the previous study being done on compact $Ta_2O_5$ films while our oxygen diffusion coefficient was determined during oxidation of nTa and therefore more accurately represents oxygen diffusion during combustion.

Drastic surface changes of the oxide shell are clearly shown in Figure 3.4 when Ta nanoparticles were heated in air to 850 $^oC$ and held at temperature for 1 ms. 850 $^oC$ was chosen as the final temperature to ensure all analyzed particles were sufficiently heated

above 500 °C with only 1 ms of hold time due to heat losses from the chip when heated in air. During oxidation, the particle's outer diameter increased from 32.83 to 38.16 nm, while the Ta core shrank by nearly 4 nm. This particle diameter growth is due to the density of $Ta_2O_5$ being approximately half that of the Ta metal core (8.2 g/cm$^3$ vs. 16.7 g/cm$^3$ respectively). After rapid heating to 850 °C, the oxide shell grew ~ 4.6 nm over 1 ms. After 130 ms of total heating to 500 °C, the average shell growth was only ~3.7 nm.

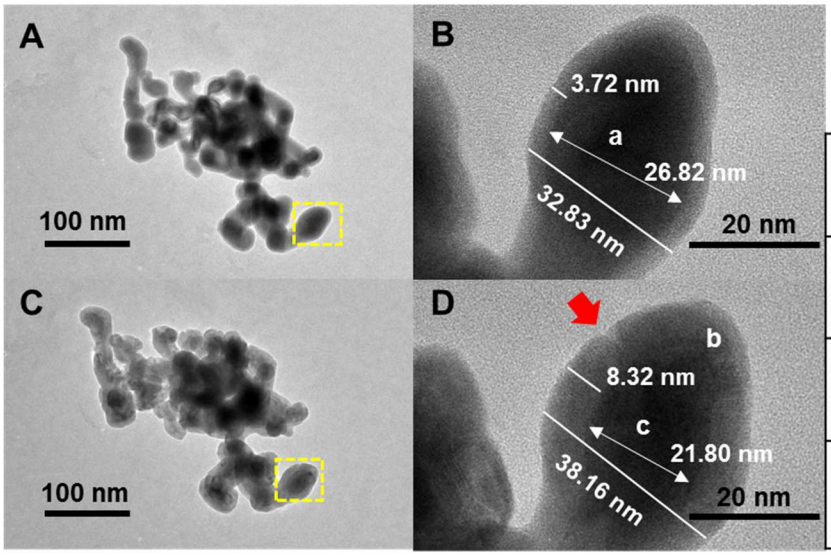


**EDS Point Scans**

| Element | Ta | O |
|---|---|---|
| a (at. %) | 100 | 0 |
| b (at. %) | 25 | 75 |
| c (at. %) | 53 | 47 |

***Figure 3.11.*** *TEM images before (A, B) and after (C, D) being heated in air to 850 °C at $10^5$ K/s and held for 1 ms. EDS point scan atomic percentages of Ta and O at locations labeled in Figure 3.4A and 3.4B.*

A crack observed in the post-heating SEM image in Figure 3.4D is further evidence that changes in the oxide shell may be enhancing oxidation rates. The rapid crystallization and the stress on the particle may cause the observed cracking of the shell, which can enhance oxygen diffusion into the core. Elemental compositions from EDS point scans in Figure 3.4 show that no oxygen exists in the center of the particle (a) prior to heating in air. After heating, a significant increase in the percentage of oxygen is observed in both the edge (b) and center (c) of the particle. As oxidation occurs, it is possible that local temperatures may reach the melting point of $Ta_2O_5$ explaining the lack of multiple cracks

in the shell in the post-heating TEM images. Localized melting of $Ta_2O_5$ would seal the crack, but as this newly formed amorphous oxide crystallizes, new cracks may form.

The D-G model above shows oxidation is kinetically limited when the oxide shell is sufficiently thin. If we assume that cracking of the shell prevents the reaction from proceeding to the diffusion limited regime, we can calculate the effective activation energy for oxidation using the calculated rate constant for the linear region and the Arrhenius equation. The relative time required to heat the particles to 850 $^oC$ at $10^5$ K/s with a 1 ms hold is significant in contrast to rapid heating to 500 $^oC$ and holding for 10 ms. Theoretical shell growth, assuming a kinetically limited oxidation mechanism, during the course of the entire heating to 850 $^oC$ experiment is shown in Figure 3.S1. Iterative calculations determined the $E_a$ required to match the experimentally measured shell growth of 4.6 nm is ~65 kJ/mol (0.674 eV).

SAD patterns before and after rapid heating are shown in Figure 3.5. Before heating, crystalline Ta from the core of the particle is observed, but no crystalline $Ta_2O_5$ is apparent. After heating, fringe lines corresponding to both crystalline Ta and crystalline $Ta_2O_5$ are visible. The clustered $Ta_2O_5$ fringe lines imply the formed $Ta_2O_5$ has a preferred orientation with crystalline oxide growth occurring on specific planes.

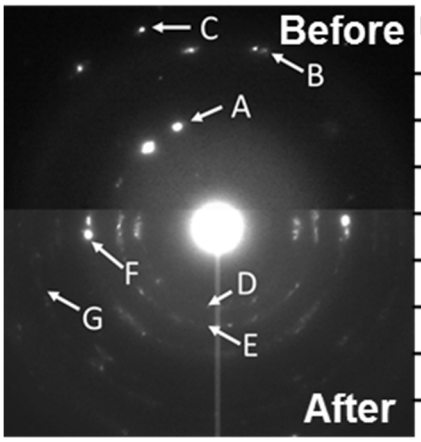


| Measured d spacing (Å) | $Ta_2O_5$ (Pccm) | Ta (Im-3m) |
|---|---|---|
| (A) 2.35 | | 2.319 (101) |
| (B) 1.36 | | 1.339 (112) |
| (C) 1.17 | | 1.16 (220) |
| (D) 3.88 | 3.89 (002) | |
| (E) 3.12 | 3.152 (110) | |
| (F) 2.38 | 2.422 (-200) | 2.32 (101) |
| (G) 1.65 | 1.657 (0-22) | 1.64 (020) |
| ICSD # | 236386 | 53793 |

***Figure 3.5.*** *SAD patterns of particle shown in Figure 3.4 before and after heating in air to 850 °C at $10^5$ K/s and held for 1 ms.*

HRTEM images in Figure 3.6A reveal little crystallization in the oxide shell after the series of heating ramps to 500 °C (30 ms in total), but crystallization is clearly observed after being heated to 850 °C for 1 ms in Figure 3.6B (also confirmed by SAD in Figure 3.5). These results show that rapid heating to 850 °C results in a faster diffusion based oxidation mechanism that may be attributed to cracks forming in the oxide shell.

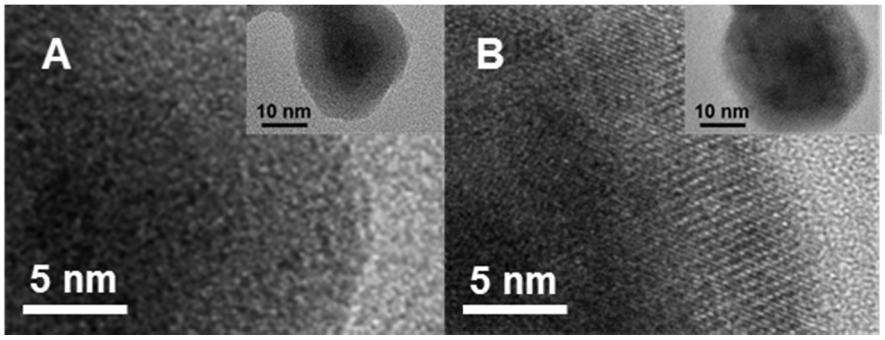


***Figure 3.6.*** *HRTEM images of Ta nanoparticles after being heated in air to 500 °C multiple times (30 ms in total) (A) and to 850 °C for one time only (B); both at a heating rate of $10^5$ K/s.*

*3.3.2. Ta based nanothermites*

*T-Jump analysis of Ta based nanothermites*

Various nTa based nanothermites were investigated using the same T-jump ignition technique as above. The ignition temperatures were measured in a vacuum environment (~$10^{-6}$ torr) to eliminate the impact of ambient gas phase oxygen on ignition. The oxygen release temperature of the pure metal oxides was plotted vs. ignition temperature of nTa and nAl based thermites as shown in Figure 3.7.

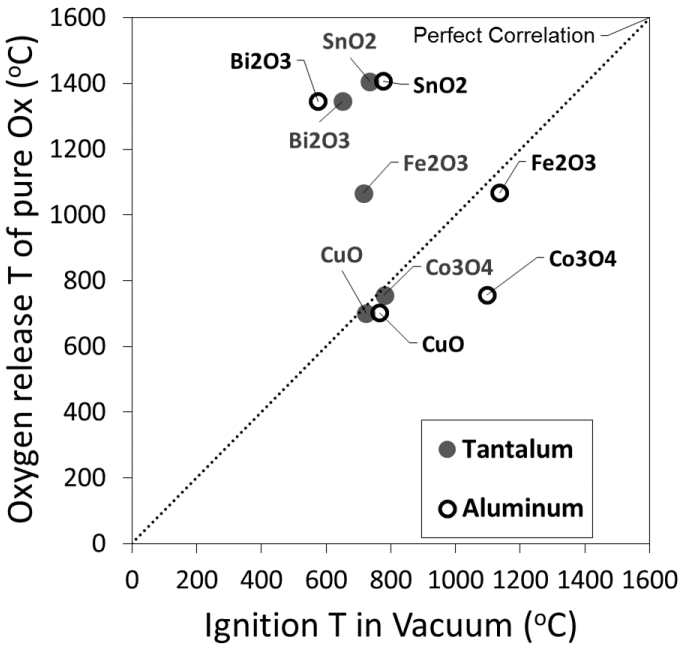


***Figure 3.7.*** *Oxygen release temperature of neat metal oxide vs. ignition temperature of nTa and nAl based thermites.*

Ignition temperatures for the Ta based nanothermites appear to be independent of oxidizer type. In some cases, the ignition temperatures vary greatly from the corresponding Al based nanothermites, with the greatest disparity being between the $Fe_2O_3$ nanothermites. Post-combustion products from the T-Jump ignition in air of Ta/CuO nanothermite were imaged using a previously published method and results are discussed in the Supporting Information.[29] One important result not shown in Figure 3.7 is that the Ta/$WO_3$

nanothermite did not ignite under these heating conditions (~24 ºC to ~1200 ºC in 3ms), but Al/$WO_3$ nanothermite has been previously shown to ignite at 757 ºC in an identical setup.[11]

Table 1 shows the theoretical enthalpy of reaction per mole of metal fuel and adiabatic flame temperature for each nanothermite in Figure 3.7. The theoretical adiabatic flame temperatures were calculated using Cheetah 6.0 equilibrium code at a constant pressure.

***Table 3.1.*** *Theoretical enthalpy of reaction per mole of metal fuel and adiabatic flame temperature calculated using Cheetah 6.0 equilibrium code at constant pressure for each nanothermite.*

| | Ta | | Al | |
|---|---|---|---|---|
| | $\Delta H_{rxn}$ (kJ/mol Ta) | Adiabatic Flame Temperature (K) | $\Delta H_{rxn}$ (kJ/mol Al) | Adiabatic Flame Temperature (K) |
| **CuO** | -633 | 2842 | -604 | 2845 |
| **$Fe_2O_3$** | -335 | 1963 | -425 | 3132 |
| **$Co_3O_4$** | -455 | 2462 | -497 | 3169 |
| **$SnO_2$** | -301 | 3290 | -405 | 3697 |
| **$Bi_2O_3$** | -548 | 2283 | -553 | 3191 |
| **$WO_3$*** | -321 | - | -417 | - |

*$WO_3$ not in Cheetah 6.0 Database

The adiabatic flame temperatures are lower for all Ta based nanothermites, with the exception of the CuO containing nanothermite where the temperatures are approximately equivalent. There does not appear to be a trend between enthalpy of reaction, $\Delta H_{rxn}$, and the ignition temperatures measured in Figure 3.7. The Ta/$Fe_2O_3$ system has a lower $\Delta H_{rxn}$ than Al/$Fe_2O_3$ yet ignites at a lower temperature.

One possible explanation for the discrepancies in ignition temperatures of Ta and Al based nanothermites is that alloying reactions unique to the Ta system my decrease the

onset temperature of reaction. A phase diagram for $Ta_2O_5$ and $Fe_2O_3$ generated using density functional theory (DFT) calculations shows the $TaFeO_4$ alloy can be formed with an enthalpy of formation of -2.5 kJ/mol.[30-32] No stable alloy exists for the $Al_2O_3/Fe_2O_3$ system. Unfortunately, this pattern does not hold true for the $Co_3O_4$ containing thermites, which also show a large ignition temperature difference. Neither system forms a stable alloy with $Co_3O_4$, therefore it is more likely that something unique to nTa and independent of the metal oxide is the cause for the trend in Figure 3.7. As stated above, the $Ta/WO_3$ nanothermite did not ignite under these conditions, contradictory to previous studies on sol-gel derived $Ta/WO_3$ thermites that ignited between 465 $^oC$ and 670 $^oC$.[19] This could be due to differences in the microstructure of the composite, heating environment, and heating rate. In addition, the sol-gel samples were pre-heated to 300-400 $^oC$ before ignition tests and they also employed amorphous $WO_3$ where we used crystalline $WO_3$.

For each of the Ta based nanothermites, ignition occurs at or below the oxygen release temperature for the corresponding metal oxide. We propose that the metal oxide must wet the surface of the nTa for ignition to occur due to Ta being an immobile fuel under these conditions. Each of the Ta based nanothermites in Figure 3.7 ignite fairly close to 700 $^oC$ whereas the Al based nanothermites have a much wider range of ignition temperatures. The TGA/DSC results in Figure 3.1A so an exotherm resulting from the crystallization of $Ta_2O_5$ with an onset temperature of 600 $^oC$ and peak temperature of 630 $^oC$ at low heating rates. Analysis of the crystallization of amorphous $Ta_2O_5$ thin films by Kim et al. showed that crystallization rates rapidly increased at higher temperatures.[18] We propose that at high heating rates, the crystallization of the amorphous shell releases enough energy in a short amount of time at the nTa/metal oxide interface to initiate reaction

between the fuel and oxidizer. In the case of Al, based thermite reactions, Al goes through an endothermic phase change (melting) neat the crystallization temperature of its oxide shell. With $Al_2O_3$ making up only 19 wt. % of nAl, the net process in this temperature regime would be endothermic as energy released from crystallization would go into the melting of Al. For the Ta case, the metal core does not go through any phase changes near the crystallization temperature of the oxide shell, therefore the energy released from crystallization will locally heat the particle. Similar conclusions on crystallization induced ignition were drawn by Cervantes et al. for the sol-gel derived $Ta/WO_3$ thermite system where they saw decreased ignition temperatures when amorphous $WO_3$ was employed.[21] These types of surface interactions were further probed using high-high heating rate TEM for $Ta/Fe_2O_3$ and Ta/CuO nanothermites below.

*High heating rate TEM of Ta based nanothermites*

The $Ta/Fe_2O_3$ nanothermite system showed the largest disparity between nAl and nTa based systems warranting a closer look at the reaction mechanism. $Ta/Fe_2O_3$ nanothermite was heated in the TEM at $10^5$ K/s to 1200 $^oC$ and held for 1 ms. Sullivan et al. preformed a similar study using the same in-situ high heating rate TEM technique with an Al based thermite system and a reactive sintering reaction mechanism was supported.[9] Figures 3.8A and 3.8B show before and after heating TEM images where the $Fe_2O_3$ appears to wet the surface of the Ta to allow for oxygen to diffuse through the $Ta_2O_5$ shell to oxidize the Ta. Unlike Al, Ta does not sinter at areas that are not in contact with the $Fe_2O_3$ under these heating conditions as shown by the maintained nanostructure of parts of the Ta aggregate shown in Figure 3.9B, which again proves wetting the Ta fuel surface by oxidizer

is the crucial for its ignition. The added heat at the interface may be promoting the reactive sintering between the nTa and $Fe_2O_3$.

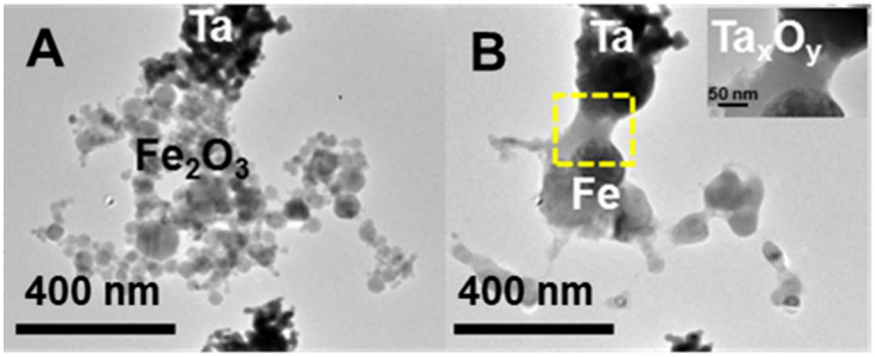


***Figure 3.8.*** *TEM images of $Ta/Fe_2O_3$ nanothermite before (A) and after (B) being heated to 1200 °C at a heating rate of $10^5$ K/s and held for 1 ms, and HRTEM image of interface after heating (inset).*

Ta/CuO nanothermite was also rapidly heated in the TEM to 1200 °C at a heating rate of $10^5$ K/s and held for 10 ms. TEM images shown in Figure 3.S3 show a similar "wetting" phenomenon as seen in the $Ta/Fe_2O_3$ system. EDS results show that that CuO is fully reduced to Cu and even at a location away from the interface, Ta is oxidized, showing the ability for oxygen to be transported throughout the Ta aggregate, even in a vacuum environment.

*Modeling the burn time of Ta/CuO nanothermite*

Using the experimentally determined activation energy for oxidation of 65 kJ/mol described above, a kinetically limited shrinking core model was used to determine a theoretical burn time for the Ta/CuO nanothermite. This model has been previously employed to model the oxidation of titanium and zirconium nanoparticles.[33] For our calculations, we assumed a 33 nm nTa particle as depicted in Figure 3.5. We also ignored heat losses from convection and radiation, but limited the maximum achieved temperature to the adiabatic flame temperature for Ta/CuO (2842 K) as shown in Table 1. The rate

constant at each time step in the model was calculated using the Arrhenius equation below with the experimentally determined activation energy of 65 kJ/mol:

$$k = k_o e^{-E_a/(k_B T)}$$

where k is the diffusion coefficient at a given temperature, $E_a$ is the activation energy for oxidation, $k_B$ is the Boltzmann constant, and T is the temperature. The maximal reaction coefficient,$k_o$, of 3.96 x $10^6$ nm/ms was determined from the value extrapolated from successive heating to 500 °C and single heating ramp to 850 °C. The oxygen concentration used in the model was determined by using a stoichiometric amount of CuO in the combustion cell with a total nanothermite mass of 25 mg and volume of 13 $cm^3$. The oxygen content in the model was finite, therefore oxygen concentration decreased as it was consumed by the nTa. The kinetically limited shrinking core model for reaction and combustion cell experimental results are shown in Figure 3.9.

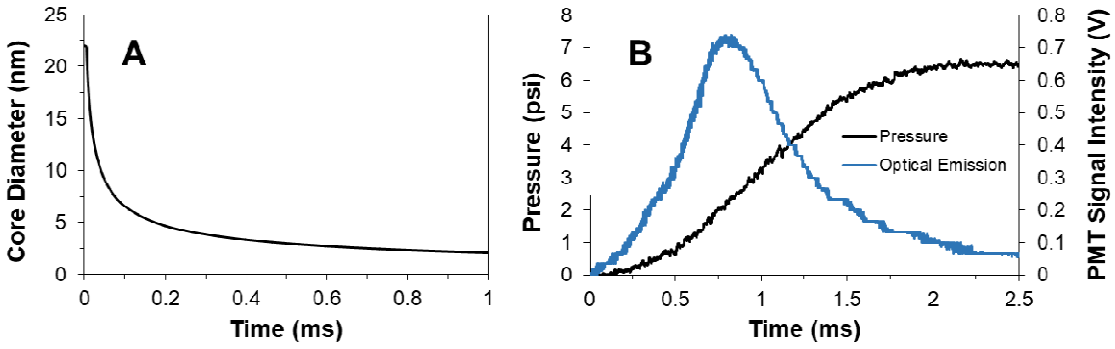


***Figure 3.9.*** *Kinetically limited shrinking core model for reaction using* $E_a$ *of 65 kJ/mol (A) and combustion cell experimental results (B) for the Ta/CuO nanothermite reaction.*

The kinetically limited shrinking core model shows that the core diameter has shrunk by ~90% in 0.9 ms (Figure 3.9A). The optical emission from the combustion cell experiment shows a burn time of ~2 ms (Figure 3.9B), which is in good agreement with this model. The combustion cell was purged with argon prior to ignition to ignore the

effects of ambient oxygen on the reaction mechanism. It is expected that the experimental burn time would be slightly longer as the material is a loose powder ignited by a resistively heated nichrome wire where the model calculates oxidation of a single particle.

*3.3.3. nTa oxidation mechanism summary*

Two distinct nTa oxidation mechanisms are apparent for nTa reacting with gas phase oxygen: a slow heating rate, low temperature oxidation resulting in the formation of amorphous $Ta_2O_5$ and a rapid oxidation caused by the crystallization of amorphous $Ta_2O_5$ creating cracks in the shell.

The Ta nanothermite reaction mechanism is controlled by reactive sintering with metal oxide. The metal oxide must "wet" Ta because Ta is immobile in the temperature range of ignition. Rapid crystallization of the oxide shell leads to heat release at the interface promoting sintering with the metal oxide. nAl also undergoes crystallization of its oxide shell, but the net energy at interface is endothermic due to the melting of the Al core, which makes up 81 % of the mass of a nAl particle. The exothermic crystallization of the $Ta_2O_5$ shell (Figure 3.1) may be attributing to the initiation of localized reactive sintering with the $Fe_2O_3$. This could also explain the trend in ignition temperatures seen in Figure 3.7 where the ignition temperature for nTa based thermites seems to be independent of the metal oxide employed.

*3.4. Conclusion*

This study probed the importance of oxide shell crystallization in the oxidation mechanism of Ta nanoparticles and nanothermites. High heating rate TEM analysis showed that oxide shell growth occurred slowly when heated in air below 500 $^{o}$C and was amorphous. When heated in air to 850 $^{o}$C, oxide shell growth happened rapidly and

crystallization of the shell led to cracks that may attribute to the enhanced oxygen diffusion rates. When investigating the nTa oxidation mechanism with a condensed phase oxidizer, ignition temperatures were independent of the employed metal oxide, unlike corresponding Al nanothermites. We propose that the rapid oxide shell crystallization of nTa contributes enough energy to the shell/oxidizer interface that reactive sintering is induced and kinetically limited oxidation occurs. An activation energy for oxidation was experimentally determined to be 65 kJ/mol from the D-G model and was used to model the burn time of the Ta/CuO nanothermite system.

# Chapter 4: Oxidation and Decomposition Mechanisms of Air Sensitive Aluminum Clusters at High Heating Rates*

*Summary*

Molecular near zero oxidation state clusters of metals are of interest as fuel additives. In this work high heating rate decomposition of the Al(I) tetrameric cluster, $[AlBr(NEt_3)]_4$ (Et = $C_2H_5$), was studied at heating rates of up to 5 x $10^5$ K/s using temperature-jump time-of-flight mass spectrometry (T-jump TOFMS). Gas phase Al and $AlH_x$ species were rapidly released during decomposition of the cluster, at ~220 ºC. The activation energy for decomposition was determined to be ~43 kJ/mol. Addition of an oxidizer, $KIO_4$, increased Al, AlO, and HBr signal intensities, showing direct oxidation of the cluster with gas phase oxygen.

*4.1. Introduction*

Metal fuels such as aluminum have been employed as additives for propellants and explosives due to their high volumetric energy densities. In a recent study, we demonstrated burn rate enhancements in a liquid hydrocarbons using a hydrocarbon soluble molecular aluminum cluster, with a near zero oxidation state, as an accelerator [1]. Specifically, there is a significant enhancement in droplet burn rate with small additions of a Al(I) tetrameric cluster, $[AlBr(NEt_3)]_4$ (Et = $C_2H_5$) [1]. While the combustion characteristics of aluminum cluster materials are largely unknown, the more well-studied nanosized metal particles show faster reaction kinetics and lower ignition temperatures relative to their micron-sized analogs [2]. However, with decreasing particle size, the

* The results presented in this chapter have been previously published and are reprinted with permission from: DeLisio, J.B.; Mayo, B.H..; Guerieri, P.H.; DeCarlo, S.; Ives, R.; Bowen, K.; Eichhorn, B.W.; Zachariah, M.R., Oxidation and decomposition mechanisms of air sensitive aluminum clusters at high heating rates, *Chem. Phys. Lett.,* **2016**, 661, 168. 

contribution of the native oxide layer to the total mass of the particle significantly increases , thereby reducing the energy content of the particles [3,4]. In addition, the native oxide creates a barrier between the metallic fuel and any oxidizer that limits the reaction kinetics. Molecular aluminum compounds with sufficient ligand stabilization offer an intriguing alternative to nano-aluminum fuels in that oxide coatings may be circumvented giving rise to potentially new combustion mechanisms and enhanced oxidation kinetics.[5,6] However, until fundamental properties of these clusters are studied, such as their compatibility with oxidizers in a composite, their utility as a fuel remains unclear.

Because the oxidation mechanisms of ligated Al clusters are unknown, their combustion characteristics are difficult to predict. For example, if combustion of the ligand shell precedes the combustion of the Al core, then any enhancement in combustion rate relative to Al NPs may be overshadowed. Simulations by Hooper and coworkers [7-9] suggest that oxidation of aluminum precedes that of the ligand shell in $Cp^*_4Al_4$ clusters but mechanistic experimental data on these processes are necessary to further develop these models. To study aluminum cluster oxidation, we require the ability to investigate air-sensitive compounds via thermally-activated chemistry on a time scale and with heating rates nominally associated with an ignition event encountered in combustion, as previous studies have demonstrated that reaction pathways can vary greatly between slow and fast heating [10-12]. In prior work, we have employed a temperature-jump time-of-flight mass spectrometer (T-jump TOFMS) to probe decomposition of nitrocellulose and RDX [13], the reaction mechanisms of nanothermite systems [14-17], and activation energies for oxygen release from metal oxides [18].

In this study, we build on our previous work on T-jump TOFMS with the incorporation of an air sensitive sample holder (ASSH) capable of heating samples at rates of up to 5 x $10^5$ K/s [13]. The ASSH enables loading of air sensitive samples in a glove box and transfer to the TOFMS without ambient exposure. In this paper we study the high heating rate decomposition of $[AlBr(NEt_3)]_4$ in an oxygen-free environment as well as its oxidation with bismuth oxide ($Bi_2O_3$) and potassium periodate ($KIO_4$). These results also demonstrate that a molecular aluminum fuel $(AlBr(NEt_3)]_4$,)can be in immediate physical contact with a strong oxidizer ($KIO_4$ or $Bi_2O_3$) and remain stable under an inert atmosphere.

*4.2. Experimental*

*4.2.1. Materials*

The tetrameric Al(I) cluster $[AlBr(NEt_3)]_4$ was synthesized from an AlBr•$NEt_3$ starting material produced in a Schnöckel-type metal halide co-condensation reactor (MHCR) [19-21]. A rendering of the cluster's crystal structure is shown in Figure 4.1.

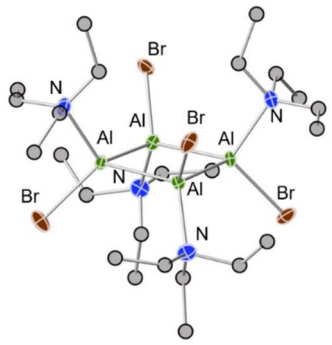


***Figure 4.12.*** *X-ray crystal structure of $[AlBr(NEt_3)]_4$ [21]. Thermal ellipsoids drawn at 50% probability level. Unlabeled grey spheres represent carbon; hydrogen atoms omitted for clarity.*

Bismuth oxide ($Bi_2O_3$) nanopowder was purchased from Sigma Aldrich. Potassium periodate ($KIO_4$) nanoparticles were prepared by dissolving $KIO_4$ (Sigma Aldrich) in distilled water and then using a previously described aerosol based spray drying procedure

[22]. Hexane was dried over sodium benzophenone ketyl and stored over activated 3Å molecular sieves.

*4.2.2. Air Sensitive Sample Holder*

A custom-built air-sensitive sample holder (ASSH) was used with a previously described temperature-jump time-of-flight mass spectrometer (T-jump TOFMS) [13]. The ASSH uses a ~25 μm thick aluminum foil membrane to prevent oxygen exposure of the sample while transporting the holder to the TOFMS. The membrane is sealed using a gasket compressed by a threaded cap at the end of a stainless steel housing that surrounds the T-jump probe. A 3D printed collar (designed in SolidWorks and printed using a Stratasys Objet30 Pro) was fixed to the electrical feedthrough of the T-jump probe. This collar punctures the aluminum foil membrane when inserted into the TOFMS.

*4.2.3. Sample Preparation*

Samples were prepared in a glovebox with 2 mg of combined solids suspended in 1 mL of dry hexane. Mixed samples containing the $[AlBr(NEt_3)]_4$ cluster and $Bi_2O_3$ or $KIO_4$ (1:3 cluster to oxidizer ratio by mass) were sonicated for 10 minutes in a sealed, oxygen-free vial. Samples were loaded as a suspension in hexanes via autopipette onto 76 μm platinum (Pt) wires held by the ASSH within the glove box. The ASSH sample holder was then capped under inert atmosphere, removed from the glovebox, and transferred to the TOFMS.

*4.2.4. Sample Analysis*

During standard operation, the roughing chamber of the TOFMS is pumped and purged with UHP nitrogen ($N_2$) gas prior to mounting the ASSH. $N_2$ was chosen over argon due its lower background signal intensity. A positive pressure of $N_2$ is maintained in the

roughing chamber during mounting of the ASSH, after which the aluminum foil membrane is punctured and the roughing chamber evacuated to ~0.5 torr. Once the roughing chamber is evacuated, the gate valve to the main chamber of the TOFMS is opened and the sample inserted. When the system is under vacuum, the platinum wires are resistively heated within the TOFMS (sampling rate = 10 kHz) with time resolved wire temperatures calculated using the Callendar-Van Dusen equation. A 600 MHz digital oscilloscope was used for data acquisition. To perform activation energy analysis, wire heating rates were varied between 1 x $10^5$ and 5 x $10^5$ K/s by increasing or decreasing the pulse width and/or driving voltage of the heating circuit. With the exception of the experiments used in determining the activation energy, a heating rate of ~4 x $10^5$ K/s was employed. All mass spectra signal intensities were normalized to the maximum signal intensity of m/z = 86 (the predominant fragment observed from electron impact ionization of $NEt_3$) unless otherwise noted.

*4.3. Results and Discussion*

*4.3.1. Thermal Decomposition of [AlBr($NEt_3$)]$_4$ During Rapid Heating*

Analysis of the decomposition of [AlBr($NEt_3$)]$_4$ was performed on both oxidized and unoxidized samples. Analysis of the data was complicated by the fact that the mass of aluminum ion (m/z = 27) also corresponds to the mass of any ethyl fragments generated by the direct decomposition of triethylamine ($NEt_3$). Unfortunately, the analogous trimethylamine and tripropylamine complexes of AlBr are not known, which precludes the resolution of the mass degeneracy by chemical substitution. When ionized using electron impact ionization, pure $NEt_3$ has multiple mass envelopes between the m/z values of 27 and 101 with the highest relative signal intensity corresponding to the m/z = 86 fragment

[23]. Since the peak at m/z 86 is solely a result of $NEt_3$ decomposition, we employed it as an internal reference standard to normalize the signal intensities. Figure 4.2 shows the spectra at the time of the maximum absolute m/z = 86 signal intensity for the unoxidized $[AlBr(NEt_3)]_4$ introduced via ASSH (Figure 4.2a), and after exposure to the ambient atmosphere for ~3 hours (Figure 4.2b).

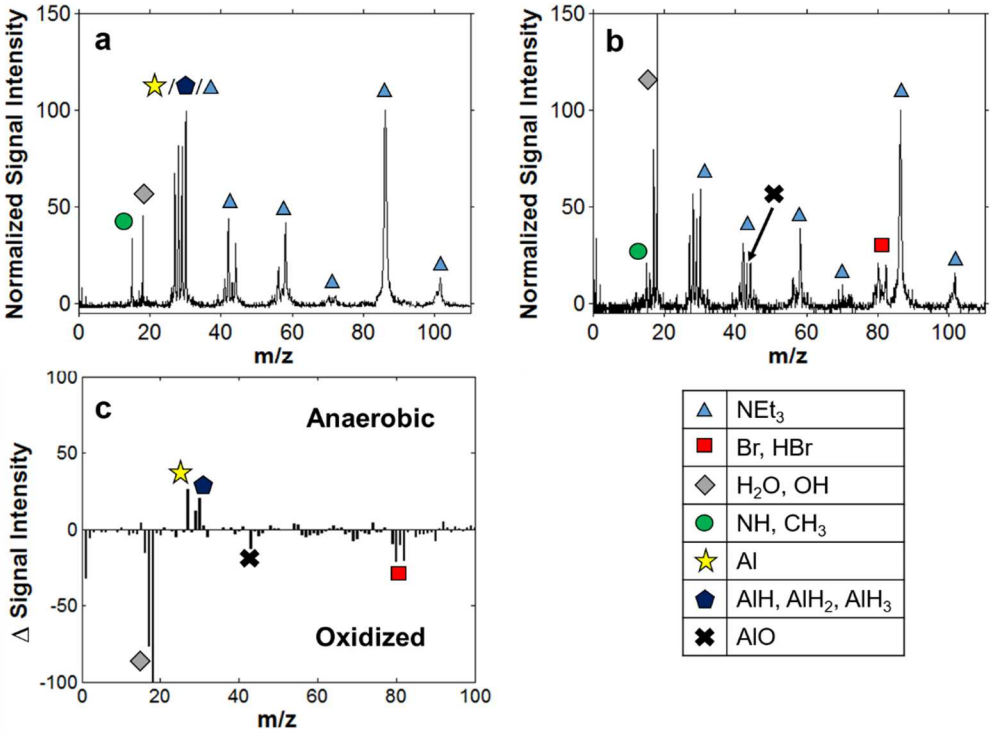


***Figure 4.13.*** *Normalized MS at time of maximum m/z=86 signal intensity (0.8 ms, ~330 $^oC$) for the anaerobic (a) and oxidized (b) Al(I) tetrameric cluster heated at ~4 x $10^5$ K/s and normalized difference spectrum (c) of anaerobic – oxidized.*

We find that peaks corresponding to m/z values of 27, 28, 29, and 30 have much higher signal intensities prior to oxidation (Figure 4.2a). When exposed to oxygen, the $NEt_3$ remains intact but the Al in the cluster oxidizes, resulting in decreased signal intensities in the 27-30 mass envelope seen in Figure 4.2b. The spectrum of the oxidized cluster in Figure 4.2b also shows an increased $H_2O$ signal intensity and the presence of AlO and HBr species (discussion below). To highlight the differences in the decomposition of unoxidized and

oxidized $[AlBr(NEt_3)]_4$, a difference plot was generated using the normalized spectrum at the time of maximum m/z = 86 signal intensity for the oxidized sample and the unoxidized sample as seen in Figure 4.2c. The difference spectrum removes all peaks associated with $NEt_3$ decomposition and highlights the Al containing species in the anaerobic sample and the $H_2O$, AlO, and HBr in the oxidized signal. The increased normalized signal intensity of the m/z = 27 peak of the unoxidized sample affirms that reactive aluminum is present in the system and is being generated during decomposition of the cluster. During rapid decomposition under anaerobic conditions, the Al(I) tetrameric cluster will presumably react with hydrogen-containing fragments from the $NEt_3$. Thus, we conclude that signals in the 27-30 m/z range in the difference spectrum (Figure 4.2c) correspond to Al, AlH, $AlH_2$, and $AlH_3$.

The observed Br and HBr in the oxidized sample is a result of hydrolysis of $[AlBr(NEt_3)]_4$[4]., In the presence of air, the aluminum in the complex reacts with ambient oxygen and water to form HBr and AlO containing species (e.g. $Al_2O_3$, Al(O)OH, etc.). The HBr will react with $NEt_3$ to give the non-volitle $HNEt_3Br$ salt that decomposes back HBr and $NEt_3$ when heated. The formation of this salt prevents $NEt_3$ from evaporating/decomposing during air oxidation, allowing the use of $NEt_3$ fragments as an internal standard for our study. Previous temperature-programmed reaction (TPR) experiments have detected generation of HBr when heating $[AlBr(NEt_3)]_4$ in the presence of water. This observation is consistent with the T-jump TOFMS results for the oxidized and $KIO_4$-containing samples (see Figure 4.S2 and discussion below) [1].

*4.3.2. Reactions of $[AlBr(NEt_3)]_4$ Mixed with Oxidizers*

The next phase of this study proceeded with the introduction of oxidizers to the $[AlBr(NEt_3)]_4$ suspensions. Two different oxygen-containing nanoparticles, $Bi_2O_3$ and $KIO_4$, were physically mixed with the cluster prior to deposition onto the Pt filament. $Bi_2O_3$ is known to have low ignition temperatures in aluminum-based nanothermite compositions and has been shown to initiate reaction through the condensed phase [24]; $KIO_4$ also exhibits low ignition temperatures with aluminum and is known to release gas phase oxygen at a low temperatures prior to ignition [22]. These two oxidizers should provide insight into the reactivity of $[AlBr(NEt_3)]_4$ in the both solid- and gas-phase.

The samples containing $Bi_2O_3$ did not alter the decomposition of the $[AlBr(NEt_3)]_4$ cluster, with no increase in m/z=43 (AlO) signal intensity, implying little discernable contribution from this oxidizer (see Figure 4.S1). As previously stated, $Bi_2O_3$ is believed to oxidize Al nanoparticles by condensed phase transport of oxygen, which implies that the Al(I) tetrameric cluster decomposes before oxygen becomes mobile in the oxidizer. This is further supported by temporal analysis (Section 4.3.3), which shows that the tetramer decomposes several hundred degrees lower than when oxygen becomes mobile, and thus gas-phase decomposition products will have escaped before they have an opportunity to be oxidized. Previous studies have shown that at high heating rates, condensed-phase reaction with $Bi_2O_3$ begins at ~627 $^oC$ for carbon and Al-based thermites [24]. The Al(I) tetrameric cluster decomposes and Al is gasified well below ~627 $^oC$, preventing the $Bi_2O_3$ from oxidizing the Al (decomposition temperatures discussed in section 3.3). Further, these results demonstrate that $[AlBr(NEt_3)]_4$ is able to be in immediate physical contact and

sonicated with a strong condensed phase oxidizer ($Bi_2O_3$) without reaction occurring during the sample preparation for this experiment.

The mass spectrum for the rapidly heated $[AlBr(NEt_3)]_4/KIO_4$ mixture (Tet-$KIO_4$) in Figure 4.S2 shows the detection of AlO and HBr species indicating that oxidation of the $[AlBr(NEt_3)]_4$ has occurred during heating. An increased amount of $H_2O$ is observed that is due to the oxidation of the cluster's ligands in addition to any residual $H_2O$ within the $KIO_4$ that is released during decomposition. A decrease in the m/z = 15, corresponding to $NH/CH_3$, is also apparent when $KIO_4$ is present. The effects of gas phase oxygen generated by the $KIO_4$ on the reaction mechanism of the rapidly heated $[AlBr{\bullet}NEt_3]_4$ is further described in the temporal analysis section.

As shown with the pure tetramer samples, the species overlap between Al and AlH and $NEt_3$ fragmentation is still an issue when analyzing samples mixed with an oxidizer, therefore the data were treated in the same fashion as previously described. Table 4.1 lists normalized integrated signal intensities for m/z = 27 and 30 of the unoxidized Al(I) tetrameric cluster and the mixture with $KIO_4$.

***Table 4.2.*** *Normalized m/z=27 and m/z=30 integrated signal intensity values during rapid heating of the unoxidized Al(I) tetrameric cluster (Tet) and Al(I) tetrameric cluster mixed with $KIO_4$ (Tet+$KIO_4$).*

| **Sample** | **Integrated Signal Intensity m/z = 27** | **Integrated Signal Intensity m/z = 30** | **Ratio 27:30** |
|---|---|---|---|
| Tet | 72 | 91 | 0.79 |
| Tet + $KIO_4$ | 72 | 62 | 1.16 |

The pure and mixed samples both show identical integrated signal intensities for the m/z = 27 peak during rapid heating. The integrated signal intensity for the m/z = 30 peak decreases when $KIO_4$ is added to the system, therefore the ratio of the m/z =27 to m/z = 30 is higher for the mixture. The m/z = 30 signal intensity is partially attributed to the formation of $AlH_3$ under anaerobic conditions. The integrated signal intensity of m/z = 43 was doubled when $KIO_4$ was added due to the aforementioned formation of AlO. In the presence of $KIO_4$, the more favorable AlO species is formed and the amount of $AlH_x$ is diminished.

*4.3.3. Temporal Speciation*

The previous TPR experiments on $[AlBr(NEt_3)]_4$ employed a much slower heating rate (10 $^oC$/min) than the T-jump TOFMS system, and the onset of cluster decomposition was observed at ~50 $^oC$ [1]. The TPR experiments, however, did not examine species with an m/z less than 50, therefore no conclusions on gas phase aluminum release can be drawn. As shown by the spectra in Figure 4.2a, the Al(I) tetrameric cluster releases gas phase Al resulting in the increased m/z = 27 signal intensity in comparison to the oxidized sample in Figure 4.2b. For the oxidized and unoxidized $[AlBr(NEt_3)]_4$, all detected species appear in the time resolved spectra concurrently pointing towards a single step decomposition of the cluster. In Figure 4.3, we show temporal results from T-jump TOFMS for the m/z = 27 species for neat $[AlBr(NEt_3)]_4$ and Tet-$KIO_4$. Figure 4.3 also shows that at a heating rate of ~4 x $10^5$ K/s, decomposition of the anaerobic neat tetramer occurs at ~220 $^oC$. The Al contribution to the m/z = 27 signal over time for unoxidized $[AlBr(NEt_3)]_4$ is shown in Figure 4.S3.

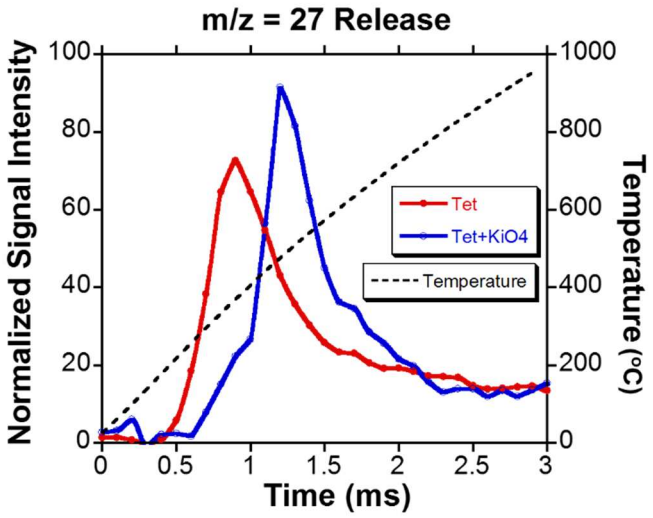


***Figure 4.14.*** *m/z = 27 release over time for the pure Al(I) tetrameric cluster (Tet) and the Al(I) tetrameric cluster mixed with $KIO_4$ (Tet-$KIO_4$).*

The addition of $KIO_4$ resulted in a delayed, yet higher intensity m/z = 27. As shown in Table 4.1 above, both the pure and mixed samples had the same integrated signal intensities for the m/z = 27 peak. The addition of $KIO_4$ delays the detection of gas phase Al in the MS, but the amount detected is unchanged. We propose that some of the gas phase Al released from cluster decomposition reacts with the surface of the $KIO_4$ particles during cluster decomposition. The sharp high intensity m/z = 27 peak in Figure 4.3 occurs concurrently with $KIO_4$ decomposition.A similar delay is observed with $Bi_2O_3$ as well, where $Bi_2O_3$ has no oxidizing effect (see Figure 4.S4). The gas phase Al on the surface of the $Bi_2O_3$ desorbs before the oxygen in the $Bi_2O_3$ is able to react, therefore the m/z = 27 peak is delayed, but does not have a higher intensity as seen in the $KIO_4$ mixture.

Samples containing $KIO_4$ appear to alter the decomposition of $[AlBr(NEt_3)]_4$, as observed in Figure 4.4, which shows the temporal behavior of m/z =43, which can be primarily be attributed to AlO. The m/z of 43, for the pure tetramer, corresponds to a minor

fragment from $NEt_3$ ionization. Thus the observed enhanced m/z 43 with $KIO_4$ addition can be attributed to oxidation of Al to AlO by gas phase oxygen from $KIO_4$.

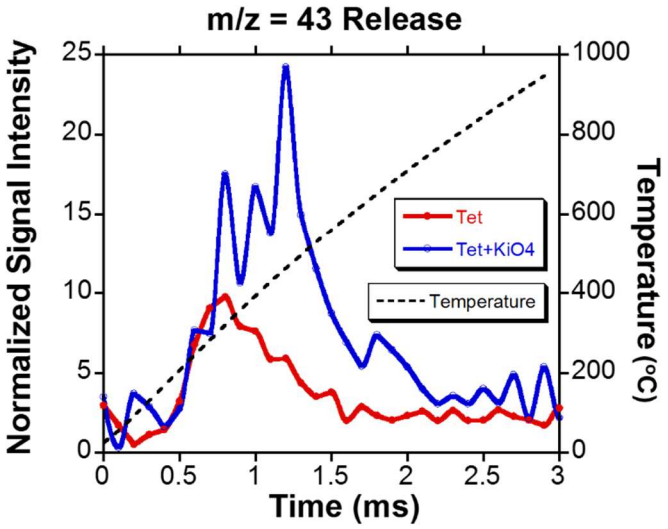


***Figure 4.15.*** *Species over time plot of m/z=43 for the pure Al(I) tetrameric cluster (Tet) and the Al(I) tetrameric cluster mixed with $KIO_4$ (Tet-$KIO_4$).*

This attribution is further confirmed by the temporal $O_2$ release seen in Figure 4.5 between neat $KIO_4$ and $KIO_4$ mixed with $[AlBr(NEt_3)]_4$ tetramer (Tet-$KIO_4$). These signal intensities were normalized to m/z = 39, corresponding to potassium being released from the decomposition of $KIO_4$.

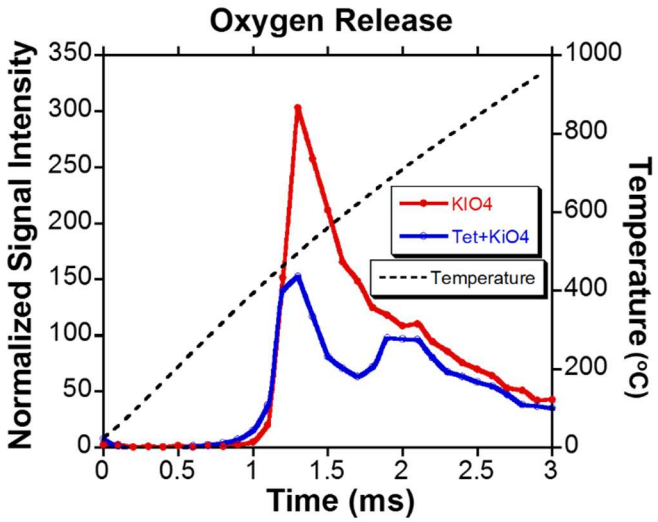


***Figure 4.16.*** *Oxygen release over time for pure $KIO_4$ and the Al(I) tetrameric cluster mixed with $KIO_4$ (Tet-$KIO_4$).*

Previous work has shown $KIO_4$ to undergo a two stage decomposition, which is consistent with the results shown in Figure 4.5 [22]. The onset temperatures for decomposition of the $KIO_4$ are identical for both neat $KIO_4$ and Tet-$KIO_4$, but a significant decrease in the first stage of oxygen release is observed for Tet-$KIO_4$. This decrease can be attributed to the oxygen being consumed by the reaction with Al from the $[AlBr(NEt_3)]_4$ cluster. It is also important to note that the peak $O_2$ signal intensity occurs at the same time/temperature as the peak m/z = 43 signal intensity of the Tet-$KIO_4$ in Figure 4.4, further supporting the proposed mechanism of Al from the cluster combining with gas phase $O_2$ generated by the $KIO_4$ to form AlO.

*4.3.4. Activation Energy for Al(I) Tetrameric Cluster Decomposition*

The activation energy for the decomposition of the Al(I) tetrameric cluster was obtained using the Flynn-Wall-Ozawa isoconversional method, similar to previous work done by Jian et al. using T-jump TOFMS [18]. The decomposition temperature was defined

as the temperature of the Pt filament when the highest intensity $NEt_3$ fragment, m/z = 86, was first detected by the TOFMS. Figure 4.6a shows the decomposition temperature as a function of heating rate, which as expected, increases with increasing heating rate. Figure 4.6b shows the resulting Arrhenius plot of heating rate, $\beta$, vs. the inverse of the decomposition temperature and yields an activation energy for decomposition of 42.8 kJ/mol for $[AlBr(NEt_3)]_4$ .

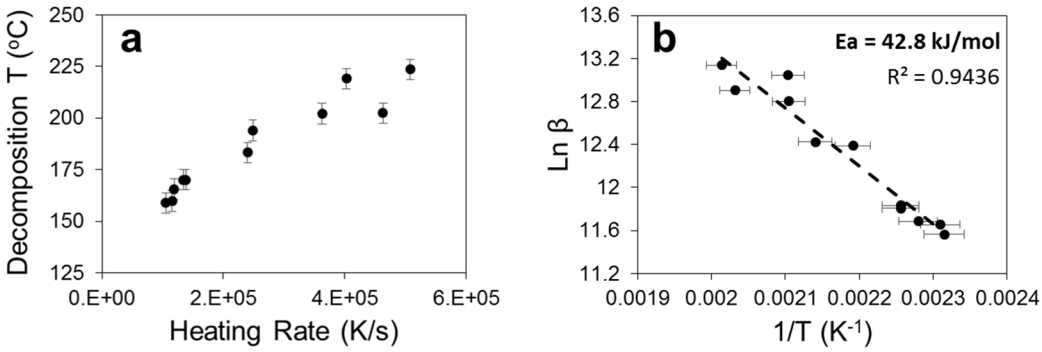


**Figure 4.17.** Decomposition temperature (first appearance of m/z = 86) vs heating rate (a) and Arrhenius plot (b) of rapidly heated unoxidized Al(I) tetrameric cluster.

While the activation energy appears to be small, low activation energies appear to be consistently observed in a variety of systems under high heating rate conditions. For example, the activation energy for oxygen release from CuO nanoparticles at high heating rates was found to be at least 2-3 times lower than that under heating rates consistent with normal TGA measurements [18].

*4.3.5. Al(I) Tetrameric Cluster Reaction Mechanism Summary*

At high heating rates, decomposition of the Al(I) tetrameric cluster, $[AlBr(NEt_3)]_4$, occurs between ~160 and ~220 °C as shown in Figure 4.6a. Decomposition releases $NEt_3$ fragments and gas phase Al, which under anaerobic conditions forms $AlH_x$ species. When heated after exposure to ambient oxygen, an increase in HBr is observed. No significant evidence of a condensed phase oxidation of the cluster was observed as demonstrated by

the lack of AlO species when $Bi_2O_3$ was mixed with $[AlBr(NEt_3)]_4$. In contrast, use of a low temperature gas –generator ($KIO_4$) showed the presence of AlO as a reaction product along with a decrease in $AlH_x$ species. As gas phase oxygen is neccessary for oxidation of this particular Al(I) cluster, future Al cluster/oxidizer systems may be tailored to have simultaneous Al and $O_2$ release to maximize Al oxidation. This work shows that $[AlBr(NEt_3)]_4$ can be intimately mixed and sonicated in a suspension with strong oxidizers ($Bi_2O_3$ and $KIO_4$) without room temperature reactions occurring, demonstrating the potential of aluminum cluster materials as ingredients in energetic formulations.

# Chapter 5: Investigating the Effectiveness of Coated Aluminum Clusters Subjected to High Heating Rates

*Summary*

Aluminum containing cluster materials are of interest for various energetic applications due to their high theoretical energy densities and reaction rates. Further, their solubility in organic solvents and lack of a nascent oxide shell is advantageous, though their air- and moisture-sensitivity poses a challenge when investigating their combustion characteristics. Recently, the decomposition and oxidation mechanisms of an Al cluster has been probed using a newly developed air-sensitive sample holder integrated with a temperature-jump time-of-flight mass spectrometer (T-jump TOFMS). To test the effect of coatings on aluminum cluster fuels to ambient conditions, the well-studied aluminum cluster $[AlCp^*]_4$ was encased in immersion oil. T-jump TOFMS was used to analyze the anaerobic decomposition of $[AlCp^*]_4$ at high heating rates; a strong release of gas phase Al was detected. This technique was employed to measure the effectiveness of the immersion oil coating in preventing cluster oxidation upon exposure to ambient conditions while still being able to release gas phase Al during rapid heating. After exposure to ambient conditions for 1 hour, the coated Al cluster still contained active Al as demonstrated by T-jump TOFMS in addition to thermogravimetric analysis coupled with differential scanning calorimetry (TGA/DSC).

## *5.1. Introduction*

Many energetic materials, including explosives and propellants, have incorporated metal fuels to increase their energy densities; aluminum (Al) is one of the most common

additives. Recent work on the oxidation of Al particles has shown that reaction rates can be drastically increased and ignition temperatures can be reduced when reducing Al particle size down to the nanoscale [1, 2]. However, Al nanoparticles have a nascent oxide shell that limits reaction kinetics and results in a significant decrease in active Al content on a per mass basis when compared to micron sized Al [3]. One approach to increasing the combustion performance of an Al based additive is to employ near zero oxidation state Al-containing cluster materials [4], which have recently demonstrated burn rate enhancements when added to liquid hydrocarbon systems [5].

The main challenge in evaluating the performance of Al clusters is their air-sensitivity. To make use of Al cluster based fuels in practical energetic applications, it would be beneficial to encase the cluster in a binder that, in addition to containing an oxidizer material that can controllably react with the fuel, can limit aerobic oxidation. Recently, a newly developed technique using an air-sensitive sample holder (ASSH) with a temperature-jump time-of-flight mass spectrometer (T-jump TOFMS) was used to study the anaerobic decomposition and reactivity of the Al(I) tetrameric cluster, $[AlBrNEt_3]_4$ (Et = $C_2H_5$) [6]. This technique only requires a small amount of sample and can be used to analyze these materials at high heating rates and time-scales that more accurately represent a combustion event. This material was also shown to be controllably oxidized when physically mixed with potassium periodate ($KIO_4$) and heated.

In this study, we investigate the high heating rate decomposition of one of the most well-studied aluminum cluster compounds, $[AlCp^*]_4$, [7, 8] and use this technique to investigate the effectiveness of an immersion oil coating in the prevention of cluster oxidation. Further, we also study the effect of the immersion oil on Al release from the

cluster. Thermogravimetric analysis coupled with differential scanning calorimetry (TGA/DSC) was also employed to evaluate the stabilization of the Al cluster within the immersion oil.

*5.2. Experimental*

*5.2.1. Sample Preparation*

The $[AlCp^*]_4$ used in this study was prepared using a previously described procedure [7, 9] and its crystal structure is shown in Figure 5.1. Immersion oil was type NVH purchased from Cargille Laboratories. Hexane was dried over sodium benzophenone ketyl and stored over activated 3Å molecular sieves. Pure $[AlCp^*]_4$ samples were prepared by suspending approximately 2 mg of the solid cluster in a small amount of hexane within a glove box to aid in sample deposition to the ASSH and TGA/DSC pan. For the mixed $[AlCp^*]_4$ and immersion oil samples, both constituents were mixed in a scintillation vial with a small amount of hexane for better mixing and to aid in the coating of the Al cluster.

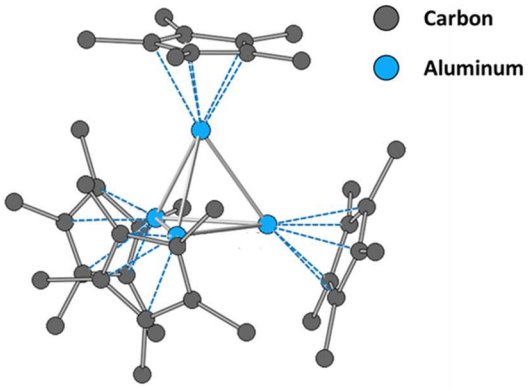


***Figure 5.1.*** *X-ray crystal structure of* $[AlCp^*]_4$.

*5.2.2. T-Jump TOFMS*

A previously described temperature-jump time-of-flight mass spectrometer (T-jump TOFMS) coupled with an air-sensitive sample holder (ASSH) was used for time resolved

speciation analysis at high heating rates of ~4 x $10^5$ K/s and a sampling rate of 10 kHz [6, 10-12]. Samples were deposited via autopipette onto 76 μm platinum (Pt) wires held by the ASSH within a glove box. Oxidized samples were prepared by loading the sample onto the Pt wires within the glove box and then exposing the dry material to air prior to insertion into the TOFMS.

*5.2.3. TGA/DSC*

A SDT Q600 (TA Instruments) thermogravimetric analysis coupled with differential scanning calorimetry (TGA/DSC) system was used to evaluate the pure and coated $[AlCp^*]_4$. Samples (2-4mg) were deposited into alumina TGA/DSC pans via autopipette within a glove box. Anaerobic samples were transferred from the glove box to the TGA/DSC using a capped scintillation vial held in an argon filled plastic bag. Exposed samples were opened to ambient conditions for 1 hour prior to analysis. Each sample was run under argon at a 100 mL/min flow rate and heating rate of 25 $^oC$/min.

*5.3. Results and Discussion*

The high heating rate decomposition of pure $[AlCp^*]_4$ was first analyzed using the ASSH coupled T-Jump TOFMS technique. This technique allows for the collection of a full mass spectrum every 0.1 ms which can be further analyzed to perform temporal analysis of individual m/z signal intensities. For preliminary decomposition product comparison between anaerobic and oxidized $[AlCp^*]_4$, the mass spectra over the course of heating were summed and normalized to their respective m/z = 27 (Al) signal intensities as shown in Figure 5.2.

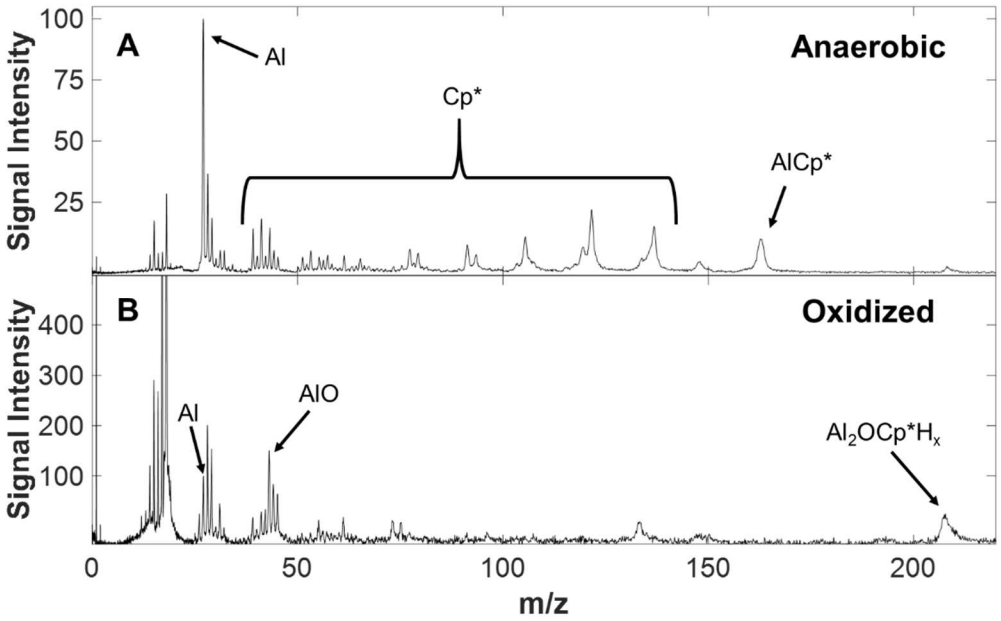


***Figure 5.2.*** *Anaerobic (A) and oxidized (B) $[AlCp^*]_4$ mass spectra summed over the course of heating during T-Jump TOFMS experiments. Both samples were heated at ~$4x10^5$ K/s and spectra are normalized to their respective m/z=27 signal intensity.*

The mass spectrum for the anaerobic sample shows a much higher relative Al signal intensity than the oxidized sample (See Figure 5.2). In addition, the pure Cp* fragments have much lower signal intensities in the oxidized sample, while the AlO peak has increased and an oxidation product, $Al_2OCp^*H_x$ is observed. These results were used as a reference for comparison between anaerobic and air-exposed immersion oil coated samples.

The time resolved Al signal intensity in Figure 5.3A shows the gas phase Al release during rapid heating. The Al release temperature and signal intensity was then used as a metric to determine the effect of an immersion oil coating on the cluster. Pure immersion oil was also analyzed with the T-Jump TOFMS system and results were used as a control for mixture analysis. The mass spectrum of the pure immersion oil contains a peak at m/z=27, most likely corresponding to the $C_2H_3$ fragment, but the temporal release of this

species does not rapidly occur until ~400 ºC, while Al releases at at ~220 ºC for pure $[AlCp^*]_4$ as shown in Figure 5.3. The immersion oil showed a strong peak at m/z=98, most likely corresponding to the $C_7H_{14}$ fragment, that is not seen in the decomposition of anaerobic or oxidized $[AlCp^*]_4$ as seen in Figure 5.3. The pure immersion oil and anaerobic and oxidized mixtures were normalized based on the maximum m/z=98 signal intensity to allow for comparison of the m/z=27 peak. The time resolved release of m/z=98 and m/z=27 for these samples are shown in Figure 5.3B-D.

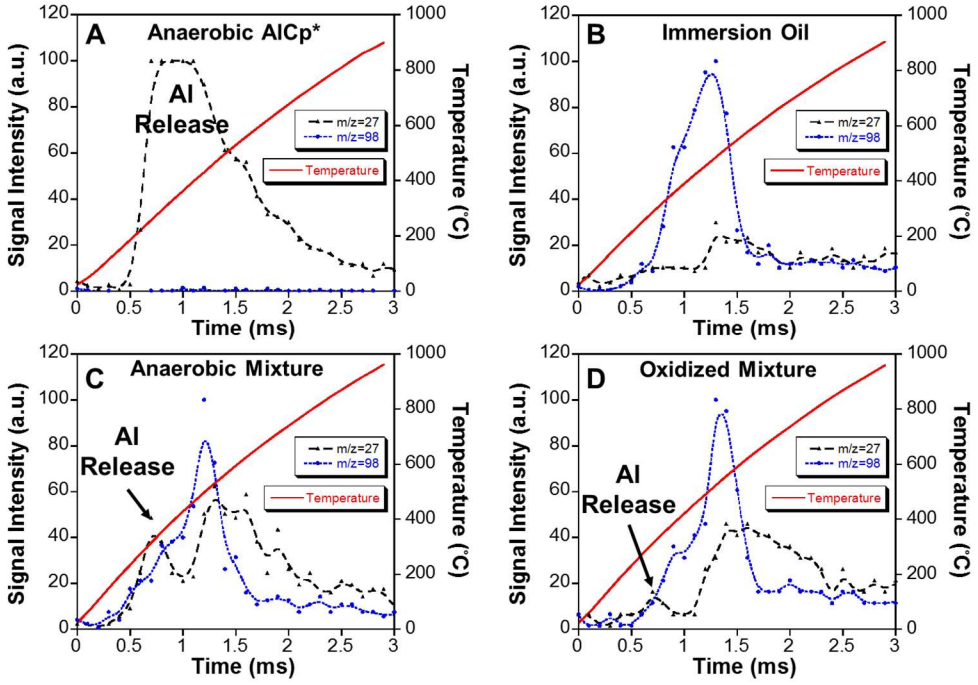


***Figure 5.3.*** *Time resolved release of m/z=27 and m/z=98 fragments during rapid heating (~4 x $10^5$ K/s) of anaerobic $[AlCp^*]_4$ ($AlCp^*$) (A) and immersion oil (B) in addition to anaerobic (C) and oxidized (D) mixtures of the two. All data, with the exception of A, were normalized to the peak m/z=98 signal intensity. A was normalized to the peak m/z=27 signal intensity.*

Both the anaerobic and oxidized mixtures show two separate m/z=27 peaks, with the first having an onset temperature close to that of pure anaerobic $[AlCp^*]_4$. We propose that the first m/z=27 peak corresponds to the release of active Al from the cluster. The

normalized m/z=27 signal intensity is also much higher for both cluster containing samples in comparison to the pure immersion oil. Some gas phase Al may be getting trapped within the immersion oil prior to the decomposition of the immersion oil; the higher relative signal intensity could be due to this Al in addition to $C_7H_{14}$. Further analysis is needed to prove these assumptions. The oxidized sample showed a reduction in Al signal intensity of ~50% after exposure to air for 1 hour, but the presence of the peak in the oxidized sample demonstrates the sample still contains some unoxidized $[AlCp^*]_4$. It is unclear if the Al signal reduction is due to oxidation of some of the material, or due to variation in cluster to immersion oil ratio in the oxidized sample due to the uncertainty in the sample deposition for this experimental setup.

TGA/DSC analysis was performed to validate the effectiveness of the immersion oil coating on the Al cluster. If proven accurate in analyzing these types of air-sensitive systems, this technique could be a valuable asset to gain further insight into the energetics of these systems, as T-Jump TOFMS provides no thermal data. As a control, pure anaerobic $[AlCp^*]_4$ was analyzed and an exothermic decomposition was observed with an onset temperature of ~210 $^oC$ as shown in Figure 5.4A. For comparison, pure $[AlCp^*]_4$ was loaded into the system and exposed to air for 1 hour prior to heating under argon flow as shown in Figure 5.4B. This sample shows a mass loss during exposure to air prior to heating and the decomposition exotherm seen in the anaerobic sample is not observed. Figure 5.4C and 5.4D show the TGA/DSC results of the cluster coated in immersion oil.

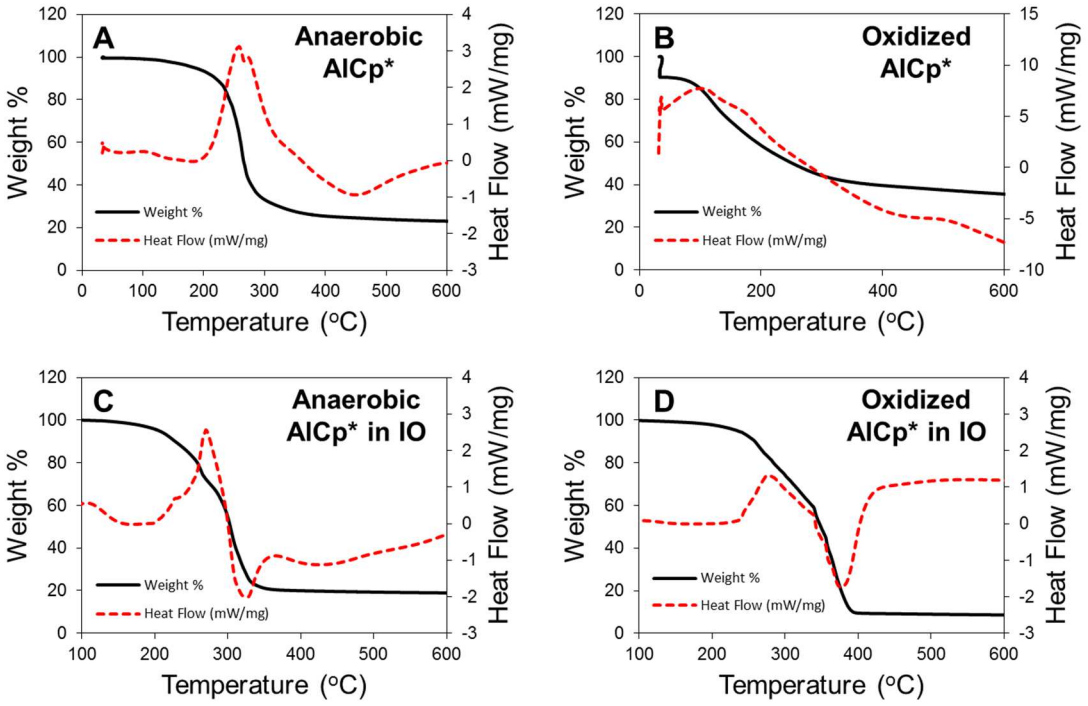


***Figure 5.4.*** *TGA/DSC results of anaerobic (A) and oxidized (B) $[AlCp^*]_4$ (AlCp*) in addition to anaerobic (C) and oxidized (D) mixtures with immersion oil (IO). Samples were run under an argon flow of 100 mL/min and were heated at 25 °C/min.*

In both the anaerobic and oxidized mixed samples, the first stage of weight loss corresponds to the exothermic decomposition of the cluster. The presence of the exotherm in the oxidized sample signified that the immersion oil prevented at least some of the $[AlCp^*]_4$ from oxidizing. Once again, due to the sample preparation for this experiment in the glove box, the exact initial cluster to immersion oil ratio is unknown, complicating the ability to quantify the extent of oxidation of the cluster.

*5.4. Conclusion*

T-Jump TOFMS and TGA/DSC experiments performed on pure $[AlCp^*]_4$ and immersion oil coated $[AlCp^*]_4$ were used to evaluate the effectiveness of a coating on the decomposition of the Al cluster. Immersion oil was shown to prevent complete oxidation of the cluster after exposure to air for 1 hour, demonstrated by the exposed material's

release of gas phase aluminum when rapidly heated. Further investigation is needed in order to quantify the effectiveness of these types of coatings on Al clusters, but the preliminary results shown in this study prove that active Al still exists for this system after exposure to air for 1 hour. In future work, oxidizers may be added to the mixture to create a functional energetic composite making use of an air-stabilized Al cluster fuel.

# Chapter 6: High Heating Rate Reaction Dynamics of Al/CuO Nanolaminates by Nanocalorimetry-Coupled Time-of-Flight Mass Spectrometry*

*Summary*

Highly tunable reactive nanolaminates have been of recent interest for various "on chip" energetic applications. The reaction dynamics of Al/CuO nanolaminates were investigated by nanocalorimetry-coupled time-of-flight mass spectrometry, capable of simultaneous measurement of temporal thermal dynamics and detection of evolved gas phase species at heating rates up to ≈ $10^6$ K/s. The nanolaminates were synthesized by alternately sputtering Al and CuO onto the heater of nanocalorimeter sensors. For thin films of 80 nm with one bilayer, the stoichiometric ratio of fuel to oxidizer significantly affected the reaction mechanism: initial reactions occurred between 300 °C and 400 °C, and main reactions varied based on stoichiometry. For thicker films of 199 nm and 266 nm, a series of samples with varying bilayer numbers were analyzed to determine the effect of diffusion distance and interfacial area. Only one reaction step was observed for a sample with a bilayer thickness of 33 nm. A two-step reaction mechanism is observed as the bilayer thickness was increased to 66 nm and beyond: solid-state reaction occurring at the interfaces of Al and CuO before the melting of Al and a much faster liquid-solid reaction right after the melting of Al. At the same time, interfacial premixed distance during the

* The results presented in this chapter have been previously published and are reprinted with permission from: DeLisio, J.B.; Yi, F.; LaVan, D.A.; Zachariah, M.R., High Heating Rate Reaction Dynamics of Al/CuO Nanolaminates by Nanocalorimetry-Coupled Time-of-Flight Mass Spectrometry, *J. Physical Chem. C,* **2017**, 121, 2771. Copyright 2016 American Chemical Society.

deposition was also estimated from parallel experiments. Furthermore, the power data from nanocalorimetry provides a more accurate method, compared to optical emission and mass spectrometry based methods, in determining the ignition temperature in addition to being able to measure actual energy output for films with nanoscale thicknesses.

*6.1. Introduction*

Energetic nanocomposites have been of recent interest for a wide variety of applications due to their high volumetric energy densities, relatively fast reaction kinetics, and decreased ignition temperatures.[1-3] The enhancements gained when using nano-sized components, as opposed to micron-sized particles, are due to increased interfacial area and decreased diffusion length scales. These systems are typically composed of a metal fuel, most commonly aluminum (Al), and a metal oxide oxidizer. Energetic nanocomposites can be manufactured with a wide range of architectures ranging from physical mixtures of nano-sized particles to sputter deposited multilayered nanofoils, often referred to as nanolaminates.[4, 5]

Nanolaminates, in particular, have various uses in microelectromechanical systems (MEMS), microelectronics, and material bonding applications.[6-10] The simple geometry at the fuel/oxidizer interface of multilayered laminates also provides an ideal system to further study the oxygen transport in thermite based reactions, making it possible to probe factors such as the influence of interface-to-volume ratio and its effect on ignition and energy release. These systems can have very low ignition temperatures (below the melting point of Al) and enhanced reactivity based on the number of bilayers.[11, 12]

The reaction dynamics of energetic nanolaminates have been extensively studied at relatively slow heating rates (≈ 10 K/min) using differential scanning calorimetry and

thermogravimetric analysis.[11, 13, 14] A recent study by Egan et al. used high heating rate analytics, which more accurately represent the timescales of a combustion event, to determine the effect of bilayer thickness on the reaction mechanism of Al/CuO nanolaminates.[12] Egan et al. used temperature jump (T-jump) time-of-flight mass spectrometry (ToF-MS) coupled with high speed videography to measure the ignition temperature of 1-12 bilayer nanolaminates with a fixed total thickness.

In this work, the reaction dynamics of the Al/CuO nanolaminate system was further studied by replacing the T-jump ignition system with a chip based nanocalorimeter capable of collecting thermal data while heating at rates of up to ≈ $10^6$ K/s.[15] The integration of nanocalorimetry with ToF-MS allows for simultaneous temporal thermal and speciation measurement.[16] The incorporation of the nanocalorimeter also allows for the study of Al/CuO nanolaminates with significantly thinner bilayers than those previously studied which do not visibly show ignition occurring. We report the effects of stoichiometry, total thickness, and individual bilayer thickness on the reaction mechanism of Al/CuO nanolaminates in addition to providing a more accurate method to determine the ignition temperature of these systems.

*6.2. Experimental*

*6.2.1. Sample Preparation*

The Al/CuO laminates were prepared using sputter deposition techniques. The Al and CuO sputter targets were purchased from Kurt Lesker and the CuO target was indium bound to a copper backing plate for better heat dissipation during the sputtering. A DC power of 300 W is used for aluminum sputtering and a RF power of 300 W is used for CuO sputtering. The sputtering was performed under a pressure of 0.67 Pa of argon. During

deposition, the target not in use was turned off to prevent contamination. XRD analysis (Fig. S1) was performed on a sputter deposited pure CuO film to verify the composition. The nanocalorimeter sensor has a 100 nm thick platinum heater suspended on a 100 nm thick silicon nitride membrane in a silicon frame. The samples are deposited on the silicon nitride side of the nanocalorimeter sensor. As shown in Figure 6.1, 10 nm of alumina was deposited using atomic layer deposition to serve as a barrier layer between the sample and sensor. The first and last layer deposited was aluminum so that one bilayer is defined as two "half" layers of aluminum and one layer of copper oxide as shown in Figure 6.1a. Sample thicknesses, bilayer thickness, and stoichiometry of the laminate were varied to investigate the reaction dynamics of Al/CuO nanolaminates.

*6.2.2. Nanocalorimetry Measurements*

The nanocalorimetry system can measure a thermal signal at heating rates up to $10^6$ K/s. The calibration of the nanocalorimeter sensors used in this work has been previously described in detail.[17] Briefly, the resistance and temperature were recorded by electrical measurements and an optical pyrometer during the resistive heating/cooling. In order to calculate enthalpy, a previously published method[18] was used that entailed heating each empty nanocalorimeter sensor at various heating rates to determine the heat losses and heat capacity of the bare sensor. The power associated with the sample could then be calculated from the total power by subtracting the power associated with the bare sensor and the heat losses. Optical emission from the chip during heating was also recorded using a high speed camera (Phantom v12.0, 67,000 frames per second), but that data is not part of the nanocalorimeter measurement.

*6.2.3. Time-of-Flight Mass Spectrometer System*

A previously reported technique describes the integration of the nanocalorimeter into a time-of-flight mass spectrometer (ToF-MS).[16] Figure 6.1b shows a diagram of the integrated setup with high speed videography to record optical emission from reaction. Specific details of the linear ToF-MS system used for this study have been previously reported.[19, 20] The nanocalorimeter sensor was inserted into the ionization region of the ToF-MS using a linear motion feedthrough with a 3D printed adapter and sensor cover. A sampling rate of 100 µs per spectrum (10 kHz) was used to capture the progress of the reaction with 100 spectra obtained post-triggering for each run. Gas phase reaction products were ionized for 3 µs using an electron gun operated at 70 eV and 1 mA. The data was captured and processed using a 600 MHz digital oscilloscope.

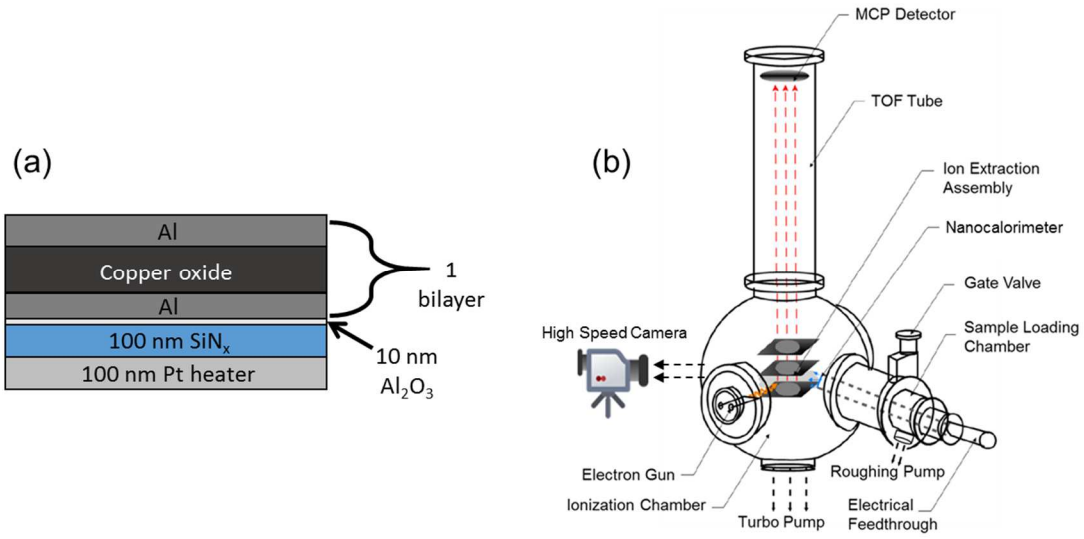


***Figure 6.18.*** *Diagram of sputter deposited single bilayer Al/CuO nanolaminate (a) and ToF-MS experimental setup with integrated nanocalorimeter and high speed imaging (b).*

*6.3. Results*

*6.3.1. Effect of Stoichiometry on Al/CuO Reaction*

In order to first evaluate the effect of stoichiometry on the reaction mechanism, films of varying equivalence ratios ($\phi$) were rapidly heated on the nanocalorimeter within the ionization region of the ToF-MS. Figure 6.2 shows the nanocalorimetry results from rapid heating ($\approx 10^5$ K/s) of the respective Al/CuO nanolaminates. These samples each have only one bilayer. The ratio of Al:CuO was varied and the total thickness was kept constant at 80 nm. All 3 samples show an initial exothermic peak with an onset temperature between 300 °C and 400 °C. The thermal data was much clearer for the fuel rich sample with the predominant exotherm occurring at the melting point of Al. The third exothermic reaction occurred around the decomposition temperature of CuO. This sample was run a second time (Figure 6.S2) and a sharp endotherm was detected corresponding to the Al-Cu eutectic. As the equivalence ratio reduced to 1, the stoichiometric ratio, the main reaction exotherm was shifted to a higher temperature closer to the decomposition of CuO. This may be related the diffusivity of liquid aluminum. The main exothermic peak becomes much broader in the fuel lean sample and spans from the melting point of Al to the decomposition temperature of CuO. An endothermic reaction is observed that occurs after the Al/CuO reaction and corresponds to the decomposition of $Cu_2O$ to Cu and $O_2$. At these temperatures, the generated $O_2$ can react with the $SiN_x$ on the chip to produce $SiO_2$ and $N_2$, which will be addressed in more detail in a parallel paper.

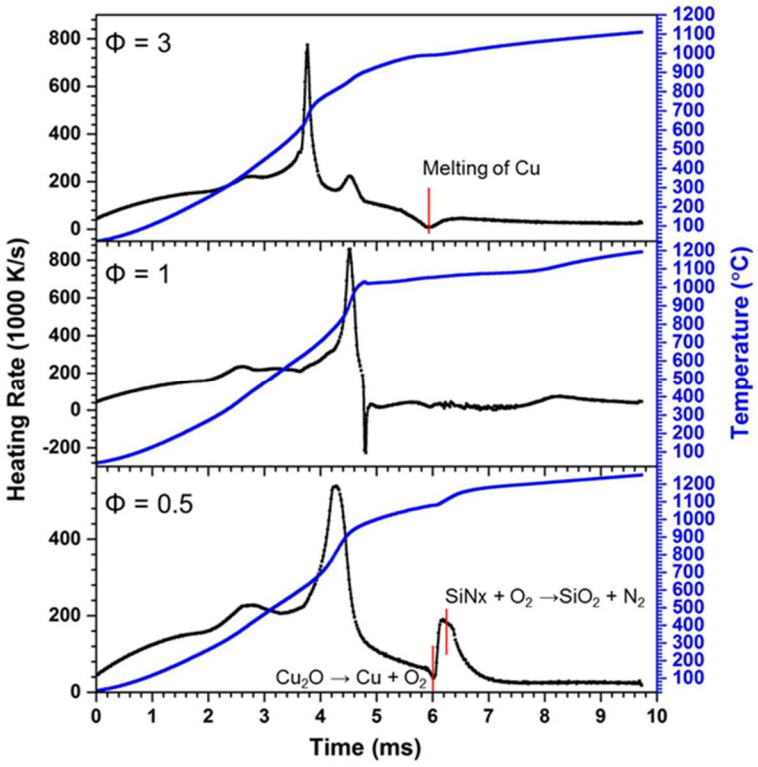


***Figure 6.19.*** *Heating Rate and Temperature vs Time plots for 80 nm thick, 1 bilayer Al/CuO nanolaminates with equivalence ratios (ϕ) of 0.5, 1, and 3.*

*6.3.2. Effect of Total Sample Thickness and Bilayer Number*

The aforementioned samples with total thicknesses of 80 nm did not produce sufficient gas phase reaction products for detection in the ToF-MS. In addition, previous work done investigating particulate based Al/CuO nanothermites using the T-jump ToF-MS system demonstrated that fuel rich samples showed increased signal intensities for Al containing reaction intermediates in the MS.[20] A series of thicker, fuel rich samples (ϕ = 1.5) were tested with total thicknesses of 199 nm and 266 nm with varying bilayer number and thickness as seen in Table 6.1. For each of the samples listed in Table 6.1, two nanocalorimeter chips were prepared to ensure repeatability of the results.

***Table 6.3.*** *Sample thickness, bilayer number, and bilayer thickness for each of the studied Al/CuO nanolaminate samples.*

| Sample ID | Sample Thickness | Bilayer Number | Bilayer Thickness |
|---|---|---|---|
| A | 199 nm | 6 | 33 nm |
| B | 199 nm | 3 | 66 nm |
| C | 266 nm | 4 | 66 nm |
| D | 266 nm | 2 | 133 nm |

Optical emission for each of these samples varied depending on the total thickness and number of bilayers. All samples besides sample A showed visible signs of ignition (Figure 6.S3) in the captured high speed video. We propose that for these nanolaminates, there is a threshold for visible ignition to occur which is determined by the amount of active material in the system. Samples A and B have the same total thickness, yet sample A has double the number of bilayers resulting in a lower active material content possibly due to the presence of more premixed regions. This will be discussed in detail below.

Figure 6.3 shows the time resolved Al and AlO release, temperature, and power results for the 199 nm total thickness Al/CuO nanolaminates.

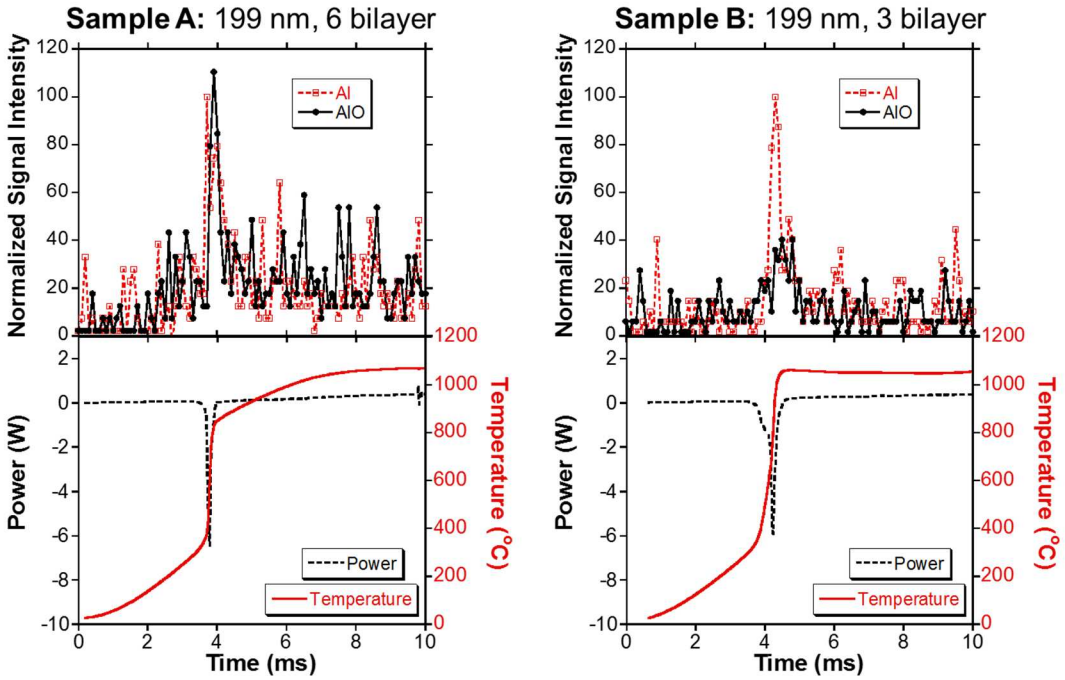


***Figure 6.20.*** *Time resolved MS and nanocalorimeter results for samples A and B.*

The MS results are normalized to the maximum Al signal intensity. Previous T-jump ToF-MS experiments have shown the detection of Al in the MS at ≈ 1450 °C during rapid heating of Al nanoparticles.[20] For the Al/CuO nanolaminates, Al is detected at a much lower temperature due to the rapid reaction between Al and CuO. For samples A and B, the Al signal peak intensity occurs at the same point as the maximum power shown in the nanocalorimetry data.

The ratio of AlO to Al signal intensity is much larger in the 6 bilayer system (Fig. 3A) in comparison to the 3 bilayer system (Fig. 3B). The absolute signal intensity for the Al and AlO peak in the 6 bilayer system was 83 % and 149 % of that for the 3 bilayer system further demonstrating the decrease in Al and increase in AlO when more bilayers are present. In addition, the peak with for the AlO signal over time is much sharper in the 6 bilayer system. As a control experiment, fully reacted films and pure $Al_2O_3$ runs were

performed and no Al or AlO species were detected supporting the claim that these species are released during the reaction of the nanolaminate. We propose that the increased interfacial area in the 6 bilayer sample results in a faster bulk reaction rate, as seen by the higher maximum power. The increased interfacial area also results in a lower relative Al signal intensity due to the formation of more AlO. The 6 bilayer sample has more interfacial area for Al to react as gas phase Al is generated.

Figure 6.4 shows the ToF-MS and nanocalorimeter results for nanolaminates with a total thickness of 266 nm.

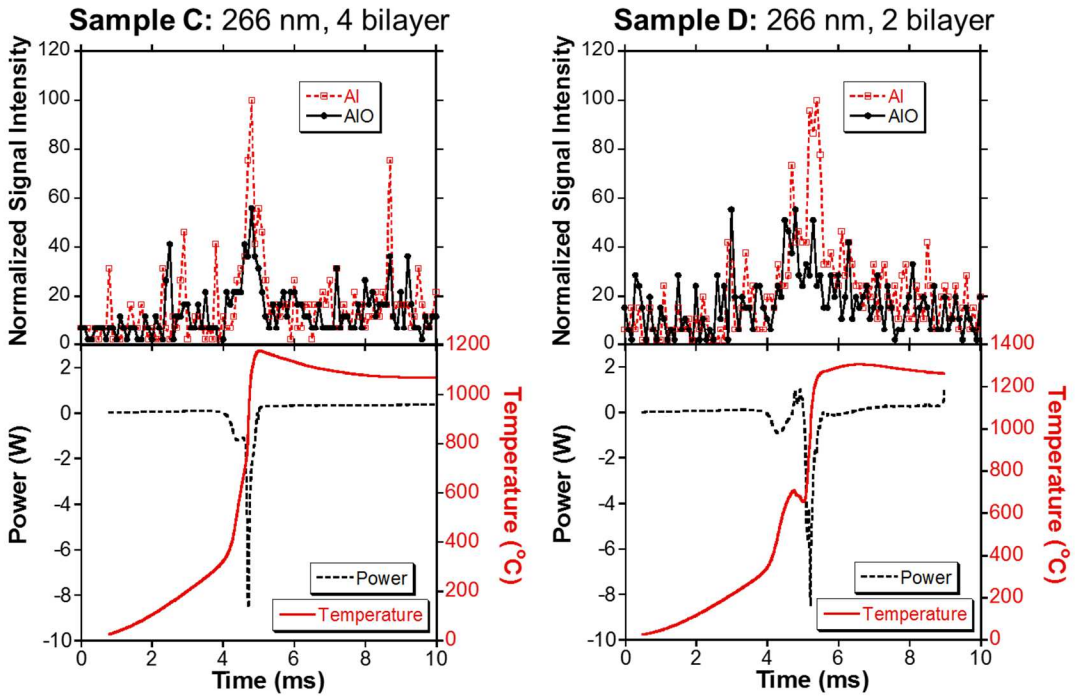


***Figure 6.21.*** *Time resolved MS and nanocalorimeter results for samples C and D.*

The 2 bilayer, 266 nm total thickness sample (D) had the largest individual bilayer thickness of the samples examined in this study. This sample also showed a sharp endothermic peak associated with the melting of excess aluminum at ≈ 4.5 ms. The time resolved MS data shows a delay in peak Al signal intensity in comparison to the peak AlO

signal for the 2 bilayer system. This occurs because the 2 bilayer sample has more "bulk" aluminum which slows down the heating rate at the melting point of Al as shown by the sharp endotherm at ≈ 4.5 ms in Figure 6.4D. The Al located in the center of each individual Al layer must first melt before it can diffuse outward to come in contact with a reactive interface. Once the Al is mobile, the heating rate sharply increases, in turn, resulting in an increase in the Al signal intensity in the MS. The AlO signal intensity is not tied directly to the heating rate as this species will continue to be generated at the reaction interface, even during the endothermic "bulk" Al melting event at ≈ 4.5 ms in Figure 6.4D. It is also important to note that there is no gas phase $O_2$ generation visible in the MS for all 4 samples. This implies a purely condensed phase oxygen transport mechanism occurring before the decomposition temperature of CuO.

*6.3.3. Enthalpy of Reaction*

Figures 6.3 and 6.4 show the resultant power curves for samples A-D along with their respective temporal temperatures. Reaction enthalpies for each sample were calculated by integrating the power during the time of reaction. Because the samples are fuel rich, the experimental enthalpies were normalized with respect to the limiting reagent (CuO) and are listed in Table 6.2 below:

***Table 6.4.*** *Experimental enthalpy of reactions from integrated power vs. time curves for each sample and calculated interface thickness and absolute enthalpy of reaction.*

| Sample ID | Sample Thickness | Bilayer Number | Bilayer Thickness | $\Delta H_{exp}$ (kJ/mol CuO) | Premixed Interface Thickness | Efficiency Factor η |
|---|---|---|---|---|---|---|
| A | 199 nm | 6 | 33 nm | -50.3 ± 1.0 | 9.3 ± 0.1 nm | 0.31 ± 0.01 |
| B | 199 nm | 3 | 66 nm | -82.4 ± 2.1 | | |
| C | 266 nm | 4 | 66 nm | -80.3 ± 0.3 | | |
| D | 266 nm | 2 | 133 nm | -105.7 ± 14 | | |

Sample A had the lowest experimental enthalpy because this sample has the most bilayers, and in turn, the most pre-mixed regions. Samples B and C had approximately the same individual bilayer thickness and also relatively similar experimental enthalpies. Sample D contained the most active material resulting in the largest measured reaction enthalpy. Thus while more bilayers result in faster energy release, this occurs with a loss of energy density.

One source for potential error in our experimental energy calculation is active Al is being lost during rapid heating, as detected by the gas phase Al signal in the MS. The amount of gas phase Al could potentially be much greater in the scope of our experiment when compared to traditional DSC experiments due to the much higher heating rates employed. Additionally, in order to calculate the amount of CuO in each film, a uniform thickness was assumed. One source of error in regards to the normalization of results is the film not having a uniform thickness.

### *6.4. Discussion*

#### *6.4.1. Pre-Mixed Interfaces*

Increasing the number of bilayers was shown to decrease the energy output from the Al/CuO nanolaminates in this study. The following equation was used to calculate the interface thickness ($T_i$) and reaction efficiency factor, $\eta$, from the theoretical reaction enthalpy ($\Delta H_{theo}$) without premixed interfaces using the results from parallel experiments with the same total thickness ($T_t$), but different number of bilayers as shown in Table 6.2 above:

$$\Delta H_{theo} \eta \frac{(T_t - 2bT_i)}{T_t} = \Delta H_{exp}$$

where the experimental reaction enthalpy ($\Delta H_{exp}$) is equal to $\Delta H_{theo}$ multiplied by the efficiency factor, $\eta$, and the fraction of active material in the laminate. The fraction of active material in the laminate is defined as the thickness of active material divided by the total thickness. The thickness of active material is determined by the total thickness subtracted by two times the number of bilayers ($b$) times the interface thickness ($T_i$). For these calculations, the interface is assumed to be fully reacted and therefore does not add energy to the reaction when heated. The $\Delta H_{theo}$ for this system is ≈ -370 kJ/mol CuO. Assuming each laminate has the same $T_i$ and $\eta$, respective values of 9.3 nm and 0.31 were calculated. An $\eta$ of 0.31 results means the experimentally determined energy value ≈ 69 % less than the theoretical energy, but our calculations do not take into account the energy required to melt excess Al. As shown above, the MS detects AlO formation during reaction. It is possible that the laminate may be reacting to form a mixture of $Al_2O_3$ and AlO, which would result in a lower enthalpy of reaction.

Kwon et al. also examined the interface layers of Al/CuO nanolaminates and found the premixed interfacial region to be inhomogeneous with an irregular thickness of up to 5 nm.[14] This value corresponds to a single Al/CuO interface. The calculated premixed interface thickness in Table 6.2 is almost double this value. The premixed interface thickness was dependent on the deposition temperature. Kwon et al. used a chilled substrate set at 10 °C.[14] For our deposition, the substrate started out at room temperature with sputter deposition causing a slight temperature increase. To deposit Al/CuO onto the nanocalorimeter sensors, good thermal contact between the sensor and sensor holder must be made, otherwise, you would have fully mixed/reacted film with no exothermic signal observed when heated. Poor thermal contact between the sensor and the holder will result

in elevated sensor temperatures as the holder acts as a heat sink during deposition. Therefore, the slight temperature increase is most likely the cause for the comparatively larger interface thickness due to the substrate in our study not being chilled.

*6.4.2. Two-Stage Reaction Mechanism*

Further investigation of the high heating rate temperature vs time data collected from the nanocalorimeter shows a two-stage reaction mechanism for the samples listed in Table 6.1 with the exception of sample A (6 bilayer, 199 nm total thickness). Linear fits for each reaction regime shown in the temperature vs time plots were used to determine corresponding average energy release rates as seen in Figure 6.5. Direct heating of the nanocalorimeter by the applied current pulse was approximated to be linear and was deducted from the linear fits during reaction in order to determine the average energy release rates.

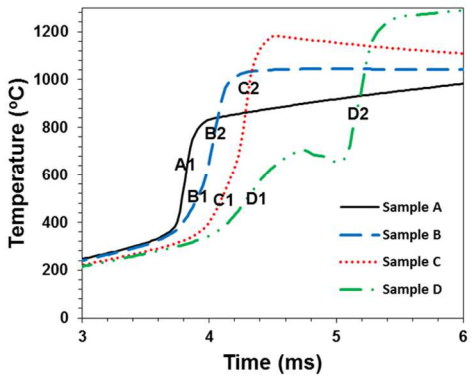


| | | | Stage 1 | Stage 2 |
|---|---|---|---|---|
| **Sample ID** | **Sample Thickness** | **Bilayer Thickness** | **Avg. Energy Release Rate** | **Avg. Energy Release Rate** |
| A | 199 nm | 33 nm | 3320 K/ms | - |
| B | 199 nm | 66 nm | 860 K/ms | 2620 K/ms |
| C | 266 nm | 66 nm | 1030 K/ms | 3630 K/ms |
| D | 266 nm | 133 nm | 610 K/ms | 2480 K/ms |

***Figure 6.5.*** *Temperature vs time curves for each Al/CuO nanolaminate (samples A-D as listed in table 6.1) with labeled reaction stages and corresponding average energy release rates.*

For samples B, C, and D, the transition point occurs near the melting point of bulk Al. The first stage of reaction is proposed to be a purely solid-state reaction occurring at the interfaces of Al and CuO. Once the sample is heated to the Al melting point, diffusion rates

rapidly increase and gas phase species are then detected by the ToF-MS. Increasing the number of bilayers results in a leftward shift in the second stage of reaction. The second stage of reaction happens earlier due to the increased heat generation caused by the increased interfacial area in the samples with more bilayers. Sample A contains the largest interfacial area and only shows a single reaction step. Due to the large interfacial area and shorter diffusion distance, the solid phase reaction is much faster with an average energy release rate of 3320 K/ms. Furthermore, no endothermic signal was observed from nanocalorimeter data as the temperature reached the melting point of aluminum. Due to the short diffusion distance, the fuel diffusion rate and the fuel supply is sufficient to complete the reaction. As the bilayer thickness/diffusion distance increases, the diffusivities of Al or CuO significantly affect the reaction speed, which is reflected in the observed lower average energy release rate of the first exothermic event for samples with individual bilayer thicknesses greater than 33 nm. A transition in the heating rate occurs around the melting temperature of aluminum for these samples. The Al diffusion rate would be much higher compared to CuO because, after the melting of Al, we did not observe any transition of heating rate, even around the decomposition of CuO in thickest samples. In addition, by comparing this series of experiments, one may be able to calculate the diffusivities in this thermite system from the heating rate and thickness of the individual layer.

### *6.4.3. Defining Ignition*

Egan et al. have developed a model based on 1D diffusion for nanolaminate ignition that holds true for the samples studied above.[12] The samples studied by Egan et al. were approximately an order of magnitude larger in total thickness than the 199 nm - 266 nm thick samples in Table 6.1. Table 6.3 shows measured ignition temperatures using 3

different experimental methods. The ignition temperature using the optical method is defined as the temperature in which a sharp rise in optical emission taken from high speed video is first observed. The ignition temperature reported in the mass spec method is the onset temperature of detected $H_2$. The appearance of $H_2$ marks the start of reaction between Al and any $H_2O$ trapped between the layers of the laminate. This species was used to determine the ignition temperature for the MS method because $H_2$ has a much higher relative signal intensity than other reaction products detected in the MS. A low relative signal intensity of a product species may result in an overestimate in the onset temperature of said species. The power method for determining the ignition temperature is defined as the onset point of the first exothermic peak after removing the power contribution applied to initially heat the nanocalorimeter sensor.

***Table 6.5.*** *Ignition temperatures for each sample using high speed video, mass spectrometry, and power data collected through nanocalorimetry.*

| Sample ID | Sample Thickness | Bilayer Number | Bilayer Thickness | Ignition Temperature | | |
|---|---|---|---|---|---|---|
| | | | | Optical Method | Mass Spec. Method | Power Method |
| A | 199 nm | 6 | 33 nm | --- | 591 °C | 318 °C |
| B | 199 nm | 3 | 66 nm | 667 °C | 676 °C | 319 °C |
| C | 266 nm | 4 | 66 nm | 609 °C | 661 °C | 322 °C |
| D | 266 nm | 2 | 133 nm | 697 °C | 668 °C | 329 °C |

In the model reported by Egan et al., the total thickness was 1000 nm and the 12 bilayer sample corresponded to the lowest ignition temperature of ≈ 350 °C. The experimental ignition temperatures determined by Egan et al. employed the optical method, which was accurate for their system due to the much larger total thickness of their nanolaminates (1800 nm vs 199 – 266 nm). Their 12 bilayer system corresponds to an

approximate bilayer thickness of 150 nm. For our results, sample D in Table 6.3 has a bilayer thickness of 133 nm and an ignition temperature of ≈ 330 °C, measured using the power method. This value agrees nicely with the aforementioned 1D diffusion model for nanolaminate ignition.[12] Figure 6.6 shows the experimentally determined ignition temperatures and iterative ignition model of Egan *et al*. along with the ignition temperatures measured from our samples as determined by the power method for the Al/CuO nanolaminates listed in Table 6.3.

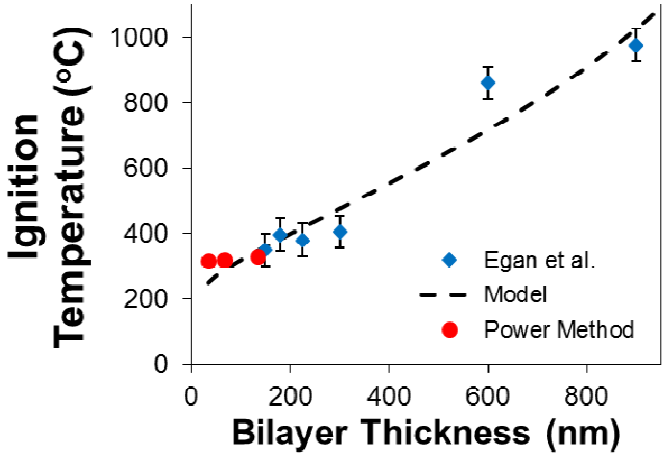


***Figure 6.6.*** *Plot of ignition temperature vs bilayer thickness for experimental values and model by Egan et al. and experimentally calculated values using the power method for Al/CuO nanolaminates in this study.*

The power method gives much lower ignition temperatures than both optical and MS methods. The optical method is limited by the sensitivity of the camera and sample size. The heat capacity of the chip is not negligible when the total thickness of the nanolaminate is small resulting in little to no optical emission at the start of reaction. In addition, the MS only detects gas phase products, which may not be released at the earliest stages of ignition. The nanocalorimeter shows an exotherm occurring before any AlO is detected implying that the start of reaction occurs through a condensed phase diffusion

based mechanism between the Al and CuO layers. When analyzing the very thin film, as shown in Figure 6.2, multiple reaction steps are apparent. For the thicker films, there is no heating rate decrease after the initial onset of the exothermic event due to the self-propagation of the reaction. The power method is the only technique, in comparison to mass spec and optical methods, in which the onset temperature of this initial exotherm can be reliably measured. We propose that the power method is the most accurate method in studying ignition of energetic nanolaminate systems, especially when dealing with small samples and small bilayer thicknesses.

*6.5. Conclusion*

By integrating high heating rate chip based calorimetry with ToF-MS, a solid-state initiation was observed for Al/CuO nanolaminates. Samples with an individual bilayer thickness of 33 nm showed a single step reaction mechanism, occurring primarily in the condensed phase, due to this sample showing the highest AlO:Al ratio in the MS. These films demonstrated the highest maximum power output, but lowest overall energy release. The decreased energy release is attributed to the loss of active material in the premixed regions of the interface. The premixed interface thickness was calculated to be 9.3 nm with an efficiency factor of 0.31.

The ignition temperature was measured using optical, MS, and nanocalorimeter based methods and the values compared. Measuring the ignition temperature from the power data collected from the nanocalorimeter proved to be the most accurate method for samples with total thicknesses on the order of a hundreds of nanometers. The values measured for the samples in this study showed good agreement with previous Al/CuO nanolaminate ignition models based on their individual bilayer thicknesses.[12]

# Chapter 7: Electrospray Synthesis of Novel Energetic Nanocomposite Microstructures*

*Summary*

In order to probe the effect of architecture on the chemistry and energy release of energetic nanocomposites, new techniques with high control of synthesized microstructure are needed. This chapter presents one such synthesis method that employs electrospray as a means of creating both gelled microparticle and thin film architectures. Additives were also incorporated into these microstructures targeting biocidal applications. The following electrospray synthesized microparticle systems using a nitrocellulose (NC) binder will be presented: gelled nanoaluminum (nAl), nAl/RDX, and iodine-containing nAl/CuO. In addition, the electrospray synthesis of nAl/polyvinylidene fluoride (PVDF) and nAl/PVDF/bismuth iodate ($Bi(IO_3)_3$) thin films is presented.

## *7.1. Introduction*

Many energetic composites use a binder to give the system mechanical integrity. It is also desirable for the binder to enhance the energetic properties of the fuel. Typical energetic binders used in the past have been nitrocellulose, epoxies, and various fluropolymers.[1-3] When dealing with nanocomposite materials, achieving a high mass loading of nanosized components can be a challenge due to the rapid increase in viscosity of the polymer melt upon the addition of nanomaterials.[2] In addition, the architecture of the composite has shown to greatly affect the bulk reactivity of the material, as described in Chapter 1.[4, 5] In this chapter, I will present a compilation of work done using

* The results in this chapter have been previously published in references [10-13]. My role in these publications was to assist in electrospray optimization and preform T-Jump ignition and T-Jump/TOFMS analysis of the materials.

electrospray based deposition methods to create tunable microstructures used to study the effects of architecture on energy release in energetic nanocomposites.

One of the earliest and most popular applications of electrospray is as an ionization source for mass spectrometry.[6] Electrospray utilizes electrical forces for liquid atomization. A conductive precursor solution is typically passed through a positively charged needle forming a Taylor cone from which liquid is ejected.[7] A collection substrate or extractor is either grounded or negatively charged typically creating an electric field on the order of 2-4 kV/cm. The Taylor cone is formed when the electric field exerts a similar amount of force as the surface tension of the conductive precursor solution. A jet of liquid is emitted from the Taylor cone that turns into an aerosol plume of nominally monodisperse droplets as small as tens of nanometers due to columbic repulsion.

Our group had previously employed an electrospinning technique in the creation of nanofiber-based thermite textiles.[8] Electrospinning operates using the same principles as electrospray, but instead of creating small droplets, nanofibers are ejected from the Taylor cone due to higher binder content (~50 wt. %) in the precursor solution.[9] The previously constructed electrospinning setup was used with various precursor solutions enabling electrospray based deposition. Binder composition and concentration, particle loading, and needle to substrate distance were tuned create energetic nanocomposites in microparticle and thin film architectures. Various additives were also incorporated into these microstructures targeting biocidal applications. This chapter will focus on the following electrospray synthesized microparticle systems using a nitrocellulose (NC) binder: gelled nanoaluminum (nAl)[10], nAl/RDX, and iodine-containing nAl/CuO[11]. In addition, the

electrospray synthesis of nAl/polyvinylidene fluoride (PVDF)[12] and nAl/PVDF/bismuth iodate ($Bi(IO_3)_3$)[13] thin films is presented.

## *7.2. Experimental*

### *7.2.1. Materials*

nAl was purchased from either Argonide or Novacentrix as noted in the specific references corresponding to each microparticle/thin film system. Both brands of nAl showed the same performance and microstructure in each system. Copper oxide (CuO) nanoparticles (<50nm) and iodine ($I_2$) were purchased from Sigma-Aldrich. The nitrocellulose (NC) used in this work was also purchased from Sigma-Aldrich as 4-8 wt. % Collodion solution. The RDX used in this study was RS-RDX from Eurenco, and was dissolved in DMF at a loading of 95 mg/mL to create a stock solution for precursor preparation.

For the thin film precursors, PVDF (Mw ¼ 534.000) and dimethyl formamide (DMF) (99.8 wt. %) purchased from Sigma–Aldrich were used as received. Bismuth iodate nanopowders were synthesized from 460 mg $Bi(NO_3)_3 \cdot 5H_2O$ dissolved into 10 mL DI water, to which 7.8 mol $L^{-1}$ $HNO_3$ was added. The solution was stirred approximate 10 min until it became clear. 500 mg $HIO_3$ was dissolved into 20 mL DI water. The $HIO_3$ solution was then added to the $Bi(NO_3)_3$ solution under vigorous stirring. As the $HIO_3$ solution was added, a white precipitate immediately formed which was subsequently collected by vacuum filtration. The product was washed four times using DI water, dried in the fume hood for 12 h, and then grounded into a fine powder.

### *7.2.2. Precursor Preparation*

Microparticle precursor solutions were prepared by sonicating solid particulates and dissolved NC in a 3:1 mixture of ethanol/diethyl ether for 1 hour. In the case of the Al/RDX/NC system, the RDX stock solution (95 mg/mL RDX in DMF) was added to the precursor prior to sonication. The solution was then stirred for 24 hours before electrospray processing. The thin film precursors were prepared by first dissolving PVDF at a concentration of 50 mg/mL in DMF by stirring for 2 hours. Solid particulates were then added and the solution was sonicated for 1 hour prior to 24 hours of stirring.

### *7.2.3. Electrospray Setup*

Figure 7.1 depicts the home-built electrospray setup used for the creation of both microparticles and thin films.

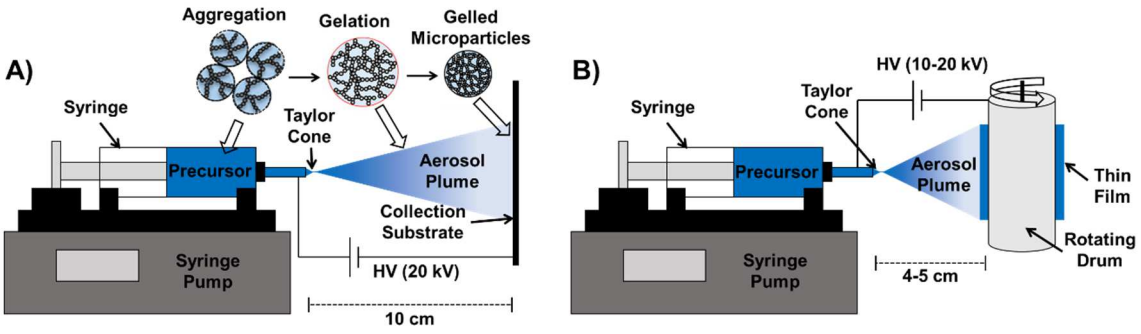


***Figure 7.22.*** *Home-built electrospray synthesis setups for the creation of microparticles (A) and thin films (B).*

For the creation of microparticles, a needle to substrate distance of 10 cm was used to allow for sufficient droplet drying time as shown in Figure 7.1A. For thin film creation, a wet deposition is performed by reducing the needle to substrate distance to 4-5 cm as shown in Figure 7.1B. The voltage applied for thin film creation was adjusted between 10 and 20 kV. Different voltages were required to maintain a stable Taylor cone depending on the conductivity of the precursor solution. A rotating drum was used as the collection substrate

for thin film creation to aid in the creation of a homogeneous film. For both microparticle and thin film architectures, flow rates of 0.1-4 mL/hr were used depending on the specific precursor.

### *7.2.4. Characterization*

The surface morphologies and thickness of films were characterized using a scanning electron microscope (SEM, Hitachi, SU-70 FEG-SEM) equipped with energy dispersive x-ray spectroscopy (EDS). For cross-sectional images, samples were first fractured in liquid nitrogen and then sputtered with carbon. T-Jump ignition experiments were performed using high-speed video taken with a Phantom v12.0 digital camera running Phantom 692 software. The videos were recorded at 67000 frames per second. Ignition time and temperature were then determined from the recordings and T-Jump data. To investigate biocidal species release from additives, T-Jump TOFMS was performed. Both T-Jump ignition and T-Jump TOFMS are described, in detail, in Chapter 2.

The combustion properties of the films were also captured using high-speed videography with a frame rate of 7,000 frames per second in both air and argon environments. Typically, a 3 x 0.5 $cm^2$ film was fixed between a nichrome wire igniter and a holder in an atmosphere-controlled combustion chamber. The combustion of films were conducted under an argon or air atmosphere, and evaluated in triplicate for each sample condition to determine propagation velocity. Following combustion, the condensed residue was collected for XRD evaluation.

## *7.3. Results and Discussion*

### *7.3.1. Microparticles*

Electrospray synthesis methods were used to create various "gelled microparticles" held together with a small mass fraction of the energetic binder, NC. The first electrospray synthesized microparticle system was composed of nAl and NC.[10] The morphology of these particles is depicted in the SEM images shown in Figure 7.2.

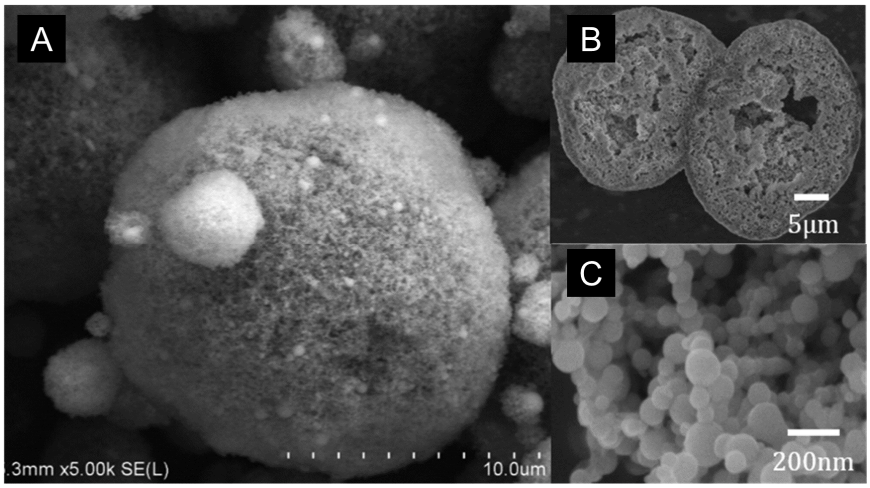


***Figure 7.23.*** *SEM images of (a) a typical gelled microsphere, (b) cross section, and (c) high magnification SEM image of gelled microsphere.[10]*

The created particles are porous in nature and contain voids in their interior as shown in the cross section image in Figure 7.2B. While some of these cavities exist, the particle is predominantly well bound together with the NC binder that extends throughout the particle. Brunauer-Emmett-Teller (BET) measurements done on these particles state that they have a surface area of 20 $m^2/g$, which is fairly close to an individual nAl aggregate.

The microparticle diameter can be tuned by changing the mass loading of nAl in the precursor solution as shown in Figure 7.3. The particle diameter ranges from 2 to 16 µm with nAl concentrations of 50 to 160 mg/mL. The drastic change at higher mass loadings may be due to changes in viscosity of the precursor solution as NC concentration

is a function of nAl concentration as it is based off of the weight percent of particulates in the precursor. An NC concentration of 10 wt. % was used for each of the created particles.

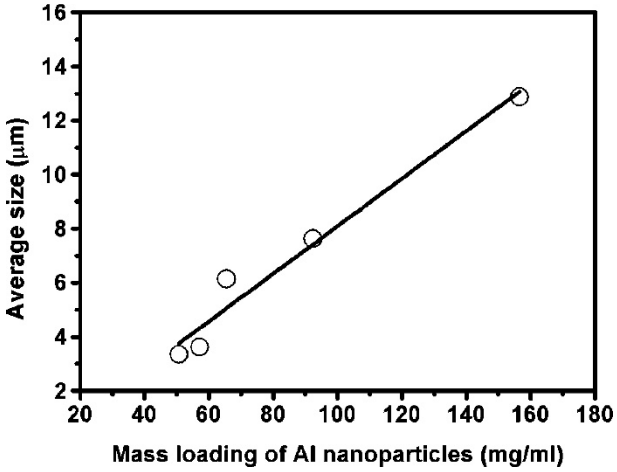


***Figure 7.24.*** *Average gelled particle size as a function of nAl mass loading in the precursor solution.[10]*

T-Jump ignition experiments, as described in Chapter 2, were performed in air to evaluate the combustion performance of the gelled nAl microspheres. Figure 7.4 shows high speed images from these experiments for gelled nAl microspheres with 10 wt. % NC and pure nAl particles.

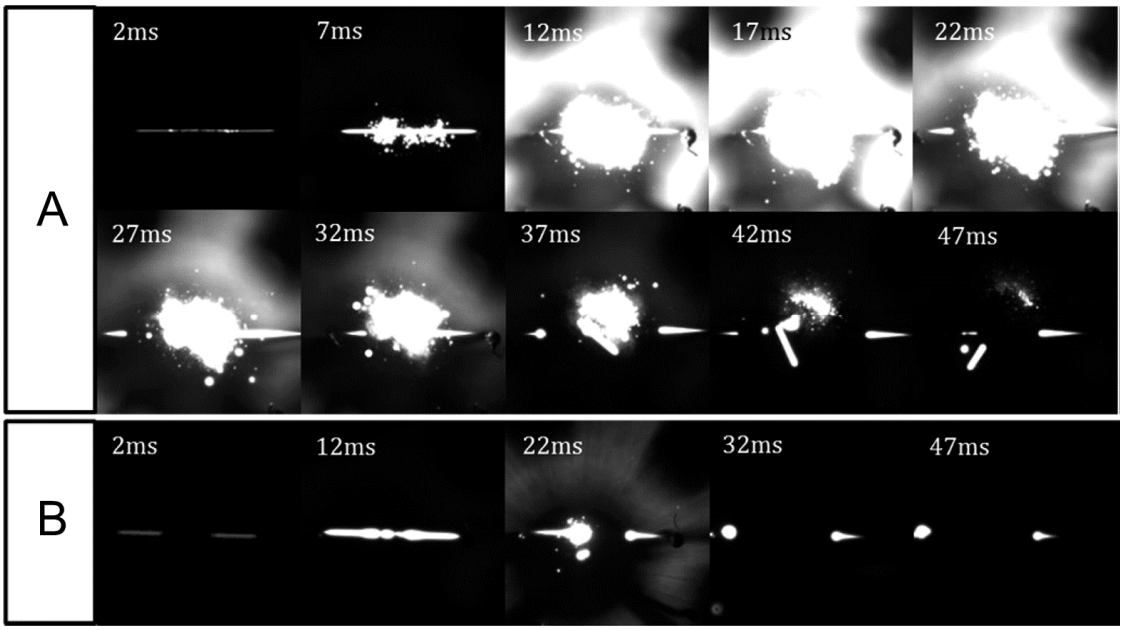


***Figure 7.25.*** *High speed video images of Gelled nAl microparticles (A) and nAl (B). The labeled times are time elapsed after triggering.[10]*

Enhanced reactivity attributing to this microstructure is clearly observed by the enhanced optical emission in Figure 7.4A in comparison to 7.4B. It is proposed that the NC binder in the microparticle prevents the rapid sintering of the nAl during ignition thus preventing the loss of surface area that would slow down oxidation. The ignition delay times are also drastically reduced as neat nAl has an ignition delay of 14.1 ms while the gelled microparticles have a delay of only 0.3 ms. These particles have recently been employed as additives in hydrocarbon fuels to achieve enhanced burn rates and have also been used in composite solid rocket propellants that showed decreased particle agglomeration on the propellant surface.[14, 15]

In a collaborative project with the Naval Surface Warfare Center in Indian Head, MD, similar gelled microparticles were synthesized incorporating the high explosive, RDX. SEM images of the synthesized RDX particles, each containing 5 wt. % NC, are shown in Figure 7.5.

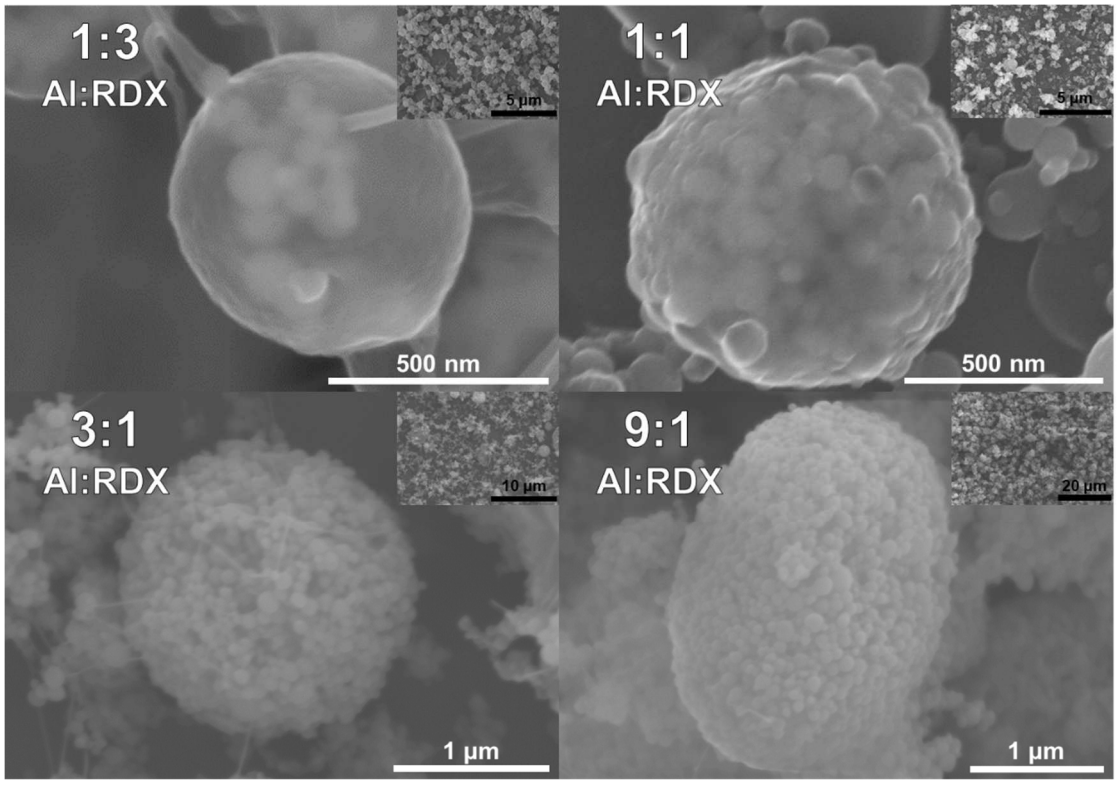


***Figure 7.26.*** *Scanning Electron Microscope Images of Al/RDX/NC Nanostructured Microparticles.*

The particles with the highest RDX loading show the Al fully encased in a RDX/NC matrix. As the RDX loading in the precursor was decreased, the average particle diameter increased from ~500 nm to ~2 µm. The particles also became less spherical at the highest Al loading. XRD analysis was also performed in order to verify that crystalline RDX exists within the microparticle as shown in Figure 7.6. Characterization of the energetic performance of these particles is currently ongoing and will be detailed in the future work section of Chapter 10.

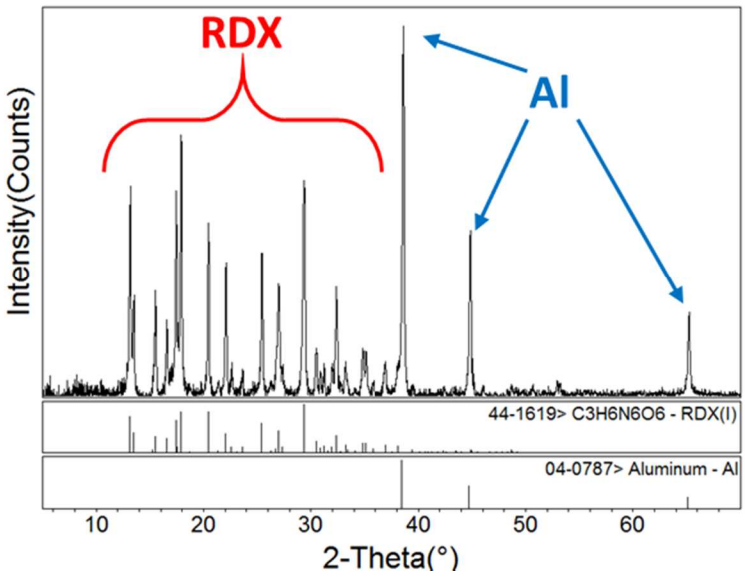


***Figure 7.27.*** *XRD of 1:3 (Al:RDX) microparticles showing crystalline RDX and Al within the particle.*

*7.3.2. Thin Films*

Electrospray deposition was also employed to create free standing nAl/PVDF energetic thin films using the setup depicted in Figure 7.1B. One of the primary goals of this study was to demonstrate that nanoparticles could be incorporated within a polymer matrix at high loadings (50 wt%) to form a free-standing film as a prelude to forming a 3D structure. Figure 7.7 shows SEM images of nAl/PVDF thin films with 50 wt. % nAl mass loading.

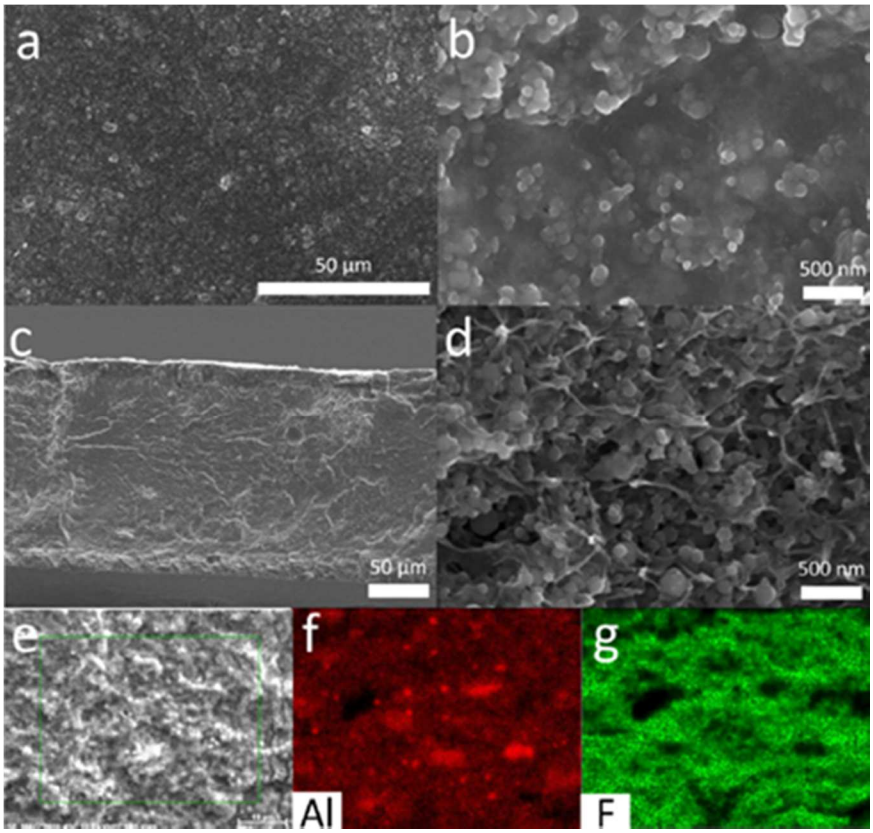


***Figure 7.28.*** *SEM images of films deposited by electrospray with 50 wt% Al-NPs loading and adding AP. (a) Top-view of the film's surface; (b) close-up of the top-view; (c) cross-section of film; (d) close-up of cross section. Elemental mapping analysis of cross-section of film with 50 wt% Al-NPs loading (e–g).[12]*

Figures 7.7a and 7.7b show the surface morphology of the synthesized thin films while 7.7c and 7.7d are cross-sectional images of the film. The electrospray synthesis method produced a crack free film with a uniform thickness (about 170 µm) composed of what appears to be a fibrous polymer network. The nAl is visibly well disbursed throughout the film, which is confirmed in the EDS results shown in Figure 7.7e-f. nAl mass loadings of 65 wt. % resulted in the formation of large aggregated microparticles due to there being an insufficient amount of binder to form a film.

The combustion propagation velocity of the nAl/PVDF film was measured by igniting a 4 cm by 1 cm piece of the film. For each sample, three experiments were run to

calculate the average combustion propagation velocity. Films were ignited in both air and argon environments. Figure 7.8 shows a representative flame propagation schematic of the nAl/PVDF film. Figure 7.8b–d shows high speed images during film combustion with different nAl loadings in air and argon environments. All the films were easily ignited and demonstrated self-sustaining combustion.

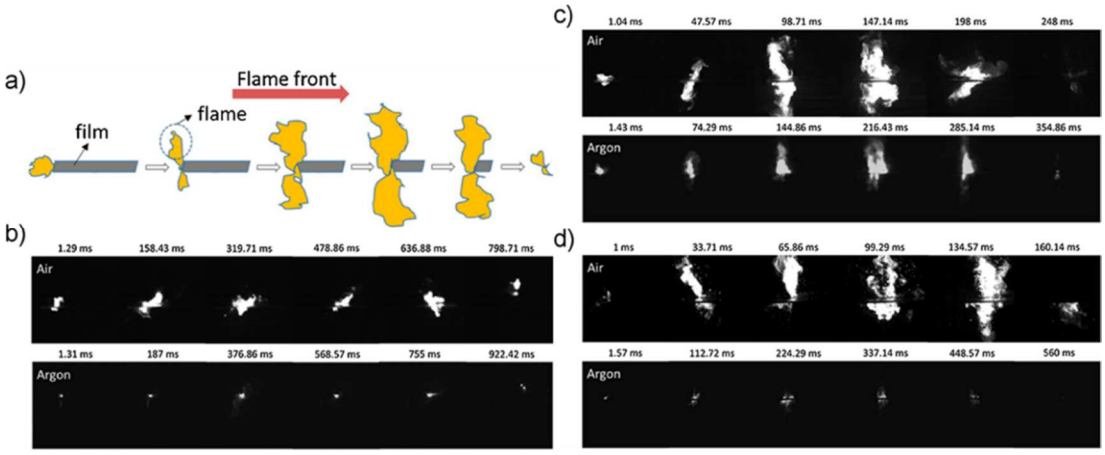


***Figure 7.29.*** *(a) Schematic showing flame propagation. (b–d) Selected frames of nAl/PVDF film combustion using high speed videography with 16.7, 30, and 50 wt. % nAl mass loadings, respectively. Note: The time stamps on the top of each picture indicate elapsed time from the starting trigger.[12]*

Figure 7.9 shows the average combustion propagation velocities of nAl/PVDF films in air and argon, respectively. For films burning in argon, the flame propagation velocity is significantly lower than burning in air at the same nAl mass loading, except for the lowest particle mass loading film (16.7 wt. %), which has almost the same burn speed in both experimental conditions. The combustion of moderate particle loading film (30 wt. % nAl) had the highest burn speed (11 cm/s). This mass loading of nAl corresponds to the stoichiometric mixture. In comparison, when burning in air, the highest velocity (23 cm/s) appeared at the highest particle loading (50 wt. %) nAl/PVDF film.

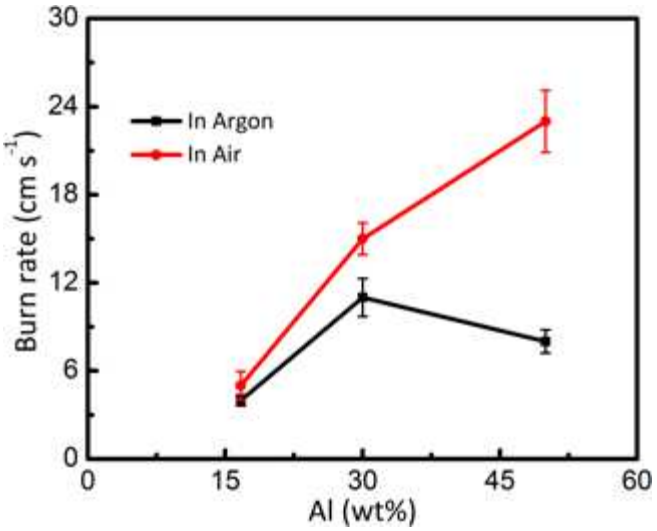


***Figure 7.30.*** *Combustion propagation velocity of Al/PVDF films as a function of particle mass loading in air and argon.[12]*

Chapter 8 takes a deeper look into the reaction mechanism of these films.

*7.3.3. Additives for Biocidal Applications*

The increased threat of bioterrorism has led to an immediate need for energetic materials with high neutralization efficiencies of biological warfare agents.[16-18] The highest neutralization efficiencies are achieved by coupling high temperatures with a long-lasting release of a biocidal agent such as iodine. One method of achieving this goal is to incorporate elemental iodine or iodine containing oxysalts into energetic nanocomposites. In order to enhance both reactivity and biocidal agent release, electrospray synthesis methods can be employed as described above. In this section, examples of both gelled microparticles and thin films tailored for use in biocidal applications are described. My role in these projects was to assist in the synthesis of the composites in addition to analyzing the gas phase products released during combustion using T-Jump TOFMS as described in Chapter 2.

The first energetic nanocomposite created for biocidal applications employed the electrosprayed microparticle architecture composed of Al/CuO nanothermite and

elemental iodine. Microparticles with molecular iodine contents ranging from 5 wt. % to 50 wt. % were created. Electrospray synthesized Al/CuO nanothermite microparticles have preciously demonstrated 3 times higher maximum pressures and pressurization rates than their physically mixed counterparts.[19] This microstructure aids in the intermixing between the fuel and oxidizer in addition to limiting sintering during reaction resulting in enhanced energy release rates.

SEM images of the elemental iodine contain Al/CuO microparticles at two different total particle loadings are shown in Figure 7.10.

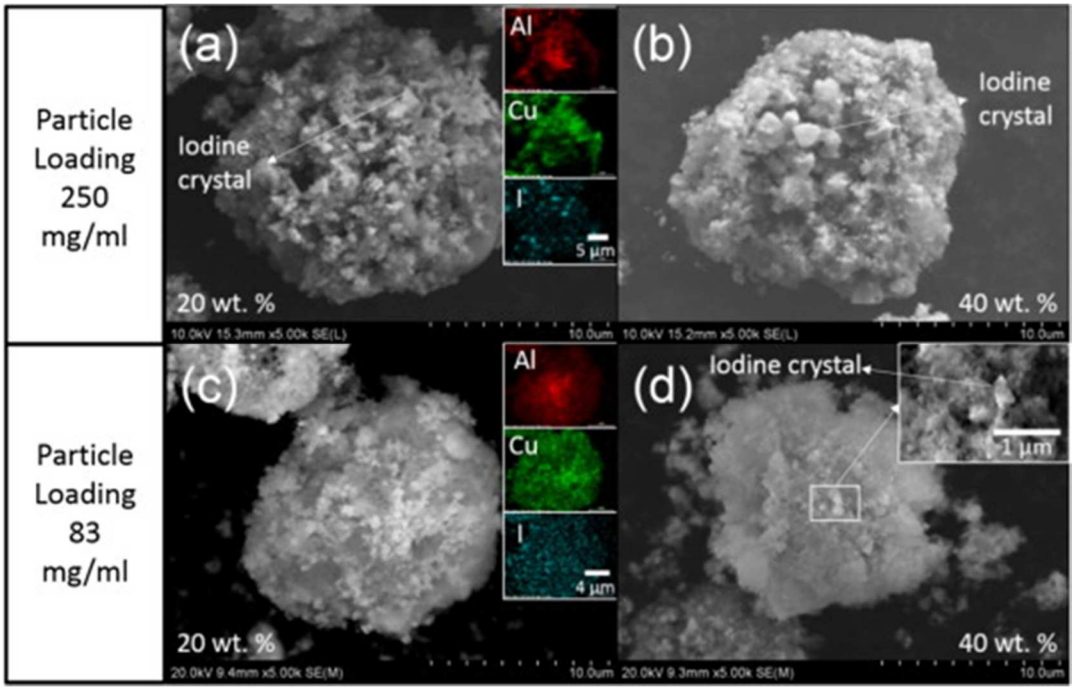


***Figure 7.31.*** *SEM images of iodine-containing Al/CuO nanocomposites. Iodine content: 20 wt.%, (a, c), 40 wt.% (b, d). Note: a and b are microparticles from precursors with particle loading of 250 mg/ml; (c) and (d) are from precursors with particle loading of 83 mg/ml. The inserts in (a) and (c) are EDS elemental maps.[11]*

Small iodine crystals are observed in the SEM images, but these crystals do not appear to disrupt the integrity of the microparticle. They are homogenously mixed throughout the particle as shown in the EDS maps in figure 7.10a and 7.10c.

T-Jump TOFMS was performed to analyze the gas phase reaction products during rapid heating using two different sample deposition methods as shown in Figure 7.8.

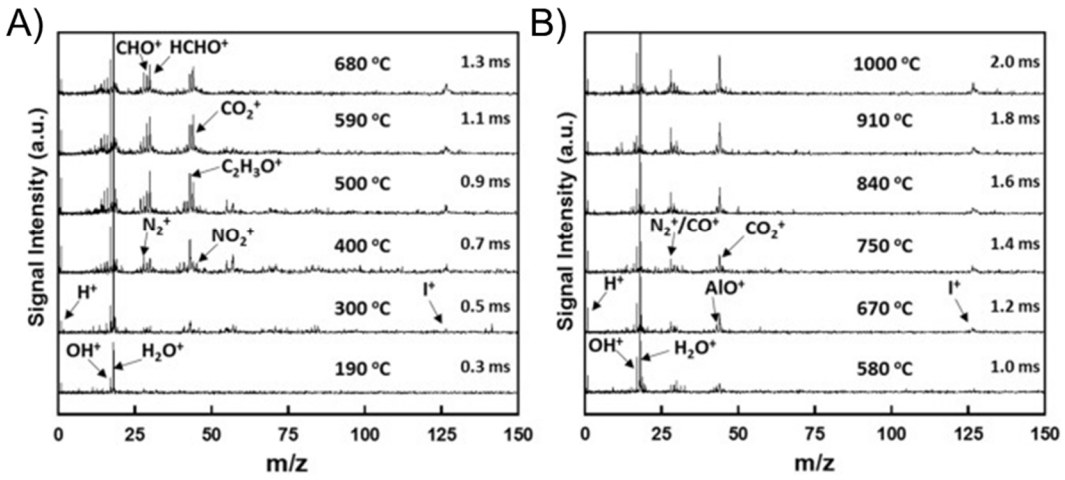


***Figure 7.32.*** *T-Jump mass spectrum of iodine containing Al/CuO (50 wt. % iodine) composites on rapidly heated wire (5 x 10₅ K/s) for (a) samples directly electrosprayed onto the wire and (b) sampled suspended in hexane and then deposited onto the wire. Note: the labeled is the time and corresponding temperature after triggering.[11]*

Figure 7.11a shows the time resolved mass spectra with corresponding wire temperatures for the case where the sample was directly electrosprayed onto the Pt wire used for ignition. In Figure 7.11b, the microparticles were dispersed in hexane, dissolving any elemental iodine crystals in the structure, and then deposited onto the Pt wire. Iodine appears much earlier (300 $^{o}$C) in the experiment where the particles were directly electrosprayed onto the wire (Fig. 7.11a). This initial iodine release corresponds to the sublimation of the iodine crystals within the microparticles. This could be occurring at a slightly higher temperature than the boiling point of iodine due to the high heating rates (5 x $10^5$ K/s) used and the iodine potentially being trapped in the NC matrix, which decomposes at 170 $^{o}$C. NC decomposition products are apparent in the mass spectra starting at 300 $^{o}$C, the same temperature at which iodine is first detected. The late appearance of iodine in the time resolved mass spectra for the sample washed in hexane alludes to a second stage of iodine

release in these samples. This iodine release occurs at 670 $^{o}$C, which is close to the measured ignition temperature of the microparticles in air. AlO is also detected at this time validating that oxidation of aluminum is occurring concurrently with the release of iodine. It is proposed that during the sample preparation process, some percentage of iodine dopes the alumina ($Al_2O_3$) shell of the Al NPs. In these iodine containing Al/CuO composites, iodine is likely stabilized by the $Al_2O_3$ shell of the aluminum nanoparticles and is not released until the shell is disrupted by the melting of the aluminum core. This halogen/$Al_2O_3$ interaction is studied, in detail, in Chapter 8 in regards to the interactions between fluorine and $Al_2O_3$.

In a second study, a multifunctional reactive material ($Bi(IO_3)_3$/nAl thermite) was developed with biocidal combustion products that remain active for an extended period of time, well past the thermal and pressure pulse for bioagents. As opposed to the elemental iodine containing microparticles above, $Bi(IO_3)_3$/nAl/PVDF thin films employed a synthesized metal iodate, $Bi(IO_3)_3$, as a iodine source in addition to acting as a secondary oxidizer. T-jump/TOFMS results demonstrate that $Bi(IO_3)_3$ containing films are highly energetic and release elemental iodine, suggesting that $Bi(IO_3)_3$/Al/PVDF films are a prime candidate as a biocidal energetic. SEM images showing a cross section of the synthesized film are shown in Figure 7.12A. For the T-Jump TOFMS measurements, $Bi(IO_3)_3$/nAl/PVDF films were directly deposited on the Pt-wire by our electrospray method. Upon ignition, $H_2^+$, $Bi^+$, and $I_2^+$are observed. The iodine and oxygen release over time are shown in Figure 7.12B. The ignition temperature of $Bi(IO_3)_3$/nAl/PVDF films in vacuum, argon and air are 850, 530, and 520 °C, respectively, with the combustion in argon and air much more vigorous than that in vacuum.

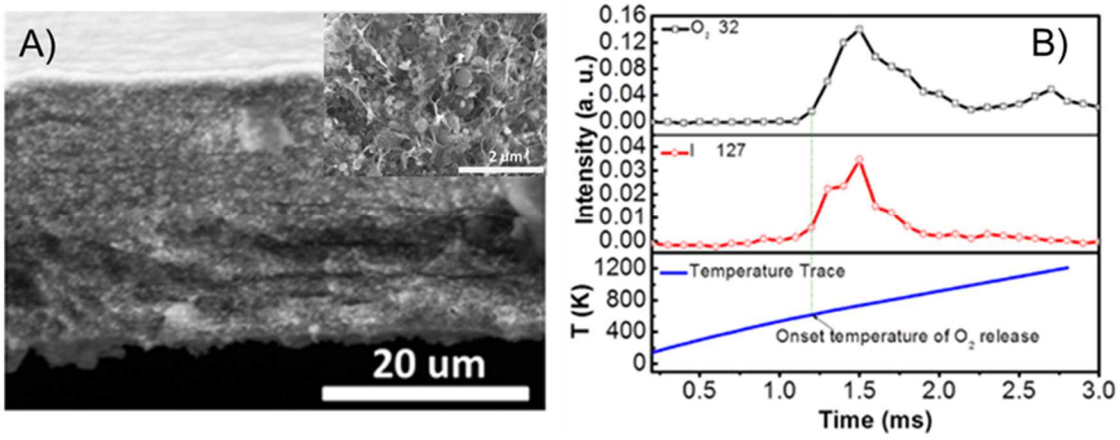


***Figure 7.33.*** *SEM image of a Bi(IO3)3/nAl/PVDF thin film (A) and T-Jump TOFMS results showing iodine release.*

## *7.4. Conclusion*

In this chapter, a novel approach to creating two unique microstructures, gelled microparticles and thin films, was described. Both of these architectures were created using electrospray synthesis methods. Examples of both microstructures and characterization of their energetic performance was presented. The rest of this dissertation will focus on probing the reaction mechanism of nAl/PVDF thin films described in this chapter.

# Chapter 8: Probing the Reaction Mechanism of Aluminum/Polyvinylidene Fluoride Composites*

*Summary*

Energetic thin films with high mass loadings of nanosized components have been recently fabricated using electrospray deposition. These films are composed of aluminum nanoparticles (nAl) homogeneously dispersed in an energetic fluoropolymer binder, polyvinylidene fluoride (PVDF). The nascent oxide shell of the nAl has been previously shown to undergo a pre-ignition reaction (PIR) with fluoropolymers such as polytetrafluoroethylene (PTFE). This work examines the PIR between alumina and PVDF to further explain the reaction mechanism of the Al/PVDF system. Temperature jump (T-jump) ignition experiments in air, argon, and vacuum environments showed that the nAl is fluorinated by gas phase species due to a decrease in reactivity in vacuum. Thermogravimetric analysis coupled with differential scanning calorimetry (TGA/DSC) was used to confirm the occurrence of a PIR and gas phase products during the PIR and fluorination of nAl were investigated with temperature jump time of flight mass spectrometry (T-jump TOFMS). Results show a direct correlation between the amount of alumina in the PVDF film and the relative signal intensity of hydrogen fluoride release (HF). Although the PIR between alumina and PVDF plays an important role in the Al/PVDF reaction mechanism, burn speeds of Al/PVDF films containing additional pure alumina particles showed no burn speed enhancement.

* The results presented in this chapter have been previously published and are reprinted with permission from: DeLisio, J.B.; Hu, X.; Wu, T.; Egan, G.C.; Young, G.; Zachariah, M.R., Probing the Reaction Mechanism of Aluminum/Poly(vinylidene fluoride) Composites, *J. Physical Chem. B,* **2016**, 120, 5534. 

*8.1. Introduction*

Aluminum particles have been extensively employed as a fuel in solid rocket propellants due to aluminum's desirable combustion characteristics.[1] Nanosized aluminum (nAl) particles are now readily available and have been implemented into various energetic formulations.[2] The primary motivation for nanosized components is decreased diffusion lengths, and an increase in the mass specific burning rate. In typical propellant applications, a binder must be employed to give the propellant mechanical integrity and ideally to enhance the combustion properties of the system.[3,4] Fluoropolymer binders are one type of energetic binder, which favorably reacts with the aluminum fuel to create aluminum fluoride ($AlF_3$).

Polytetrafluoroethylene (PTFE), also known as Teflon, has been extensively used for the fluorination of aluminum in energetic formulations due to the high density of fluorine atoms within the polymer.[5,6] The Al/PTFE reaction mechanism has previously been studied, and a pre-ignition reaction (PIR) has been observed that is proposed to play an important role in the reaction mechanism between Al and a fluoropolymer.[7] The PIR is proposed to arise from the fluorination of the native $Al_2O_3$ passivation shell on aluminum particles.[8] With most aluminum nanopowders being between ~70-80% active, there is a significant weight percent of alumina in these composites that can contribute to this reaction. As nAl particle size decreases, the amount of $Al_2O_3$ in the particle on a per mass basis is increased resulting to an enhanced PIR leading to increased ignition sensitivity and exothermicity.[7]

Although PTFE has one of the highest fluorine concentrations among the commonly used fluoropolymers, it poses many processing issues because PTFE is

insoluble in most solvents. However, polyvinylidene fluoride (PVDF) does not have these solubility issues and has recently been employed as an energetic binder for nAl[9] using an additive manufacturing approach. In this approach, electrospray deposition was employed to avoid the difficulties in mixing nanoparticles in polymer systems, and thus enabling the fabrication of high metal loaded polymer. [9-10] This approach also enables the fabrication of graded or laminate structures with different mechanical and combustion performance. These properties make Al/PVDF highly desirable for a wide range of potential applications, but composites involving nAl have not yet been widely studied and more information is needed on the fluorination mechanism.

Of particular interest is the PIR that has been observed in the Al/PTFE system as well as multiple other systems employing halogen-containing oxidizers such as the Al/perfluoropolyether (PFPE) and Al/$I_2O_5$ systems.[11-12] Preliminary work by our group has proposed that a similar PIR occurs in the Al/PVDF system as well.[9] However, the exact role or importance of the PIR in the combustion Al/PVDF has not yet been fully explored. Here, we will investigate this process in the context of the broader mechanisms of reaction and propagation. In particular we focus on using techniques that allow for exploring a wide range of heating rates, including those that are representative of free combustion.

Previous works have used standard differential scanning calorimetry (DSC) and thermogravimetric analysis (TGA) techniques to investigate the Al/PTFE PIR and a direct correlation between exothermicity of the PIR and heating rate has been observed.[13] However, the highest heating rate tested in that work was 780 $^{o}$C/min. In comparison, the temperature jump (T-jump) ignition experiments can increase the heating rate of the

material to ~$10^5$ ºC/sec, which can more realistically represent a combustion event.[14] Ignition experiments using the T-jump technique were performed in different environments and pressures to probe the effect of the surrounding gasses on the overall Al/PVDF reaction mechanism. Since little information on the species created before and during ignition has been obtained, we employ T-jump ignition coupled to time-of-flight mass spectrometry (TOFMS), to investigate the role of the PIR in the overall reaction mechanism at much shorter timescales.

In this work, the PIR between $Al_2O_3$ and PVDF is explored to determine its role in the reaction mechanism between nAl and PVDF. PIRs have been studied in other halogen-containing systems, but have yet to be fully investigated in the Al/PVDF system.[7, 8, 11, 12, 15] We examine the exact nature of how nAl is fluorinated in an energetic thin film employing PVDF as an energetic binder. Further understanding of this mechanism may allow for the creation of tailored energetic laminates and multicomponent nanocomposites. Gas phase decomposition products of fluoropoymers exhibiting PIRs with $Al_2O_3$ have yet to be analyzed on timescales representative of combustion, which will be the main focus of this work. Results show that nAl is fluorinated by gas phase decomposition products from the PVDF and the nature of the PVDF decomposition is directly correlated to the amount of $Al_2O_3$ in the film. These new findings are then used to determine if altering the decomposition of PVDF by adding $Al_2O_3$ can affect the burn speed of thin films.

*8.2. Experimental*

*8.2.1. Materials*

The nAl used in this work were purchased from Novacentrix with an active Al content of 81 % by mass, determined by thermogravimetric analysis (TGA). The $Al_2O_3$

nanopowder (<50 nm), polyvinylidene fluoride (PVDF) (MW = 534,000), and dimethylformamide (DMF) (99.8 wt. %) were purchased from Sigma-Aldrich.

*8.2.2. Precursor Preparation and Film Deposition*

Al/PVDF thin films were created using the previously described electrospray based deposition method.[9] This method allows for the creation of films with high mass loadings while avoiding the increased viscosity issues associated with traditional nanopowder-containing polymer melts. Al/PVDF films of 50% Al by weight were synthesized for the initial T-jump ignition tests. Al/PVDF equivalence ratios of 0.5, 1, and 2 were synthesized for T-jump TOFMS experiments probing the release of gas phase species, which correspond to Al mass loadings of 15, 25, and 40 % by weight. The equivalence ratio in this work corresponds to the Al to F ratio to give the main reaction product, $AlF_3$. $Al_2O_3$/PVDF films were also made with the same $Al_2O_3$:PVDF mass loadings as the Al/PVDF films in order to further probe the PIR. Films prepared for burn speed tests used a stoichiometric ratio of Al:PVDF (25 % Al by weight) with varying amounts of 50 nm $Al_2O_3$ added to the precursor solution before sonication/stirring. Precursor solutions for the films prepared for burn speed tests used 8 mL of DMF with a 50 mg/mL loading of PVDF in addition to the varying amounts of Al and $Al_2O_3$. A distance of 4 cm and voltage differential of 18 kV between the electrospray needle and the collection substrate were employed as the parameters for electrospray deposition. The electrospray setup was also modified to coat a thin platinum (Pt) wire (76 μm diameter), approximately 10 mm in length with a 3-5 mm length of coating, to be used for the T-jump experiments. When depositing films onto the Pt wire, a deposition time of 15 min at a rate of 2 mL/h was used

resulting in a ~5 μm thick film on the wire. Free standing film thicknesses ranged from 50-100 μm.

*8.2.3. Characterization*

Ignition temperature tests were performed using T-jump heating of a platinum wire (76 μm diameter) coated with an electrosprayed Al/PVDF film approximately 3-5 mm in length inside of a chamber pressurized to a specified value. The Callendar-Van Dusen equation was used to correlate the resistance of the wire to a time resolved temperature by recording the voltage across, and current through the wire during heating, with a 600 MHz digital oscilloscope.[14] The platinum wire was heated with a heating rate of approximately 5 x $10^5$ K/s in these experiments for approximately 3 ms. High-speed video was taken using a Phantom v12.0 digital camera running Phantom 692 software. The videos were recorded at 67000 frames per second. Ignition time and temperature were then determined from the recordings and T-jump data.

Thermogravimetric (TG) and Differential Scanning Calorimetry (DSC) experiments were performed on a SDT Q600 (TA instruments) under 100 mL/min of $O_2$ flow. 1-2 mg samples were placed into an alumina pan, and heated from room temperature up to 1000 ℃ at a rate of 5 ℃/min to 50 ℃/min. No discernable difference in TGA/DSC results were observed between stock PVDF powders and electrosprayed PVDF films.

Temperature jump time of flight mass spectrometry (T-jump TOFMS) was performed using a previously described home-built instrument.[14] Samples were electrosprayed onto a 76 μm diameter platinum wire for use in the TOFMS and for ignition temperature tests respectively. The same heating parameters and wire temperature calculations were performed as in the T-jump ignition experiments described above. A

sampling rate of 100 μs per spectrum (10 kHz) was used to capture the progress of the reaction with 100 spectra obtained post-triggering for each run. The data was captured using a 600 MHz digital oscilloscope.

PVDF films and $Al_2O_3$/PVDF films (before and after heating) were analyzed using X-ray diffraction (XRD; Bruker C2 Discover with GADDS, operating at 40 kV and 40 mA with unfiltered Cu Ka radiation, E ¼ 8049 eV, k ¼ 1.5406 Å).

Burn speed tests were performed in accordance to the parameters previously described in similar work on energetic thin films.[9, 10] Strips of each film (0.5 cm x 3.0 cm x ~0.01 cm) were ignited using a resistively heated nichrome wire in a small chamber purged with argon for 15 min. High speed video was taken of the flame propagation, using a Phantom Miro M110 recording at 7000 fps with an exposure of 40 μs, in order to calculate a burn speed for each film.

### *8.3. Results and Discussion*

#### *8.3.1. T-jump Ignition*

In order to evaluate the reactivity of the Al/PVDF films, precursor solutions were directly electrosprayed onto platinum T-jump filaments using the electrospray deposition setup shown in Figure 8.1A.

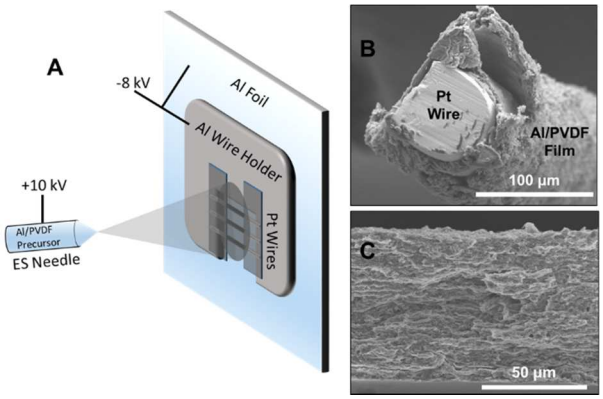


***Figure 8.34.*** *Pt wire electrospray deposition setup (A), cross-section of coated Pt wire (B) and cross section of 20 wt. % Al/PVDF free standing film (C).*

A 50% Al/PVDF by mass ratio was found to be the highest nAl loading that enabled a crack free, mechanically flexible film, therefore this ratio was used for preliminary T-jump ignition tests.[9] T-jump ignition experiments were run in air, argon and vacuum environments, and show a decrease in reactivity between air and argon and negligible reactivity in vacuum (Fig. 8.S1). The increased reactivity of samples ignited in air can be attributed to the participation of $O_{2(g)}$ in the oxidation of the Al as well as production of oxygenated carbon. The significant decrease in reactivity at low pressures suggests that gas phase reaction products must also be participating in the overall reaction. Zulfiqar et al., has reported that the main decomposition product of PVDF is hydrogen fluoride (HF).[16] These results suggest that the Al/PVDF reaction is a two-step process where the PVDF must first decompose into HF, which then enables the fluorination of the Al. The exact composition of these gas phase decomposition species at time scales relevant to reaction will be further analyzed using other techniques later in this paper.

In order to further explore how Al is being oxidized by a gas phase product from the decomposition of PVDF, T-jump experiments were performed to measure the ignition temperature ($T_{ign}$) in air and argon at pressures of 0.1 MPa to ~9 MPa. Figure 8.2 shows a

decrease in ignition temperature of over 250 C as the pressure is increased, consistent with Al reaction with a gaseous reaction product that has constrained diffusion at higher pressures. The higher ignition temperature at 1 atm of argon, when compared to 1 atm of air, implies that reaction is initiated by gas phase oxygen at this pressure, while at elevated pressures, there is no discernable difference in ignition temperature between argon and oxygen environments, suggesting that ignition is initiated by the PVDF decomposition products at these pressures.

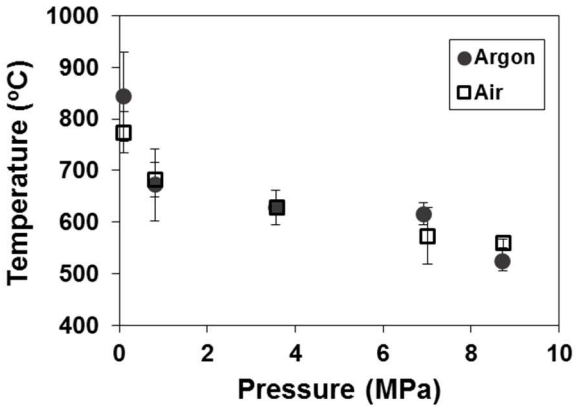


***Figure 8.35.*** *Ignition temperature vs pressure for Al/PVDF film electrosprayed onto a platinum wire in air and argon.*

*8.3.2. Slow Heating Chemistry by TGA/DSC*

As mentioned above, slow heating rate TGA/DSC in argon environments has been frequently used to investigate the reaction mechanism between aluminum and fluoropolymers.[9] Previous TGA results at 20 °C/min shown by our group indicate that pure PVDF films lose the majority of their mass, corresponding to decomposition, at 500 °C while Al/PVDF films show the majority of their mass loss ~100 °C lower at a temperature of 400 °C.[9] Previous work by Pantoya et al. has shown that the alumina shell of nano to micron sized aluminum particles can react with fluoropolymers, such as PTFE and PFPE, before ignition in what is referred to as the pre-ignition reaction (PIR).[8, 15]

In previous work, we state that the first mass loss seen (between 190 and 300 ºC) in the TGA of Al/PVDF films corresponds to the PIR between the $Al_2O_3$ shell of the nAl and the PVDF. Figure 8.S2 highlights the initial mass loss and PIR seen in TGA/DSC results for an $Al_2O_3$/PVDF film heated under 100 mL/min of argon flow.

In this work, a slightly different approach was taken to tweeze out the effect of $Al_2O_3$ on the decomposition of PVDF as compared to prior work.[7, 9, 13] When standard DSC experiments are run in argon, the PIR exotherm in $Al_2O_3$/fluoropolymer systems can potentially be hidden by the large PVDF decomposition endotherm immediately following the PIR. In addition, the fluorine containing decomposition products can react with the alumina pan used in the TGA/DSC complicating the results (Fig. 8.S3). In order to further investigate the $Al_2O_3$/PVDF PIR and its effect on PVDF decomposition, TGA/DSC of pure PVDF and $Al_2O_3$/PVDF films (40 wt. % $Al_2O_3$) were run under 100 mL/min of pure $O_2$.. Further, since Hobosyan et al. demonstrated that heating rate plays an important role in the exothermicity of the PIR.[13], we employed 5, 20, and 50 ºC/min heating ramps. It is important to note that the combustion of PVDF in $O_2$ will be an exothermic process with an onset temperature close to the decomposition temperature of PVDF under the respective heating conditions.

Figure 8.3 shows TGA and DSC results for the of reaction of PVDF and $Al_2O_3$/PVDF films with oxygen at heating rates of 5, 20, and 50 ºC/min. Figure 8.3A shows two stages of mass loss when the PVDF film is heated in $O_2$ with onset temperatures increasing with an increase in heating rate. Two exotherms, due to the oxidation of PVDF decomposition products, are observed in Figure 8.3C that correspond to these mass loss

events with the distinction between the two peaks becoming less apparent with an increase in heating rate.

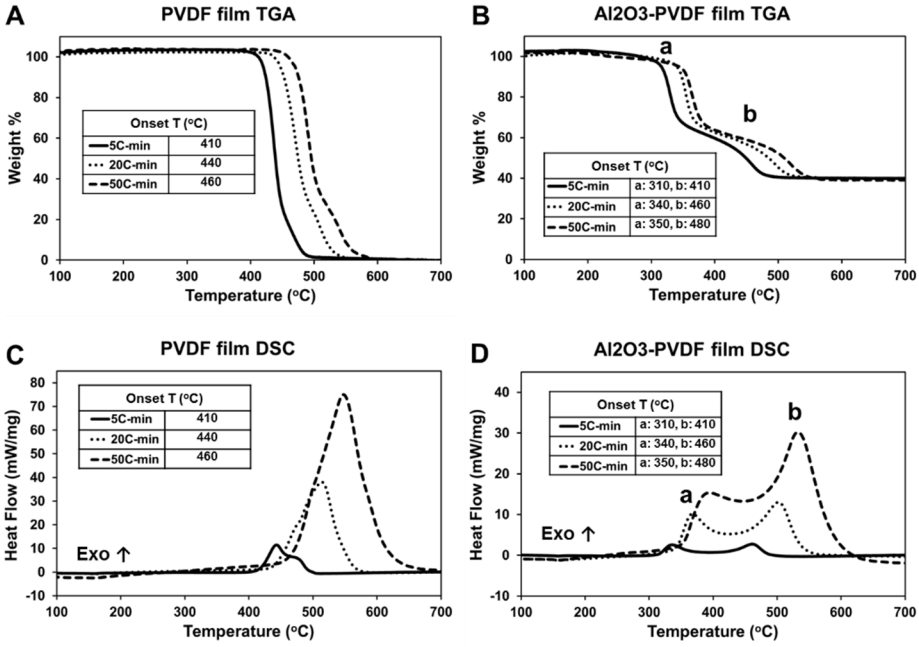


***Figure 8.36.*** *TGA/DSC data with labeled respective peak onset temperatures at heating rates of 5, 20, and 50 °C/min under 100 mL/min $O_2$ flow of PVDF and $Al_2O_3$/PVDF films containing 40 wt. % $Al_2O_3$.*

When compared to previous PVDF decomposition analysis by our group in argon at 20 °C/min, the 20 °C/min run in $O_2$ has a similar onset temperature of ~440 °C.[9] It can be inferred from this comparison that the PVDF decomposes at the same temperature with and without the presence of $O_2$. Previous work also showed a final wt. %, when heated in argon, of ~20-25 wt. % that corresponds to remaining carbon from PVDF.[9] PVDF is composed of 37.5 wt. % carbon, therefore carbon-containing gas phase decomposition products must be formed to attribute for this discrepancy. In Figure 8.3A, the second stage of mass loss, which begins at ~25 wt. %, can be attributed to the oxidation of this residual carbon due to the presence of oxygen in the system.

It is also important to note that the heat release from the oxidation of carbon increases with increasing heating rate. Previous work investigating the burn rates of Al/PVDF films showed a faster burn rate in an oxygen-containing atmosphere.[9] This was explained by the added oxidation of the nAl by atmospheric oxygen.[9] The TGA/DSC data in Figure 8.3 further supports a faster burn speed in air as it indicates that oxygen plays an important role in oxidizing the PVDF, which has an increased heat release at higher heating rates.

When $Al_2O_3$ is incorporated into PVDF films, two main mass losses are also observed (Fig. 8.3B) corresponding to two distinct exotherms (Fig. 8.3D), the first of which occurs at a much lower temperature than in the pure PVDF. The decrease in onset temperature is 100-110 $^oC$, depending on the heating rate employed. This decrease in decomposition temperature of PVDF can be attributed to the PIR between $Al_2O_3$ and the condensed phase fluorine of the PVDF as has been previously seen in other Al/fluoropolymer systems such as Al/PTFE.[7] The PIR occurs prior to the first large exotherm in Figure 8.3D and initiates the lower temperature decomposition/oxidation of the PVDF. We observe an increase in our first exotherm in Figure 8.3D with an increase in heating rate similar to Al/PTFE[12]. There is also no significant mass loss before the PIR occurs, signifying that the $Al_2O_3$ reacts with PVDF through the condensed phase to catalyze the fluoropolymer's decomposition similar to Al/PTFE.[7] The second main mass loss, with an onset temperature between 400 and 500 $^oC$ in Figure 8.3B, occurs at the same temperature as pure PVDF. This mass loss can again be attributed to the oxidation of residual condensed phase carbon-containing species left behind from the decomposition of PVDF. This step is unaffected by the presence of $Al_2O_3$ in the film, as it occurs at the same

temperature with and without $Al_2O_3$. Figure 8.3B shows a final mass of ~40 wt. % corresponding to the 40 wt. % $Al_2O_3$ in the film. The remaining $Al_2O_3$ was later analyzed using XRD to see the extent of any fluorination of the $Al_2O_3$.

The PIR in the Al/PTFE system has been explained by Osborne et al. to be of significance to the oxidation of nAl mainly because of the fluorination of the $Al_2O_3$ shell exposing the Al core to allow for enhanced reaction kinetics.[7] The PIR of the $Al_2O_3$/PVDF system precedes the first main mass loss in the TGA similar to what has been observed in other Al/fluoropolymer systems.[7] As discussed in the T-jump ignition experiments, the nAl in the Al/PVDF system is oxidized by gas phase reactants. In addition to the potential exposure of the Al core after the PIR, the observed lower temperature exothermic mass loss seen in Figure 8.3B and C could play an additional important role in the reaction mechanism by releasing oxidative gas phase species more rapidly at a lower temperature. The first mass loss in Figure 8.3B, which correlates to the release of fluorine-containing gas phase species facilitated by the condensed phase reaction between PVDF and $Al_2O_3$, was also shown in Figure 8.3D to be increasingly exothermic with an increase in heating rate supporting the need for a high heating rate analysis of the exact nature of this decomposition.

*8.3.3. Fast-heating Chemistry by T-Jump TOFMS*

We begin with the mass spectrum of pure PVDF film electrospray onto a Pt wire at a snapshot in time (1.6 ms at a heating rate of ~ 4 x $10^5$ K/s) to show predominant species in Figure 8.4. T-Jump TOFMS allows for the collection of a full spectra every 0.1 ms allowing for higher heating rates consistent with combustion times.


***Figure 8.37.*** *MS @ 1.6 ms (~700 °C) of PVDF film and likely fragments labeled in spectra.*

Large masses (>50 m/z) are observed, which are identified with likely species in Figure 8.4. The most striking feature is the small amount of HF, which is just the opposite to that observed at low heating rates.[16]

Figure 8.5 shows the time resolved full spectra of the pure PVDF (A) and Al/PVDF (B). As seen in Figure 8.5, the PVDF decomposition products are detected earlier when nAl is present, corresponding to a decrease in the PVDF decomposition temperature.

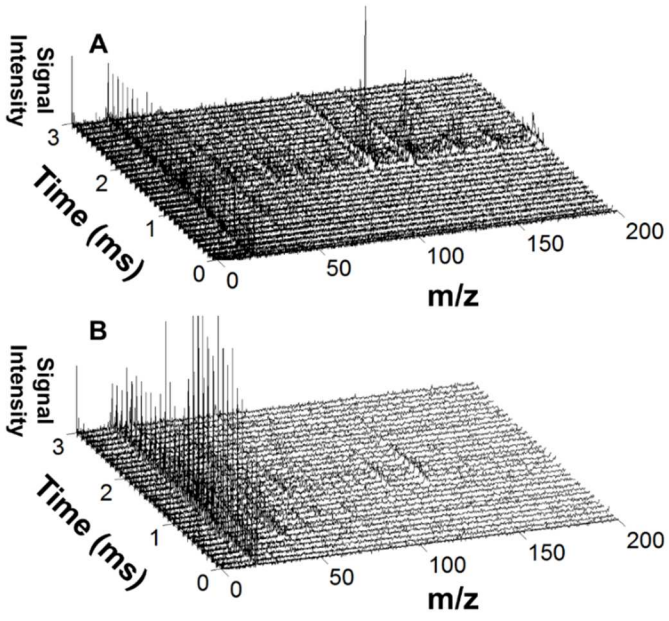


***Figure 8.38.*** *3D plots of time resolved spectra obtained from T-jump TOFMS of PVDF (A) and Al/PVDF (B) films.*

PVDF decomposition occurs at ~650 ºC in the pure PVDF film and at ~450 ºC in the Al/PVDF film. The temperature difference is about 200 ºC at the high heating rate of the T-jump experiment (~$10^5$ K/s) while the temperature difference is only 100 ºC in the previously published TGA/DSC experiments (20 ºC/s).[9] Adding Al also significantly diminishes formation of large mass species implying Al not only lowers the decomposition temperature, but promotes a more complete decomposition of the polymer.

Figure 8.6 shows detected species at the peak HF (A- 1.3 ms; 600 C) and peak AlF (B-1.8 ms, 780C) signal intensities. HF was detected prior to any AlF-containing gas phase species, consistent with nAl being oxidized by the gas phase PVDF decomposition product, HF. The nAl fluorination reaction would proceed as follows:

$$2Al + 6HF \rightarrow 3H_2 + 2AlF_3 \quad (1)$$

The evolution of $H_2$ gas in the MS is observed concurrently with detection of AlF as seen in Figure 8.6B. It is also important to note that the larger mass decomposition products vary slightly from the pure PVDF film. Fragments of m/z = 132 and 63 are observed, which are 1 m/z lower than the described 133 and 64 peaks above. This correlates to the loss of a hydrogen from these fragments, resulting from more HF production in the Al/PVDF case.

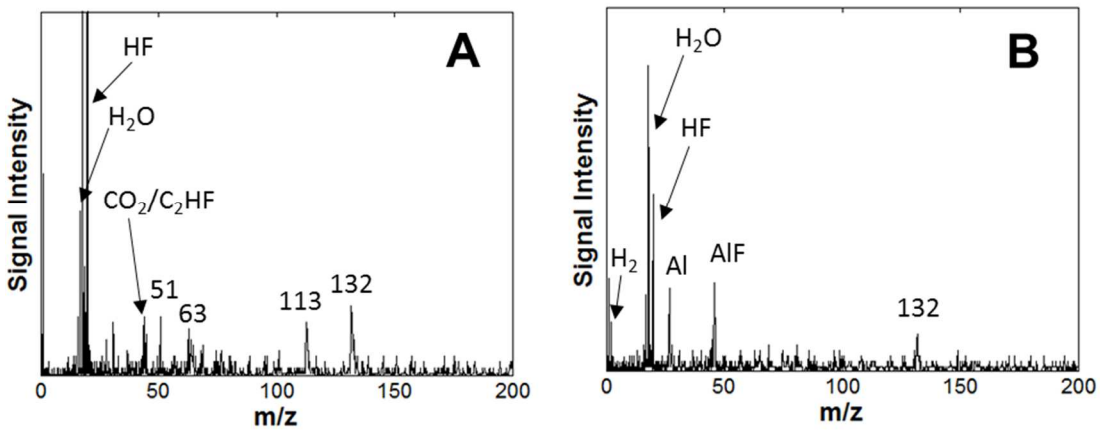


***Figure 8.39.*** *MS of Al/PVDF film at peak HF signal intensity (1.3 ms, 600 °C) and peak AlF signal intensity (1.8 ms, 780 °C).*

The PIR between the $Al_2O_3$ shell of the Al and condensed phase F-containing species is suspected to be the cause of the altered PVDF decomposition as the $Al_2O_3$ creates a boundary between Al and PVDF and the Al is unable to diffuse through the shell in the decomposition temperature range. The catalyzed PVDF decomposition begins at ~450 °C while the melting point of Al is not until 660 °C. While some may argue $Al_2O_3$ is acting as a co-reactant, in this context, the PVDF decomposition is said to be catalyzed simply because $Al_2O_3$ remains unchanged at the end of the process. This reaction promotes a lower temperature decomposition and increased HF generation from PVDF as seen in Figures 8.5 and 8.6. In order to isolate the role of $Al_2O_3$ in the reaction mechanism with PVDF, films were created containing 50nm $Al_2O_3$ particles in a PVDF matrix. Films of varying $Al_2O_3$/PVDF ratios were electrosprayed onto Pt wires for T-jump TOFMS. The mass of PVDF used in the precursor solution was kept constant for this particular study.

Figure 8.7 A-D show temporal HF and temperature profiles for alumina- and Al-containing films. For the Al case, 15 and 40 wt. % correspond to Al/PVDF equivalence ratios of 0.5 and 2 respectively. Increasing the alumina content results in both an earlier

onset (~450 $^{o}$C) of HF appearance as well as an increase. At higher temperatures HF evolution increases and does so well past the termination of heating. It is also important to note that these experiments are done in vacuum where the lack of heat transfer from the platinum filament to the surrounding atmosphere allows the wire to stay hot, well after the heating pulse is completed. The first HF increase is attributed to decomposition of PVDF catalyzed by the condensed phase PIR with $Al_2O_3$. We propose that the PIR results in the creation of condensed phase fluorinated $Al_2O_3$ products, along with some left over condensed phase $C_xH_yF_z$ species that presumably further decompose to account for the second stage of HF release. XRD analysis of $Al_2O_3$/PVDF films that were heated in an argon environment at 1000 $^{o}$C for 2 hours showed only the $Al_2O_3$ starting material (same phase) and no AlOF species (Fig. 8.S4). This implies that any surface reaction may lead to an amorphous fluorine-containing product. Sarbak et al. have also seen a similar result of no new peaks corresponding to new F-containing species on fluorinated gamma phase $Al_2O_3$.[17] It is also likely that the AlOF species formed on the surface of the $Al_2O_3$ decompose during further heating after the PIR occurs. The decomposition of AlOF species may also contribute to the second stage of HF release observed in Figure 8.7 A,B.

When using Al rather than alumina, a sharp HF peak is observed for the fuel lean sample (Fig. 8.7C) (15 wt. % corresponding to an equivalence ratio, φ, of 0.5), but the peak intensity is diminished and shifts to a later time for fuel rich samples (Fig. 8.7D). The equivalence ratio was determined taking into account the 81% active Al content of the Al nanoparticles used. The initial high intensity HF release is presumably due to the rapid decomposition of PVDF, which is catalyzed by the PIR between the $Al_2O_3$ shell of the Al and the fluorine of the PVDF. When there are large amounts of Al in the film, the early

stage HF is subsequently, rapidly consumed in the fluorination of Al resulting in the creation of the final reaction product, $AlF_3$.

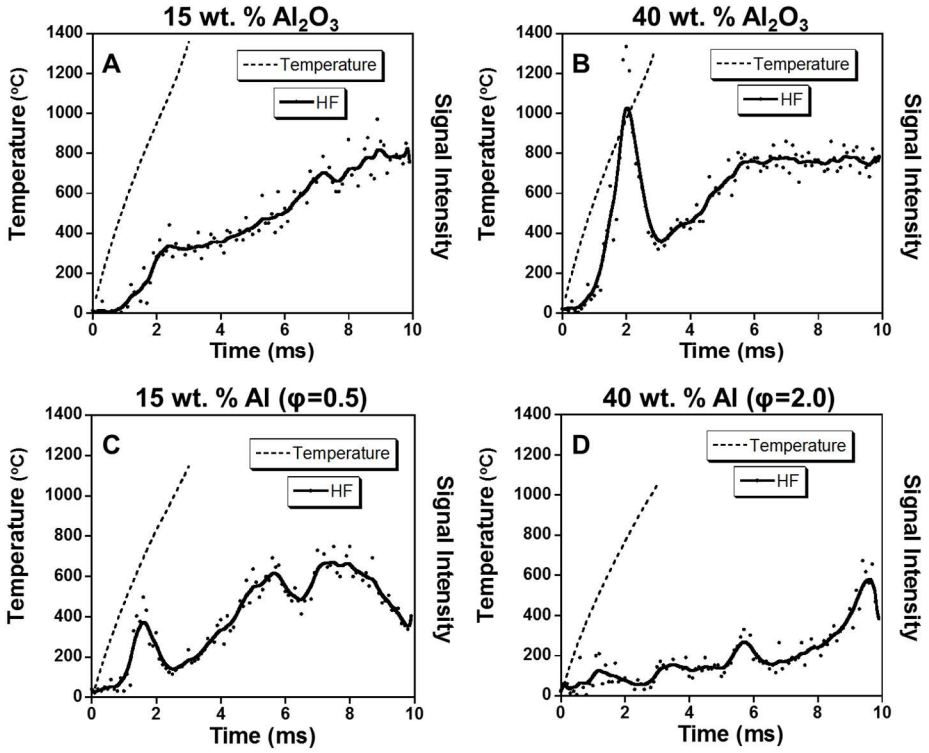


***Figure 8.40.*** *Temporal wire temperature and HF signal intensity for 15 wt. % $Al_2O_3$ (A), 40 wt. % $Al_2O_3$ (B), fuel lean 15 wt. % Al (C), and fuel rich 40 wt. % Al (D) containing PVDF films. Absolute signal intensity scale and approximate amount of film on the wire is consistent for A-D.*

The PIR facilitates a rapid release of HF that reacts with Al, leading to the creation of AlF species and hydrogen. The following reactions seen in Figure 8.8 outline this process with step A occurring first at ~450 $^oC$ and steps B, C, and D occurring in parallel:

| | |
|---|---|
| **A) Catalyzed PVDF Decomposition (PIR)** | $Al_2O_3 + -(C_2H_2F_2)_n- \rightarrow (C_xH_yF_z) + HF_{(g)}$ |
| **B) Direct Pyrolysis of PVDF** | $-(C_2H_2F_2)_n- \rightarrow (C_xH_yF_z) + HF_{(g)} + C$ |
| **C) Decomposition of Intermediates** | $(C_xH_yF_z) \rightarrow HF_{(g)} + C$ |
| **D) Fluorination of Aluminum** | $2Al + 6HF_{(g)} \rightarrow 2AlF_3 + 3H_{2(g)}$ |

HF generation is possible through three different reactions. Reaction A shows the catalyzed PVDF decomposition resulting in the rapid low temperature release of HF. As the $Al_2O_3$ concentration is increased (Fig. 8.7 B), more of the PVDF can react with the $Al_2O_3$ as seen by the increase in the first stage of HF release in comparison to the lower concentration case (Fig. 8.7A). PVDF that is not in direct contact with $Al_2O_3$ can pyrolize to form $C_xH_yF_z$ species, HF, and carbon (reaction B). The remaining $C_xH_yF_z$ species (reaction C) continue to decompose, releasing even more HF over a prolonged period of time. The decomposition of $C_xH_yF_z$ species and pyrolysis of PVDF are proposed to be much slower processes as the secondary HF release peaks in Figure 8.7 are much broader than the low temperature HF release from the $Al_2O_3$ catalyzed decomposition. Fluorination of Al (reaction D) occurs once HF available, and the Al core is either exposed by the fluorination of its $Al_2O_3$ shell or the Al has diffused outwards as has been demonstrated in previous reports.[18, 19]

*8.3.4. Al/PVDF Reaction Mechanism Summary*

The above results show the importance of the nascent oxide shell on the aluminum nanoparticles to the Al/PVDF reaction occurring in the nanocomposite thin films. Before aluminum oxidation can occur, the $Al_2O_3$ + PVDF PIR forms $Al_xO_yF_z$ species while also rapidly producing $HF_{(g)}$ through the decomposition of $C_xH_yF_z$ species. This early stage $HF_{(g)}$ release should be limited by the available reaction sites on the surface of the $Al_2O_3$. This is demonstrated by the increase in relative HF signal intensity with an increase of $Al_2O_3$ shown in Figure 8.7. The unstable $Al_xO_yF_z$ species formed during the PIR

decompose with further heating, resulting in the second, prolonged stage of HF release observed in the temporal plots in Figure 8.7. T-Jump TOFMS analysis in Figure 8.6 also showed the release of $H_2O_{(g)}$ from the surface of the $Al_2O_3$ that precedes any $HF_{(g)}$ generation. Sarbak has proposed that fluorine can form bonds with the surface of $Al_2O_3$ that are facilitated through OH groups on the surface of $Al_2O_3$[17] as follows:

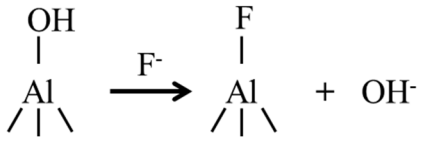


In the case of the condensed phase PIR between $Al_2O_3$ and PVDF, $H_2O$ must leave the surface sites in order for F to bind.

Any substantial changes to the alumina shell, as for example creation the $Al_xO_yF_z$ species will only increase to enhance the transport of elemental Al from the core to react with $HF_{(g)}$ producing $AlF_3$ and $H_2$. Unstable $Al_xO_yF_z$ species can go on to decompose, along with any residual condensed phase fluorine-containing PVDF decomposition products, resulting in the secondary prolonged release of HF that is observed in the TOFMS results.

*8.3.5. Burn Speed Analysis*

The results in Figure 8.7 show that the amount of $Al_2O_3$ in the system directly correlates to the amount of early-stage HF that is released. In order to test the effect of an enhanced PIR between $Al_2O_3$ and PVDF on any macroscopic observable, $Al_2O_3$ was added to the precursor solution for stoichiometric Al/PVDF films in varying quantities and burn speeds were measured under 1 atm of argon. As shown in Figure 8.8, the addition of $Al_2O_3$

resulted in a decrease in burn speed when compared to the stoichiometric Al/PVDF film (0 wt. % of added $Al_2O_3$) signifying that, although $Al_2O_3$ promotes the low temperature release of HF, this does not translate into any enhancement in global combustion rate.

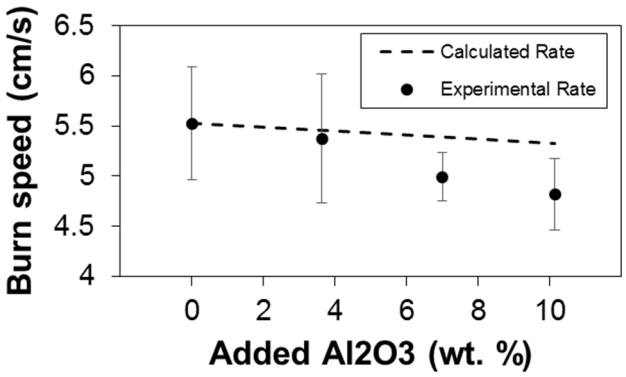


***Figure 8.8.*** *Burn speeds for stoichiometric Al/PVDF films with varying amounts of added $Al_2O_3$.*

Four possible causes of such a decrease in burn speed caused by the addition of $Al_2O_3$ include: $Al_2O_3$ acting as a diluent thus decreasing the energy available for propagation, $Al_2O_3$ catalyzes the release of oxidizing species faster than Al can react with these species, the creation of condensed phase $Al_xO_yF_z$ species by direct reaction of $Al_2O_3$ with PVDF, and/or a morphological change in the film altering the interfacial contact area between Al and PVDF.

In order to estimate the isolated effect of $Al_2O_3$ acting as a heat sink during the reaction of Al and PVDF, the ratio of reaction rates of a pure Al/PVDF stoichiometric film, R, and an $Al_2O_3$-containing film, $R_{Al_2O_3}$, was approximated to be equivalent to the respective burn speed ratio, $\frac{\nu_{exp}}{\nu_{calc}}$, where $\nu_{exp}$ is the experimentally determined burn speed for the pure Al/PVDF film and $\nu_{calc}$ is the theoretical burn speed for a film with an added amount of $Al_2O_3$. We further assume that all things being equal, if this is just a dilution

effect then the burn speeds should scale as the effective heat of reaction as shown in Equation 2.

$$\frac{R}{R_{Al_2O_3}} = \frac{\Delta H_{rxn}}{\Delta H_{rxn}\left(1\text{-}\chi_{Al_2O_3}\right) + \left(C_P\Delta T\right)_{Al_2O_3}\left(\chi_{Al_2O_3}\right)} \approx \frac{\nu_{exp}}{\nu_{calc}} \quad (2)$$

The calculated burn speed shown in Figure 8.8 corresponds to $\nu_{calc}$ in the following equation for the respective amount of added $Al_2O_3$. The enthalpy of reaction for the stoichiometric Al/PVDF film with no additional $Al_2O_3$, $\Delta H_{rxn}$ (kJ/mol), was calculated for the fluorination of Al by HF, which can be seen in reaction D. $(C_P\Delta T)_{Al_2O_3}$ represents the energy required to heat the added $Al_2O_3$ from room temperature to the experimental ignition temperature at 1 atm of argon (~825 ºC as shown in Fig. 8.2). Heats of formation for HF and $AlF_3$ of -273.2 and -1209 kJ/mol, respectively, and a $(C_P\Delta T)_{Al_2O_3}$ of 90.5 kJ/mol were obtained from the NIST Webbook. The theoretical amount of HF generated from the complete decomposition of the PVDF in the film is taken into account when calculating the mole fraction of $Al_2O_3$, $\chi_{Al_2O_3}$. The reaction rates in Equation 2 are equal to the enthalpy of reaction divided by a characteristic time. Evident from the calculated curve plotted in Figure 8.8, the heat absorbing effect of $Al_2O_3$ is only partially responsible for the experimental decrease in burn speed.

The second potential explanation for the decrease in burn speed is $Al_2O_3$ catalyzing the PVDF decomposition before the Al is ready to react with the gas phase HF being generated. This situation is highly unlikely because the T-jump TOFMS results in Figure 8.7C and D show a decrease in early onset HF signal intensity for fuel rich samples. If the Al was unable to react during the early-onset HF release, the preliminary HF signal intensity would be consistent among fuel rich (Fig. 8.7D) and fuel lean (Fig. 8.7C) samples. Figure 8.7A and B also show that increasing the amount of $Al_2O_3$ in a PVDF film will

increase the amount of early onset HF generated, but does not alter the temperature in which the catalyzed decomposition occurs.

The third potential effect that added $Al_2O_3$ may have is that in addition to catalyzing the decomposition, the $Al_2O_3$ is reacting with the PVDF and/or PVDF decomposition products to form $Al_xO_yF_z$ species, thusly decreasing the amount of reactive fluorine to fluorinate the Al. XRD analysis of $Al_2O_3$/PVDF films after heating (Fig. 8.S4) do not show any crystalline $Al_xO_yF_z$ species and the TGA results in Figure 8.3B show a final mass that is identical to the initial mass of pure $Al_2O_3$ in the film. Both of these results show that while the $Al_2O_3$ has a catalytic effect on the decomposition of PVDF, it does not decrease the amount of reactive fluorine species available to fluorinate the Al.

The final, and what we consider to be an additional most likely explanation for the burn speed reduction is the change in interfacial area between Al and PVDF with the addition of $Al_2O_3$. Adding $Al_2O_3$ hinders the fluorination of aluminum by acting as a storage mechanism for fluorine. This is an interfacial area explanation, and if the conjecture is correct than there may be advantages of to making laminates composed of Al/PVDF and $Al_2O_3$/PVDF bilayers. We are in the process of exploring this possibility.

*8.4. Conclusion*

The PIR between $Al_2O_3$ and PTFE has been previously identified as a key initiating step in the reaction between aluminum and the fluoropolymer. This PIR was recently identified as a key component in the Al/PVDF reaction; a system that has gained attention due to the ease of processing and ability to create films with high mass loadings of nanosized constituents using electrospray deposition methods.[9] Using T-jump ignition in different environments, it was determined that the Al in the Al/PVDF system does not react

in the condensed phase and is oxidized by gaseous HF released as a decomposition product of PVDF. TGA/DSC analysis showed an exothermic decomposition for PVDF film in the presence of oxygen and also clearly showed a low temperature PIR when $Al_2O_3$ was incorporated into the film. These experiments also showed a clear increase in heat release for the PIR and PVDF decomposition with an increase in heating rate, further supporting the need for high heating rate analytics to be performed.

The Al/PVDF reaction mechanism was further probed using T-jump TOFMS and the condensed phase PIR between PVDF and the $Al_2O_3$ shell of the nAl caused the PVDF to decompose more completely and at a lower temperature. This more complete decomposition promotes the generation of gas phase HF that can go on to oxidize the Al. $Al_2O_3$ was added to Al/PVDF films to see if increasing the amount of low temperature HF generated would have an effect on the burn speed of a thin film. No burn speed enhancements were observed and it was concluded that adding $Al_2O_3$ to the system hinders the Al/PVDF reaction propagation in the film. Future work will entail using these results to create multilayer films containing Al, $Al_2O_3$, and PVDF that can maintain the desired Al/PVDF interfacial area while also containing thin layers of $Al_2O_3$/PVDF that can rapidly supply the Al with reactive HF. Further understanding of the Al/PVDF reaction mechanism is essential to the understanding of multi-layered laminates based off of the Al/PVDF system and multi-component thermite systems such as Al/CuO/PVDF.

# Chapter 9: Investigating the Reaction Mechanism of Al/PVDF Films at 1 atm

*Summary*

The ability to probe reaction dynamics in transient energetic systems is critical to the analysis of fast chemistry processes such as rapid thermal decomposition, ignition, and combustion of energetic materials. Rapid reactions pertaining to nanoparticle systems have been characterized in the past using a temperature jump time-of-flight mass spectrometer (T-Jump/TOFMS) which requires the sample (100's of μg) to be coated on a thin platinum filament and heated within the vacuum environment of the system. A molecular beam sampling system for a reflectron time-of-flight mass spectrometer (MBMS) was developed and coupled with high speed videography to probe the reaction mechanisms of energetic nanocomposites in anaerobic environments at elevated pressures (1 atm). Nano-aluminum/ Poly(vinylidene fluoride) (Al/PVDF) based thin films were analyzed using this system's capability to investigate the time resolved speciation of gas phase products and intermediates during ignition and film combustion propagation. Results were compared with the previously reported Al/PVDF reaction mechanism studied using T-Jump/TOFMS to further understand how these films react under ambient conditions. Silica and iodine were added into the Al/PVDF films to investigate their effect on the reaction mechanism and film propagation.

## *9.1. Introduction*

The fabrication of energetic nanocomposites employing metallic nanoparticles has become a promising frontier in the search for new materials with a high-

energy densities. Enhanced reactivity derived from increased specific area and surface energy, higher mass diffusivity, and decreased diffusion length between fuel and oxidizer make these materials highly desirable as a fuel source in solid propellant systems [1]. Typically, solid propellants utilize polymer based binders which not only provide the composites their mechanical integrity and ability to prevent loss of nanostructure due to sintering, but can also act as an internal oxidizer source as in the case of fluoropolymer binders [2,3].

In this study, a Molecular Beam Mass Spectrometer (MBMS) coupled with high speed videography was developed to probe the reaction mechanism at 1 atm of electrosprayed thin films comprised of readily available Nano-aluminum and the fluoropolymer Poly(vinylidene fluoride) (Al/PVDF). Previous work utilizing Linear Time-of-Flight Mass Spectrometry coupled with Temperature-Jump wire ignition (T-Jump/TOFMS) characterized the reaction mechanism of 10-100 μg of Al/PVDF material coated on a thin platinum wire within a high vacuum environment (~$10^{-6}$ Torr) [4]. This work proposed a reaction mechanism which stated that the prerequisite for ignition and self-sustaining combustion of the material relies on the decomposition of PVDF to hydrogen fluoride (HF) which reacts exothermically with aluminum to form aluminum fluoride ($AlF_3$) and hydrogen gas ($H_2$) [4]. This work is discussed, in detail, in Chapter 8 of this dissertation.

Though both mass spectrometer systems have the capability to report time resolved speciation of gas phase products at similar sample rates, only the MBMS has the capability to probe real time flame products of relatively large samples at elevated pressures. Since the T-Jump/TOFMS system is performed in vacuum, gas phase

interactions are limited. Unlike the TOFMS system, the ignition and combustion of the film within the MBMS system occurs outside of the of the ionization region, allowing for an added degree of customizability of the sampling environment. This allows for the use of larger samples within a chemical environment which is rich in gaseous collisions. As a result, various reaction products not seen in vacuum can be detected during the full duration of film propagation (~1 second), allowing the reaction to be studied in practical application conditions. The MBMS also possess the ability for enhanced mass spectrum resolution utilizing the systems reflectron design which doubles the focal length of the flight tube [5].

Previous studies which have incorporated additives within the Al/PVDF films, such as iodine or silica, have shown that flame propagation speed is altered, most likely due to changes in the combustion chemistry. Iodine addition into electrosprayed Al/CuO nanothermite microparticles has also been studied targeting biocidal applications.[6] This study also looks to use the MBMS to characterize the variations in the reaction mechanism of multi-constituent films by analyzing time resolved speciation of gas phase products [6-7].

## *9.2. Experimental*

### *9.2.1. Materials*

Nano-Aluminum (nAl) (~85nm) utilized in this study was purchased from Novacentrix and determined to be 81% active via thermogravimetric analysis (TGA). Poly(vinylidene fluoride) powder (PVDF) (MW=534000), dimethylformamide (DMF) (99.8 wt. %) solvent, Iodine (99.8 % wt.) were purchased from Sigma-Aldrich. Mesoporous Silica (99 wt. %) (~1 μm) was synthesized through the process of spray drying [8]. High-speed video was taken using a Phantom v12.0 digital camera running Phantom

692 software and operating at 3000 fps. A quartz tube (~1 m) was purchased from Quark Glass, melted at the end by a hydrogen flame, and sanded down in order to create a small orifice (150-200 μm diameter) at the end.

### *9.2.2. Film Synthesis*

The synthesis of Al/PVDF films was conducted using the proven technique of scalable electrospray assembly. Starting with a thoroughly mixed precursor solution of Nano-Aluminum, PVDF, and DMF, this technique employs electrical forces to introduce hydrodynamic instabilities to enable the direct fabrication of nanoparticle polymer composites [3,9]. The nature of this assembly process makes it possible for these structures to be synthesized at much higher precursor viscosities and therefore made highly tunable in size, shape and reactant content [3]. This technique is discussed, in detail, in Chapter 7 of this dissertation.

### *9.2.3. Characterization*

Ignition of stoichiometric Al/PVDF films was conducted in a 1 atm anaerobic environment at the end of a 10-mm diameter quartz tube while ambient atmosphere was maintained by a constant inlet and outlet flow of nitrogen gas. Electrospray synthesized films (5-8 mm × 2.5-3.5 mm × ~0.10 mm) were sandwiched between two thin nichrome wires (0.10" Diameter) anchored to the ends of two copper leads and subsequently ignited via Joule heating.

During combustion, hot gaseous products rapidly expand through the sampling orifice at the end of the quartz tube into an intermediate region of relatively low pressure (~$10^{-3}$ Torr), and into the E-gun (70 eV) ionization chamber (~$10^{-6}$ Torr) through an adjacent skimmer cone (450 μm I.D.), creating a molecular beam (Fig. 9.1). The essential

feature of the MBMS relies on this sudden transition from a continuum environment (reaction event) to one which is collision-less (E-gun ionization region/flight tube). The sudden transition in tandem with the creation of an ultra-cold supersonic molecular beam enables the preservation of the sample until reaching the detector of the mass spectrometer [10].

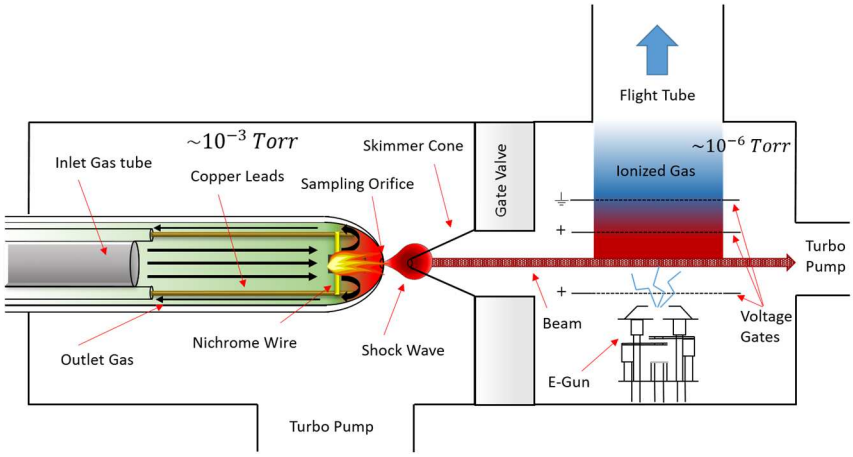


***Figure 9.1.*** *Experimental setup and Molecular Beam Mass Spectrometer schematic of flame sampling during combustion.*

Roughly 3.5 seconds worth of time resolved data can be captured utilizing a 600 MHz Teledyne LeCroy Oscilloscope at a sampling rate of 1-3 full mass spectra per millisecond (1-3 kHz). Pre-ignition preparation requires the alignment of the sampling orifice to the skimmer cone which can be achieved by optimizing the distance between the end of the quartz tube and skimmer cone (<1cm), and maximizing the detector signal intensity of the atmospheric gas. Quality of the molecular beam can also be measured through a ratio of the intensity of the unblocked beam to the intensity of a partially blocked

beam utilizing the skimmer cone gate valve. Typical beam to background ratios were found to be roughly 4:1.

Triggering the wire heating, data capture, videography, and voltage gates simultaneously using a single trigger source provides the opportunity for comprehensive analysis of the entire combustion event. Mass spectrum characterization of the gaseous combustion products of distinct Al/PVDF films containing additives of 20 wt. % $I_2$ and 5 wt. % $SiO_2$, respectively, were also performed in this manner.

## *9.3. Results and Discussion*

### *9.3.1. MBMS and T-Jump TOFMS Comparison*

Al/PVDF samples were first run in both T-Jump/TOFMS and MBMS systems. Figure 9.2 illustrates the resulting averaged mass spectra recorded by each device in anaerobic conditions during rapid heating. At first glance, peaks of roughly equivalent intensity with m/z values between 30 and 140 exist in the vacuum environment. This corroborates with the notion that, in a vacuum environment, gas phase species detected are those that form before and immediately following ignition. These unstable intermediate species have virtually no opportunity to interact with other molecular species given their long mean free path in this environment. Conversely, the MBMS spectrum illustrates a chemical landscape which is devoid of the same relatively high mass species depicted in the vacuum spectrum, but rich in notable products such as acetylene ($C_2H_2$), butane ($C_4H_{10}$), and other lower mass hydrocarbons. Previous studies have shown drastic burn speed differences between aerobic and anaerobic environments, as detailed in Chapter 7.

It is proposed that the formed hydrocarbon species burn in the presence of oxygen enhancing the reactivity of the composite.

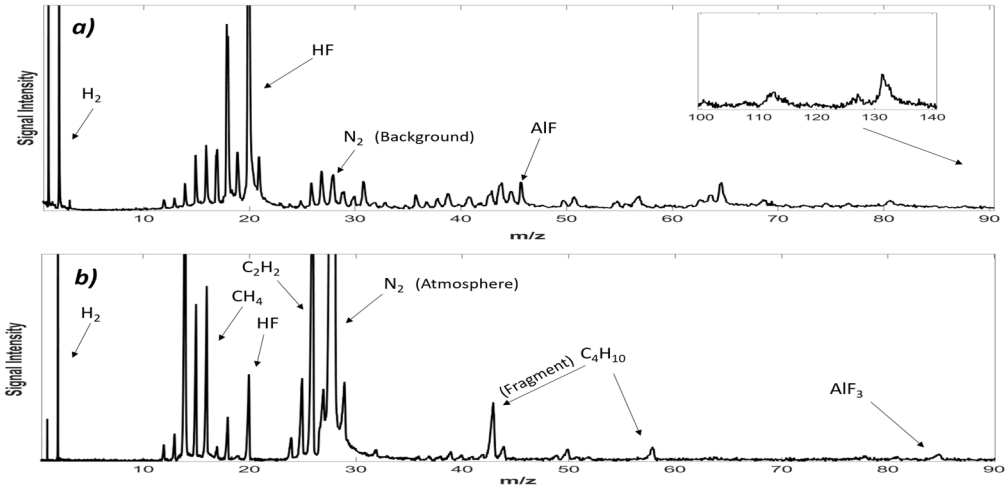


***Figure 9.2.*** *Al/PVDF combustion mass spectra in anaerobic environments: a) Vacuum (*$\sim 10^{-6}$ Torr*) T-Jump/TOFMS sampling and b) 1 atm $N_2$ MBMS sampling.*

Though detection of HF and $H_2$ was achieved in both systems, the final product species, $AlF_3$, was detected only in the MBMS. In the vacuum environment of the TOFMS, the formation of $AlF_3$ is limited due to the gas phase oxidizer, HF, being rapidly removed from the aluminum (Al) fuel due to the low pressure environment. However, the intermediate species aluminum monofluoride (AlF) is detected, signifying the initiation of reaction [11]. The conditions of the MBMS allow for continuous interactions of HF and Al, favorable to the formation of $AlF_3$. The detection of $AlF_3$ in the MBMS experiment implies that the flame temperature must be higher that the sublimation temperature of $AlF_3$ (1291 $^oC$) as this system can only detect gas phase products.

*9.3.2. Additives in Al/PVDF Thin Films*

Using the Al/PVDF spectrum as a reference, one can probe the combustion reaction mechanisms by adding one or more chemical components to see how the mechanism is

affected. An additive may or may not add energetic benefit to the system. Ongoing studies have suggested that films with homogenously dispersed mesoporous silica have enhanced energy transfer properties as a result of efficient convective flow transfer, leading to increased flame propagation speeds [7]. Energetic materials incorporating Iodine have also been previously studied to be used for biocidal applications [6]. Figure 9.3 shows the averaged MBMS spectra during burning for pure Al/PVDF, Al/PVDF/$I_2$, and Al/PVDF/$SiO_2$.

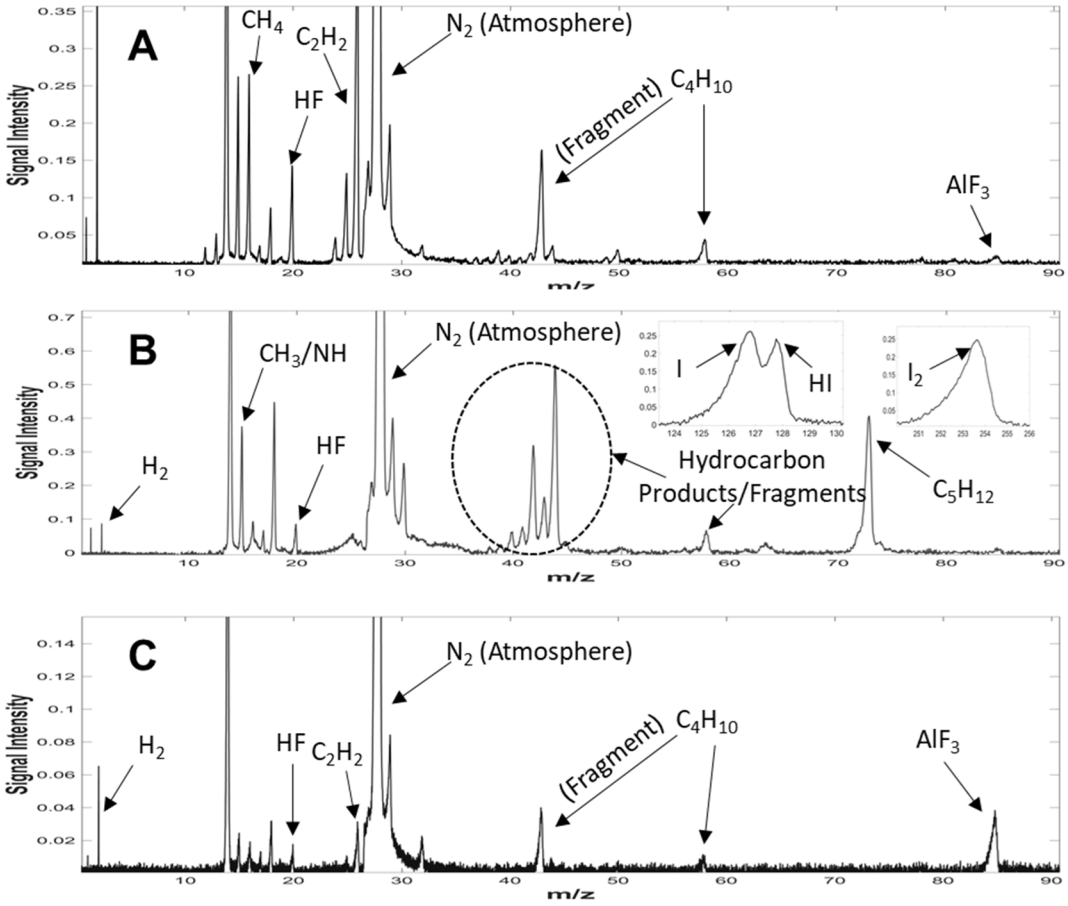


***Figure 9.3.*** *Averaged MBMS spectra during film burning of Al/PVDF(A), Al/PVDF containing 20% w.t. $I_2$ (B) and Al/PVDF containing 5% w.t. $SiO_2$ (C).*

When analyzing the mass spectrum of Al/PVDF/$I_2$, a multitude of hydrocarbon species can be observed between m/z values of 30 and 70, along with the even heavier species of atomic iodine (I) and hydrogen iodide (HI). Comparison of this iodine film spectrum (Fig. 9.3B) with the spectrum of Al/PVDF in vacuum (Fig. 9.2A) reveals the existence of the largest species detected (m/z = 132), previously proposed to be $C_6H_3F_3$ [4]. As explained above, species detected in vacuum have little to no interactions with one another, thus limiting the dissociation of larger molecules due to lack of heat transfer. Collisions within the 1 atm conditions of the MBMS are plentiful and thus provide opportunities for larger gas phase species to heterogeneously react or further decompose. The existence of the 132 species in the iodine film, which is not observed in the pure Al/PVDF film, would suggest that the iodine containing film simply does not burn hot enough to decompose this species. The iodine must act as a heat sink or boundary layer between fuel and oxidizer, slowing the transfer of energy propagating through the film and thus making it more likely for relatively temperature sensitive products to exist. Previous work has shown that $I_2$ can embed itself in the $Al_2O_3$ shell of the Al and was still detected in T-Jump TOFMS experiments even after particles were washed with hexane [6]. The $I_2$ embedded in the shell may impede the diffusion of fuel and oxidizer in this system resulting in reduced reactivity and slower burn speeds. Figure 9.4 shows the optical intensity during burning collected from high speed videography.

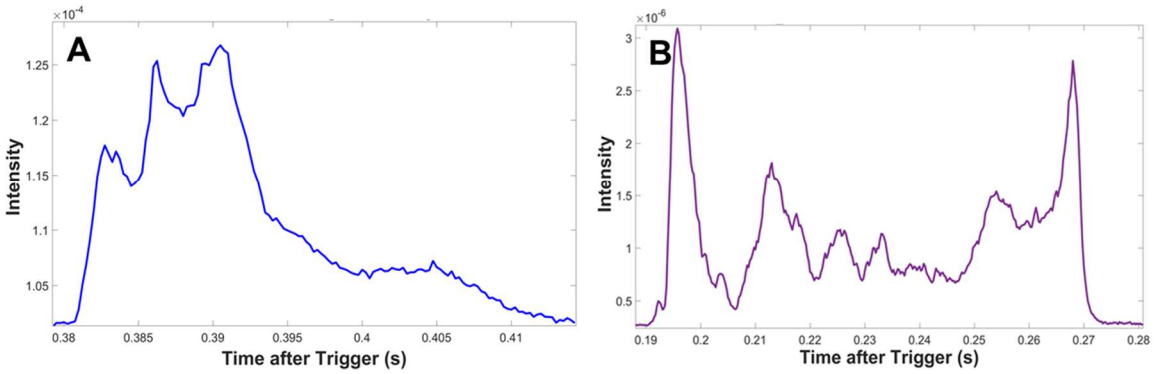


***Figure 9.4.*** *Optical emission during burning from coupled high speed videography of Al/PVDF (A) and Al/PVDF/$I_2$ (B) films.*

The fluctuating optical emission supports the theory that iodine is impeding the fluorination of Al and must be removed from the interface prior to combustion.

The purpose of adding elemental iodine to an energetic nanocomposite is to release gas phase $I_2$ during combusting resulting in simultaneous high temperatures and biocidal agent release. The MS in Figure 9.3B unfortunately shows that for this system, the iodine is not simply gasified, but forms HI, which does not share the same biocidal effectiveness as $I_2$. The formation of HI is proposed to occur due to the abundance of $H_2$ produced by the fluorination of Al by HF as shown in the equation below:

$$2Al + 6HF \rightarrow 2AlF_3 + 3H_2$$

This result demonstrates the need to examine the reaction products under application conditions such as those represented in the MBMS. In a vacuum environment, HI may not be detected due to the lack of exposure of $I_2$ to $H_2$ at the temperatures required for reaction between the two components.

Burn speed enhancements have been observed with the addition of mesoporous $SiO_2$ into Al/PVDF films in a tangential study [7]. This enhancement may suggest an increase in the flame temperature during burning. Preliminary findings suggest

mesoporous silica increases the rate of HF production while simultaneously promoting flame propagation via convection due to its porous nature [7]. The MS in Figure 9.3C shows a decrease in hydrocarbon formation in comparison to the pure Al/PVDF (Fig. 9.3A). The mesoporous $SiO_2$ may be catalyzing the decomposition of PVDF leading to the formation of relatively more HF. $Al_2O_3$ has shown a similar effect on the decomposition of PVDF as described in Chapter 8. The analysis of time resolved speciation of HF and the main product species, $AlF_3$, in Figure 9.5 also appear to support these findings. The signal intensities were normalized to the background nitrogen signal in order to qualitatively compare the ratio of species. Though not directly evident, the stark difference in the intensity of $AlF_3$ products detected between the pure Al/PVDF film and the one containing silica could indicate both the relative temperature of film burning and relative rate of PVDF decomposition to HF. Whether or not the $AlF_3$ product was detectable, the widths of each HF peak act as an indicator of how long the combustion event occurred, suggesting in this case that the film with silica consumes the oxidizing agent, HF, faster resulting in an increased temperature and burn speed. Figure 9.5b depicts the maximum HF release to occur at the same time as $AlF_3$ which indicates that, even though figure 9.5b superficially reports a smaller fractional intensity of HF compared to Figure 9.5a, the vast amount of HF has already been consumed.

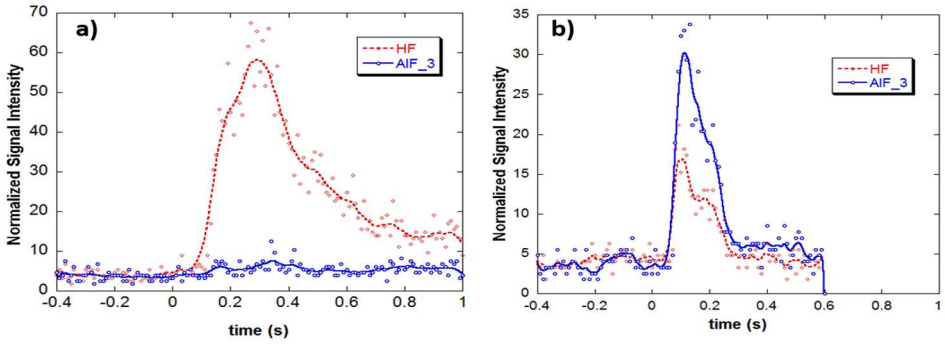


***Figure 9.5.*** *Film Burning Species over time in $N_2$ for a) Al/PVDF and b) Al/PVDF/$SiO_2$ mixtures are stoichiometric with additives comprising of 5% w.t. $SiO_2$ and 20% w.t. $I_2$.*

## *9.4. Conclusion*

The reaction mechanism of combustible Al/PVDF films was characterized by the time speciation capabilities of the Molecular Beam Mass Spectrometer and Linear Time-of-Flight Mass Spectrometer. By comparing the heating environments of the MBMS and TOFMS, insight to the importance of the reaction environment of these films was obtained, revealing the tendency of larger molecules to fully react and decompose under conditions of elevated pressure. Likewise, conclusions about characteristics such as film burning temperature and propagation speed can be inferred and distinguished among films with varying chemical components. Further analysis of this study can be greatly strengthened and enhanced by the inclusion of a spectrometer to enable quantitative temperature measurements and corroborate the findings so far.

# Chapter 10: Summary

## *10.1. Conclusions*

The objective of this dissertation was to probe the reaction mechanisms of energetic nanocomposites in order to understand how composite chemistry, architecture, and energy release are related. This was done by investing the oxidation mechanisms two non-traditional types of fuels, tantalum nanoparticles (nTa) and molecular Al clusters, in addition to creating multiple new analytical techniques to probe these reactions. The conclusions drawn in this dissertation have demonstrated characteristics of a variety of energetic nanocomposites that may be used to create tunable energetics for future applications.

In Chapter 2, I describe the need for high heating rate analytics in order to accurately study energetic nanocomposite systems. I described one commercial technique capable of high heating rates using Protochips thermal E-chips capable of *in situ* and *ex situ* TEM and SEM analysis. In addition, two modifications to the T-Jump TOFMS system were discussed that enable high heating rate speciation of air sensitive compounds and simultaneous acquisition of temporal thermal data and speciation. The design and fabrication of a MBMS system was also presented that adds flexibility in the sampling environment and types of samples that can be studied via time-of-flight mass spectrometry.

The oxidation mechanisms of nTa and Ta based nanothermites were described in Chapter 3 to aid in the development of a global reaction mechanism for nanosized metal fuels. The active metal core of nTa is immobile during ignition, unlike the more commonly studied nAl fuel. This allowed for the study of how oxide shell phase changes affect the ignition process. High heating rate TEM studies showed that oxidation occurring below the crystallization temperature of the nascent $Ta_2O_5$ oxide shell follows the Deal-Grove

model of oxide growth. Cracks were visible in the nTa shell when oxidation occurred above the $Ta_2O_5$ crystallization temperature that may be enhancing oxygen diffusion to the core resulting in a kinetically limited oxidation mechanism. The ignition temperature of nTa based thermites occurred after the $Ta_2O_5$ crystallization temperature and appeared to be independent of the metal oxide employed.

The decomposition and oxidation mechanism of two different Al cluster compounds were studied in Chapters 4 and 5 using the described ASSH for the T-Jump TOFMS system. Both clusters showed the release of gas phase Al during rapid heating. In addition, the oxysalt, $KIO_4$, was physically mixed with the $[AlBr(NEt_3)]_4$ tetrameric cluster demonstrating, to the best of my knowledge, the first known experimental work done employing a molecular Al compound in an energetic formulation. Preliminary work on using a coating to mitigate oxidation of these types of materials in an ambient environment was discussed in Chapter 5. The conclusions in this work demonstrate that the ASSH coupled T-Jump TOFMS system can be employed to study the oxidation of air sensitive compounds at high heating rates using only a small amount of material.

In Chapter 6, the nanocalorimetry coupled TOFMS system described in Chapter 2 was used to investigate the reaction mechanisms of Al/CuO nanolaminates. A solid-state ignition mechanism was observed and the effect of bilayer thickness on the reaction mechanism was explored. Samples with an individual bilayer thickness of 33 nm showed a single step reaction mechanism, occurring primarily in the condensed phase, due to this sample showing the highest AlO:Al ratio in the MS. These films demonstrated the highest maximum power output, but lowest overall energy release. The decreased energy release is attributed to the loss of active material in the premixed regions of the interface. The

premixed interface thickness was calculated to be 9.3 nm with an efficiency factor of 0.31. This system was also able to accurately measure the ignition temperature, which is overestimated when using optical methods to analyze small samples. These ignition mechanisms showed good agreement with a previously developed ignition model based on individual bilayer thickness.

An electrospray based synthesis method was described in Chapter 7 that enabled the creation of tunable microparticle and thin film energetic nanocomposite architectures. This chapter also surveyed multiple systems assembled in these geometries. The reaction mechanism of free standing nAl/PVDF thin films was explored, in detail, in Chapter 8. Using T-jump ignition in different environments, it was determined that the Al in the Al/PVDF system does not react in the condensed phase and is oxidized by gaseous HF released as a decomposition product of PVDF. A pre-ignition reaction (PIR) between the $Al_2O_3$ shell of nAl and PVDF that accelerates the release of HF in the initial stages of heating was identified as a key component in the reaction. The conclusions made in this work will be vital in the design of customizable energetics employing a PVDF binder with nanosized metal fuels.

To further probe the reaction mechanism of the nAl/PVDF system under conditions more representative of application environments, the MBMS system discussed in Chapter 2 was employed. Results were compared with the previously reported Al/PVDF reaction mechanism studied using T-Jump/TOFMS to further understand how these films react under ambient conditions. The production of hydrocarbon species was observed under ambient conditions, which may attribute to the enhanced burn speeds measured in aerobic

environments. Iodine and mesoporous silica were added into the Al/PVDF films to investigate their effect on the reaction mechanism and film propagation.

*10.2. Recommendations for future work*

*10.2.1. Incorporating nTa into Microparticles and Thin Films*

Now that we have a better understanding of the oxidation mechanism of nTa and how it reacts with metal oxides, we can use this material as a substitute for nAl to probe the effect of a composite's microstructure. For example, in Chapter 7, we propose that the gelled nAl/NC microparticles show enhanced reactivity in comparison to neat nAl due to the prevention of nAl sintering during reaction. Preliminary work has been done creating Ta/CuO nanothermite microparticles. The electrosprayed Ta/CuO nanothermite microparticles and Ta/CuO physical mixtures were ignited in a confined combustion cell and results are shown in Figure 10.1.

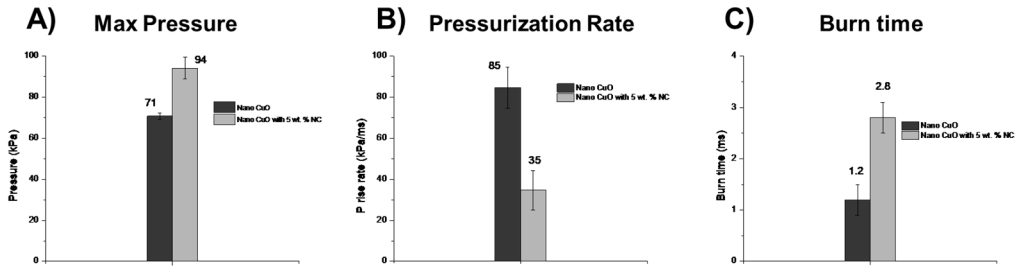


***Figure 10.1.*** *Combustion cell results comparing the max pressure (A), pressurization rate (B), and burn time (B) for electrosprayed and physically mixed Ta/CuO nanothermites.*

The pressurization rate comparison in Figure 10.1B shows that the gelled microparticle architecture actually decreases the pressurization rate where in an Al based system the pressurization rate increases significantly. This discrepancy is most likely due to the fact that nTa is an immobile fuel during ignition/combustion and does not sinter prior to reaction like nAl. More studies can be done incorporating this fuel into other systems to tweeze out what is happening in more commonly employed nAl based systems.

*10.2.2. Future Studies on Al Clusters*

The studies performed in Chapters 4 and 5 looked at the anaerobic decomposition of Al clusters and decomposition of pre-oxidized materials at high heating rates. A modification to the ASSH has been designed and fabricated allowing for "oxygen dosing" of the material within the mass spectrometer system. A prototype for this modification is shown in Figure 10.2.

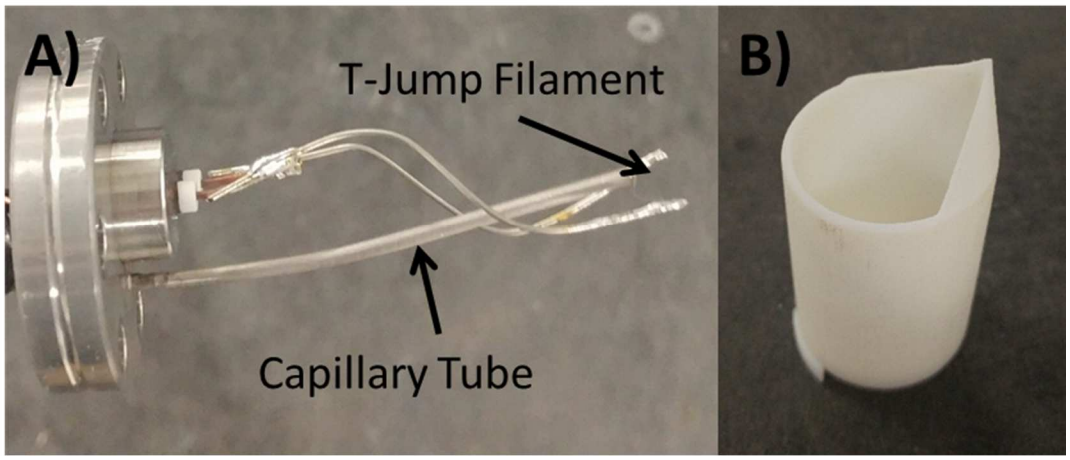


***Figure 10.2.*** *Custom T-Jump probe faceplate with capillary tubing (A) and 3D printed collar for use with this faceplate (B).*

The custom T-Jump probe faceplate would allow for oxygen to be released directly onto the T-Jump filament within the TOFMS. A precision leak valve or pulsed valve could be used to control the oxygen flow onto the filament. This could potentially by synced with TOFMS data acquisition and wire heating. The 3D printed collar in Figure 10.2.B can be used with this faceplate to allow for air-sensitive sample measurements identical to the described ASSH system.

Chapter 5 demonstrated that immersion oil can be used to retard oxidation under ambient conditions. The next step in this work would be to incorporate an oxidizer into the immersion oil to create an air-stable energetic composite employing a molecular Al

compound as the fuel. In addition, polymers with more structural integrity can be explored as "capping agents" to prevent oxidation and these systems could be ignited in the MBMS to examine combustion products.

*10.2.3. Expanding the Functionality of MBMS*

Current MBMS studies, as shown in Chapter 9, have only looked at anaerobic combustion of Al/PVDF thin films at 1 atm. The MBMS system is capable of sampling combustion products in aerobic conditions as well, which should be the logical next step in understanding the species produced under real world application conditions. Results shown in Chapter 9 show that hydrocarbon species are produced during anaerobic combustion. In Chapter 7, I show that burn speeds of nAl/PVDF films are much faster in an aerobic environment. The MBMS can aid in determining if the combustion of the released hydrocarbons is the cause for this burn speed enhancement.

With the sampling environment outside of the RTOFMS vacuum chamber, other analytical techniques can be coupled with MBMS data acquisition. One such technique that has been in development in our lab is high speed color camera pyrometry. Figure 10.3 below shows the max, mean, and medium temperature of a 35 nAl wt. % nAl/PVDF film during combustion in air. This coupled experimental setup can help determine if flame temperature is affected by additives in nAl/PVDF films as was proposed in Chapter 9.

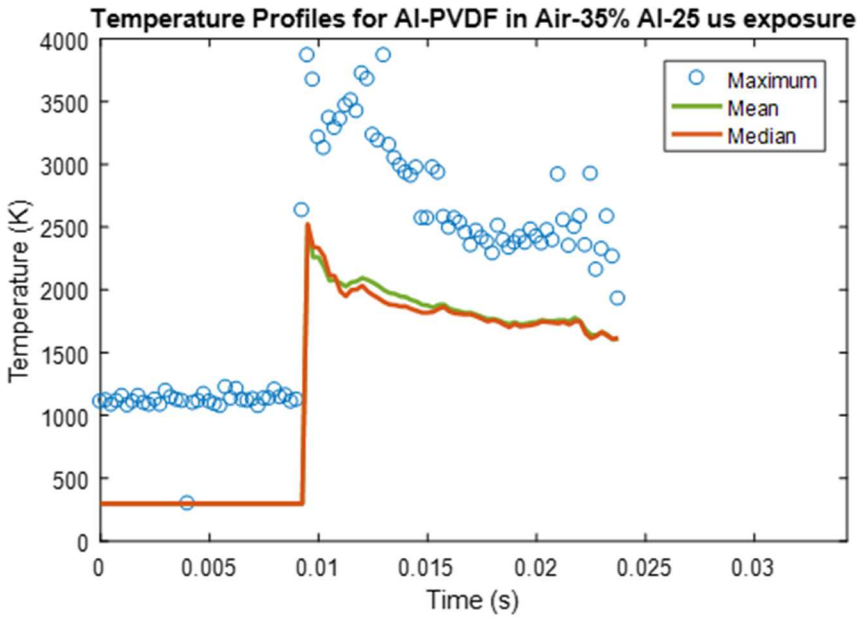


***Figure 10.3.*** *Color camery pyrometry captured simultaneously with MBMS data acquisition for the combustion of a 35 nAl wt. % nAl/PVDF thin film in air.*

# Supplemental Information

*3.S. Supplemental Information: Role of Oxide Shell Crystallization in the Oxidation Mechanisms of Tantalum Nanoparticles and Nanothermites*

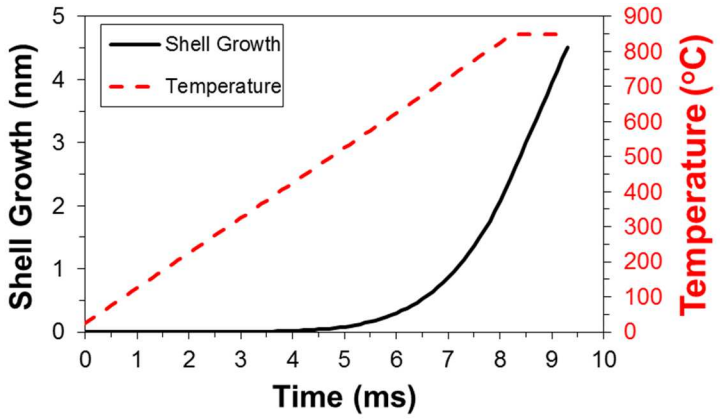


***Figure 3.S1.*** *Theoretical shell growth using the kinetically limited portion of the Deal-Grove model using an oxidation activation energy of 65 kJ/mol during heating at $10^5$ K/s to 850 °C and holding for 1 ms.*

*T-Jump Product Collection for Ta/CuO Nanothermite*

Spherical particles, assumed to be $Ta_2O_5$ and Cu, with sizes ranging from 1 – 10 µm were collected, as seen in Figure 3.S2A. Figure 3.S2B shows a high resolution image of one of the spherical particles. The small aggregates on the surface of the particle are assumed to be caused by the nucleation of gas phase Cu during cooling. Jacob et al., analyzed the post-combustion products for the Al/CuO nanothermite system and observed the same Cu aggregates on the product particles, but in a much higher concentration. This is presumably due to the higher flame temperature of the Al/CuO system in comparison to Ta/CuO.

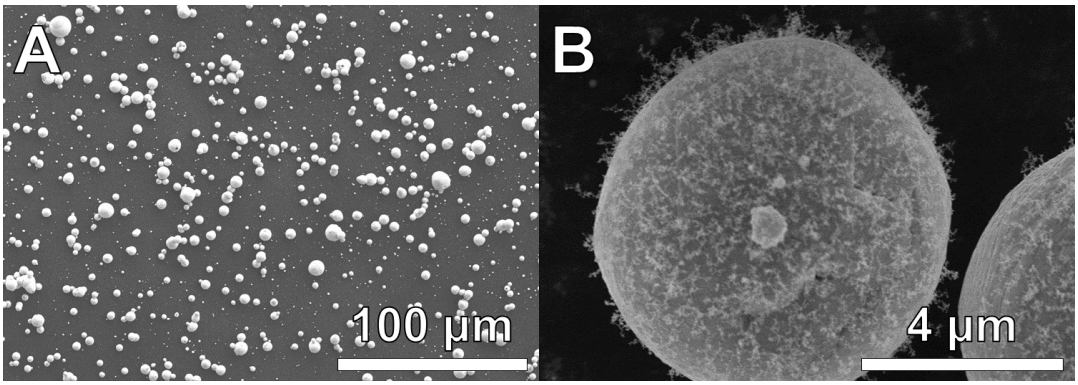


***Figure 3.S2:*** *SEM images of product size distribution (A) and individual post-combustion particle (B) collected from T-Jump ignition of Ta/CuO nanothermite.*

To validate the appearance of nucleated copper on the surface of the $Ta_2O_5$ particles, the theoretical adiabatic flame temperature of the Ta/CuO nanothermite was calculated using Cheetah 6.0 equilibrium code at a constant pressure and found to be 2842 K (Table 3.1). This is very close to the boiling point of copper (2833 K).

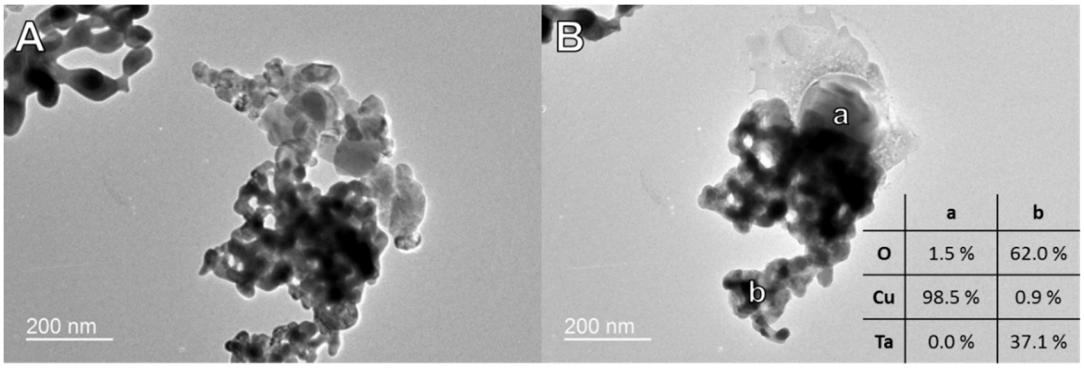


***Figure 3.S3:*** *TEM images of Ta/CuO nanothermite before (A) and after (B) being heated to 1200 °C at a heating rate of $10^5$ K/s and held for 1 ms, and EDS results at two labeled points in the post-heating sample (inset).*

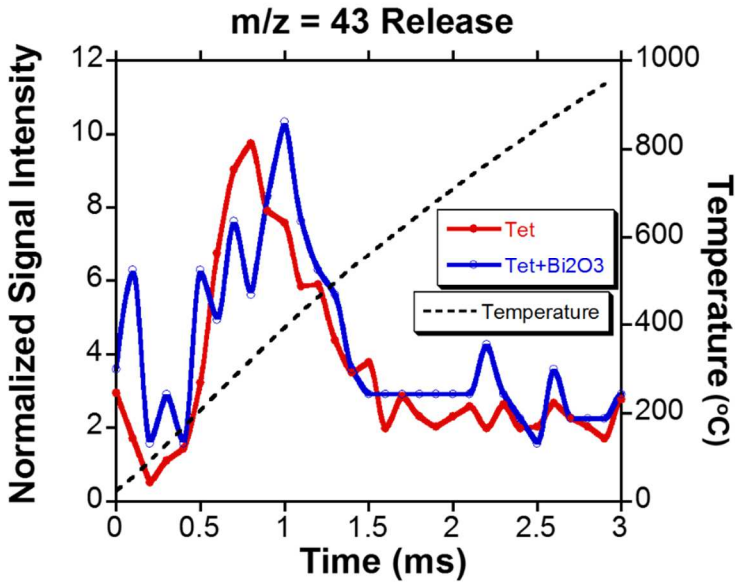


***Figure 4.S1.*** *Species over time plot of m/z=43 for pure Al(I) tetrameric cluster (Tet, red) and Al(I) tetrameric cluster mixed with $Bi_2O_3$ (Tet- $Bi_2O_3$, blue).*

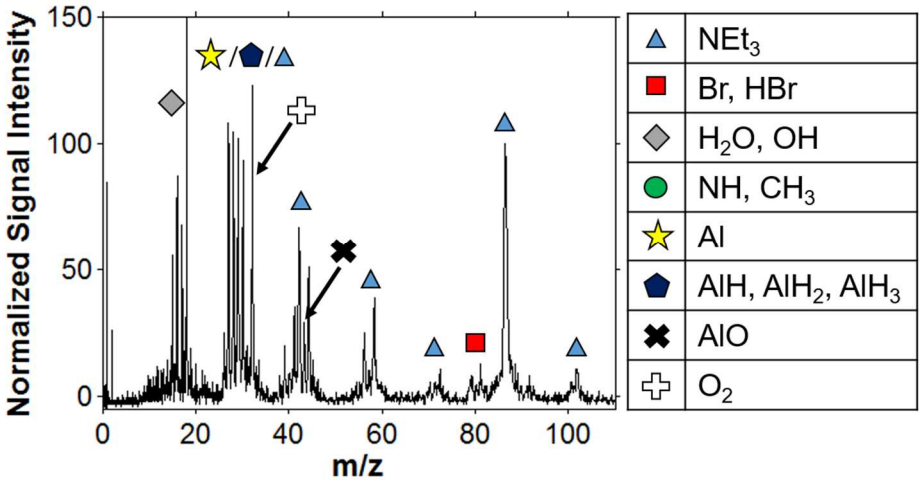


***Figure 4.S2.*** *Normalized MS of $[AlBr(NEt_3)]_4$ mixed with $KIO_4$ (1.2 ms, ~490 °C) heated at ~4 x $10^5$ K/s.*

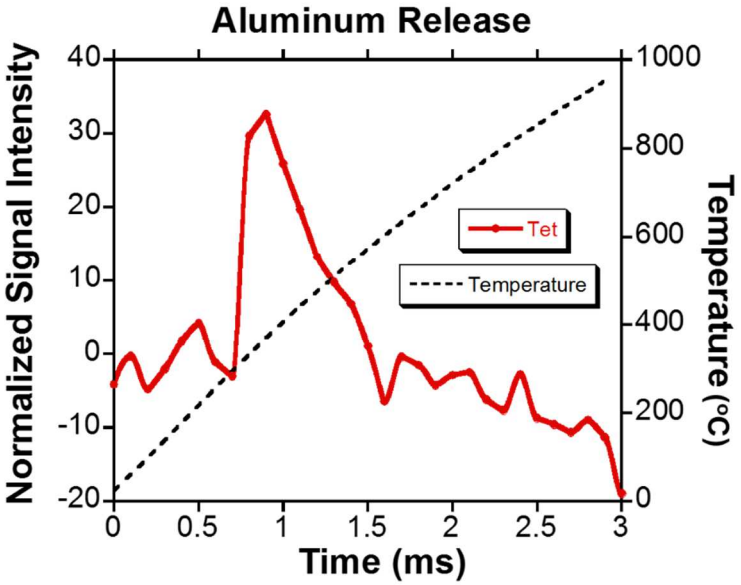


***Figure 4.S3.*** *Plot of aluminum release over time calculated by subtracting the normalized time resolved signal intensities of the m/z = 27 fragment of the oxidized* $[AlBr(NEt_3)]_4$ *from the respective unoxidized* $[AlBr(NEt_3)]_4$ *intensities.*

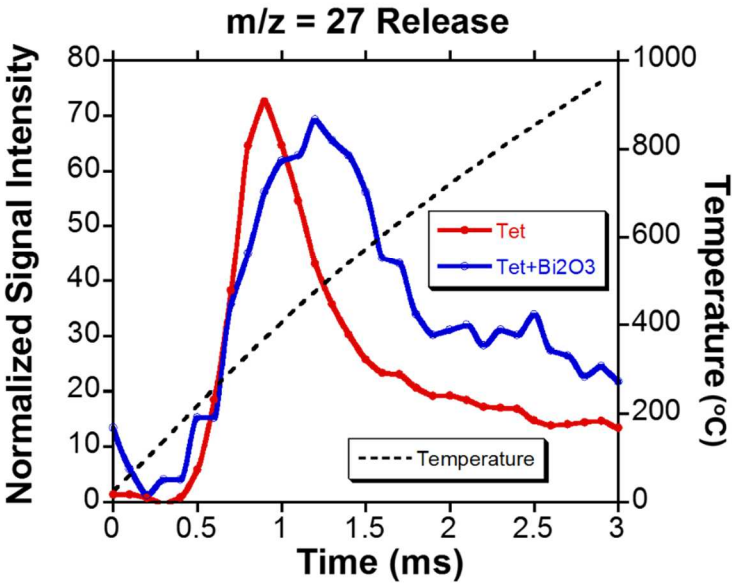


***Figure 4.S4.*** *Species over time plot of m/z=27 for pure Al(I) tetrameric cluster (Tet, red) and Al(I) tetrameric cluster mixed with* $Bi_2O_3$ *(Tet-* $Bi_2O_3$*, blue).*

*6.S. Supplemental Information: High Heating Rate Reaction Dynamics of Al/CuO Nanolaminates by Nanocalorimetry-Coupled Time-of-Flight Mass Spectrometry*

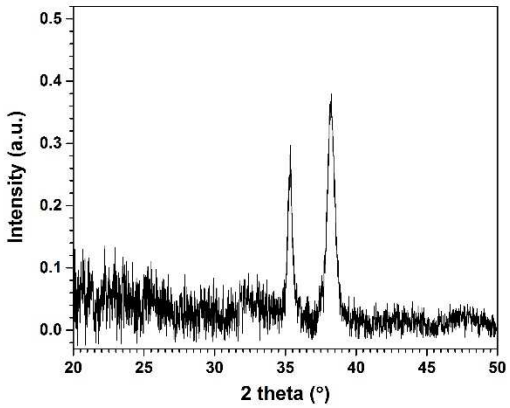


***Figure 6.S1.*** *XRD of pure sputter deposited CuO verifying its composition.*

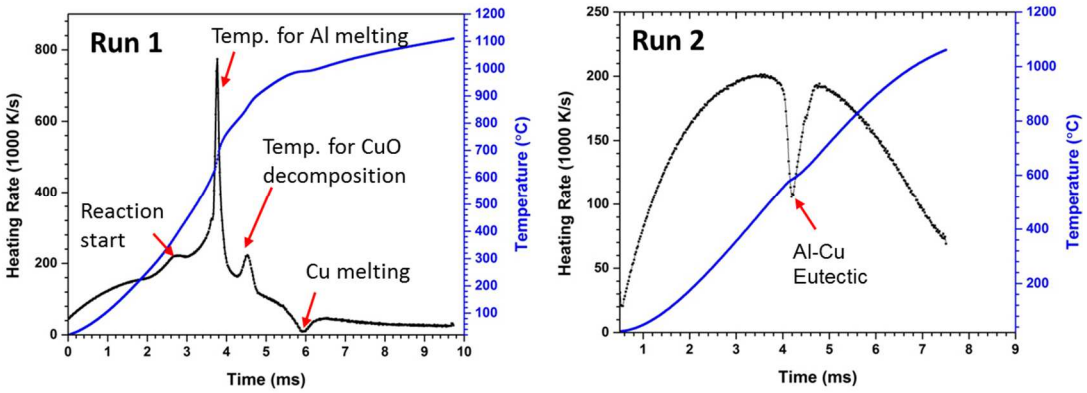


***Figure 6.S2.*** *Heating Rate and Temperature vs Time plots for 80 nm thick, 1 bilayer Al/CuO nanolaminate with an equivalence ratio (ϕ) of 3.*

*8.S. Supplemental Information: Probing the Reaction Mechanism of Aluminum/Polyvinylidene Fluoride Composites*

Figure 8.S1 shows the T-jump ignition in air, argon and vacuum environments. These results show a decrease in reactivity between air and argon and negligible reactivity in the vacuum environment.

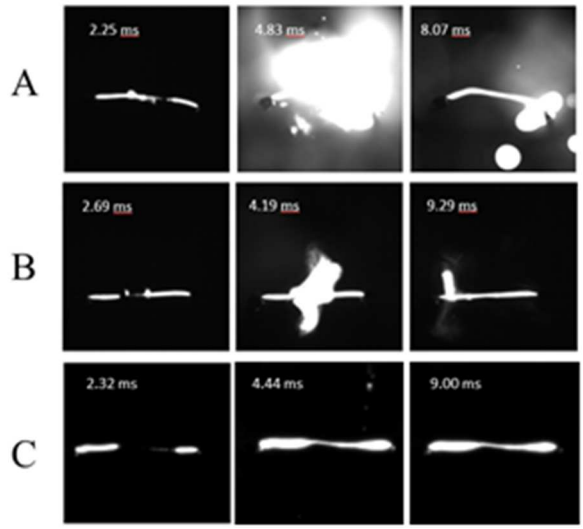


***Figure 8.S41.*** *Rapid heating of platinum wire coated with Al/PVDF in air (A), argon (B), and vacuum (C).*

TGA/DSC performed under 100 mL/min of argon (Ar) flow at 5 $^{o}$C/min of PVDF and $Al_2O_3$/PVDF films is shown below in Figure 8.S2.

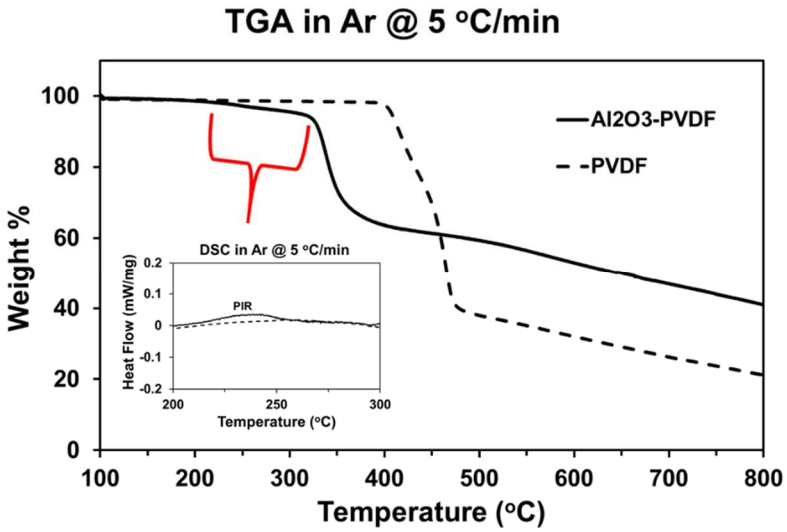


***Figure 8.S2.*** *TGA/DSC data for PVDF and $Al_2O_3$/PVDF films under 100 mL/min Ar flow at a heating rate of 5 °C/min.*

At higher heating rates, PVDF decomposition products react exothermically with the alumina TGA/DSC pans complicating the DSC results as shown in Figure 8.S3. The addition of $Al_2O_3$ speeds up decomposition creating high concentrations of reactive PVDF decomposition products resulting in the small exotherm that follows the decomposition exotherm at ~320 °C (Fig. 8.S3 A). This effect is also observed for pure PVDF at high heating rates (Fig. 8.S3 B). It is also possible that oxygen contamination in the system could be oxidizing the PVDF adding to the exotherm.

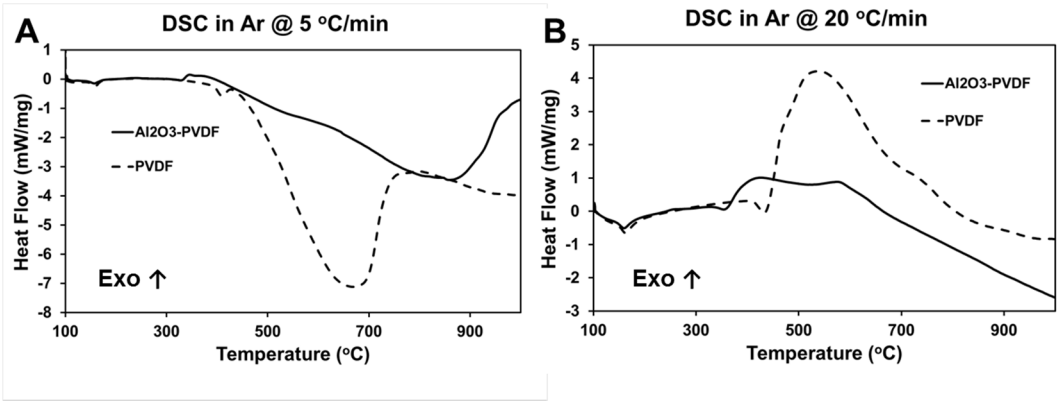


***Figure 8.S3.*** *DSC data for PVDF and $Al_2O_3$/PVDF films under 100 mL/min Ar flow at a heating rates of 5 °C/min (A) and 20 °C/min.*

XRD analysis was performed on electrosprayed PVDF and $Al_2O_3$-PVDF films along with the collected products from heating the $Al_2O_3$-PVDF at 1000 $^oC$ in a tube furnace for 2 hours under argon flow. The $Al_2O_3$-PVDF shows $Al_2O_3$ peaks from the gamma and delta phase, which is what was expected given the $Al_2O_3$ used in the precursor. Pure $Al_2O_3$ was also tested to confirm that there was no change to the $Al_2O_3$ crystalline phase during sample preparation. These results are shown in Figure 8.S4.

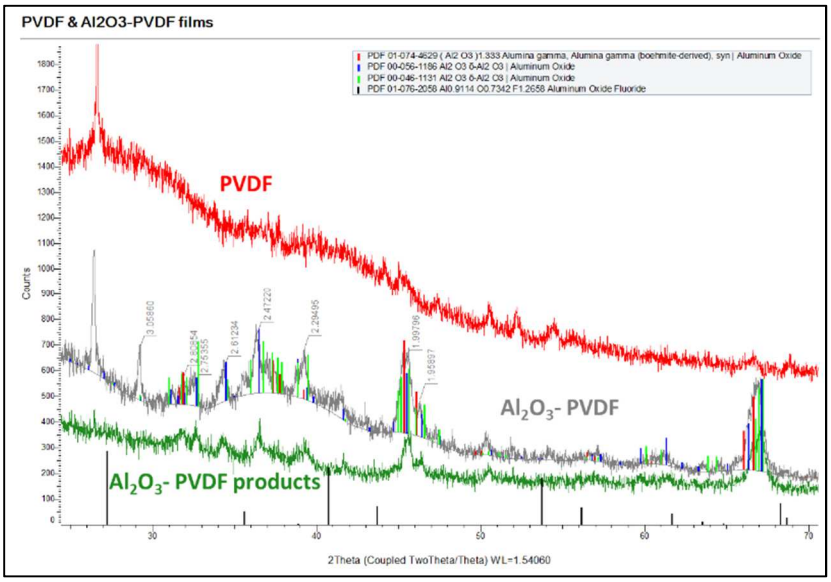


***Figure 8.S4.*** *XRD of PVDF film and $Al_2O_3$/PVDF films before and after heating.*

# Appendix A: Procedure for Protochips High Heating Rate TEM Studies

*Sample Preparation*

1. Add 1-2 mg of solid nanoparticles to empty vial.
2. Fill vial with ethanol and sonicate for ~30 min.
3. Use micropipette to dispense a small aliquot of the suspended particles onto the Protochips heating chip.
4. Label the chip case with the date and sample type for the chip that was coated.

*System Operation*

1. Load heating chip into Protochips TEM sample holder using supplied plastic tweezers in the holder's case.
    a. Compress clasp on mount with one set of tweezers while sliding chip on with others.
    b. When electrical contacts are aligned, let release the compression of tweezers opening the clasp to allow them to close onto the chip.

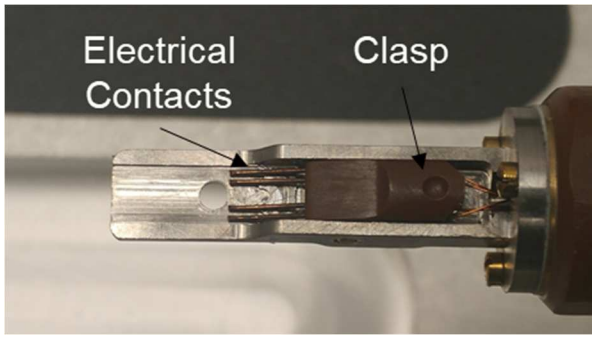


***Figure A-1.*** *Image of chip mount on Protochips TEM holder.*

2. Insert holder into the TEM following standard TEM sample holder installation instructions.

3. Plug in the laptop cart with mounted Protochips power supply into a standard electrical outlet.

4. Open Arduro II software on the desktop.

5. Turn on Protochips power supply on cart.

6. Select chip type as listed on the box the chip was stored in (typically E-AHA21).

7. Open calibration file by finding chip number in calibration folder.

   a. Note: if chip number is not listed in calibration folder on the PC, insert the CD housed in the chip case and copy the calibration files to the PC.

   b. Make sure to use the proper chip number as listed in the case.

   c. Note: chips can have calibration files for both vacuum (default) and air environments. Make sure to load the proper file as denoted by the folder it is in.

8. Plug in TEM holder to the cable coming out of the power supply.

9. Click “Test device”. This ensures the cable is properly connected and electrical contact is being made between the chip and sample holder.

10. Click “Test USB”. This ensures the power supply is functioning properly and can communicate with the PC.

   a. Note: an error will occur if the power supply is not turned on.

11. Click on the “Automatic” tab at the top of the Arduro II window.

12. Click on “Edit Ramp” to edit the heating ramp you would like to apply to the chip.

   a. Note: this is where you enter the max temperature and heating rate.

b. Note: max heating rate is ~$10^6$ K/s

c. Add ramp when completed. A visual representation of the ramp will show up in the bottom window.

13. Add a wait time if you would like to hold the chip at a certain temperature.

a. Type in the time in the box and hit ass. A visual representation of the hold will show up in the bottom window.

14. To return the chip back to room temperature, add a set point of the default temperature listed (25 $^{o}$C).

a. Note: chip will remain at the max temp if this is not added to the method.

15. Click run when method preparation is complete. Chip will instantaneously follow the method.

An image of the software with added method is shown below:

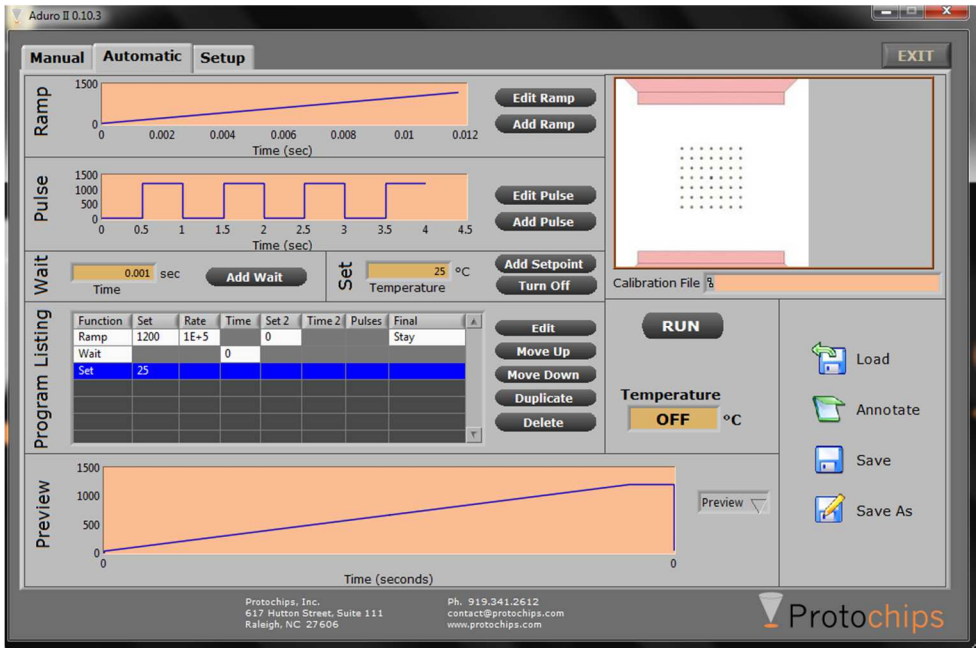


***Figure A-2.*** *Image of Arduro II software.*

# Appendix B: Matlab Scripts for TOFMS Data Processing

```
%Will import spectra data from scope as an average spectrum over every
certain number of segments and will be done within a larger range of
segments. Used for reactions which can be captured within a few
seconds. Contains pauses for better data acquisition. Requires the
averaging math channel and can be used in order to obtain individual
spectra if necessary. Allows you to select segment range of interest
from total segments acquired.


prompt='Enter # of spectra to average\n';
AvgNum = input(prompt);
prompt='Enter start segment #\n';
startSeg = input(prompt);
prompt='Enter stop segment #\n';
stopSeg = input(prompt);
samplingRate = 1000.0; %sampling rate in Hz
prompt='Enter sample name\n';
name=input(prompt,'s');


%% MAKE CONNECTION AND READ DATA FROM SCOPE %%
DSO = actxserver('LeCroy.XStreamDSO.1', '127.0.0.1');

% Read back instrument ID
get(DSO.Item('InstrumentID'),'Value')

%% Setup objects
acq = DSO.Object.Item('Acquisition');
c1 = acq.Object.Item('C1');
mat = DSO.Object.Item('Math');
sav = DSO.Object.Item('SaveRecall');
savWav = sav.Object.Item('Waveform');
f1 = mat.Object.Item('F1');
f3 = mat.Object.Item('F3');
f4 = mat.Object.Item('F4');
f4_zoom = f4.Object.Item('Zoom');
f1_op = f1.Object.Item('Operator1Setup');

%% Get sequence mode settings and set zoom to AvgNum
set(f4_zoom,'NumSelectedSegments',AvgNum);
segNum=get(acq.Object.Item('Horizontal').Item('AcquiredSegments'),'Valu
e');

%% Save avg gate pulse
set(f1_op,'Sweeps',10);
pause(.25)
set(f1_op,'Sweeps',3500);
pause(.25)
set(savWav,'TraceTitle',name);
set(savWav,'SaveSource','F1');
invoke(savWav,'DoSave');
```

```
%% First avg acquisition
invoke(mat,'ClearSweeps');
pause(.25)
set(f4_zoom,'SelectedSegment',1);
pause(.25)
set(savWav,'SaveSource','F3');
invoke(savWav,'DoSave');

%% Looped acquisition/save
for i=1:(((stopSeg-startSeg)/AvgNum)-1)
    pause(.25)
    invoke(mat,'ClearSweeps');
    pause(.25)
    set(f4_zoom,'SelectedSegment',startSeg+(i*AvgNum));
    pause(.25)
    set(savWav,'SaveSource','F3');
    invoke(savWav,'DoSave');
end

%% Calculate spec times
specTime = zeros(int64((stopSeg-startSeg)/AvgNum),1);
specTime(1,1) = (AvgNum/2)/samplingRate; %Time of first average
spectrum
for k=2:length(specTime)
   specTime(k,1)= specTime(k-1)+(AvgNum/samplingRate);
end

%% Process data files and combine
specNum=0;
%% Import F1
        filename = ['Z:\Rehwoldt\MBMS
data\Calibrations\Krypton\F1',name,'00000.txt'];
        delimiter = ',';
        startRow = 6;
        formatSpec = '%f%f%*s%*s%[^\n\r]';
        fileID = fopen(filename,'r');
        dataArray = textscan(fileID, formatSpec, 'Delimiter',
delimiter, 'EmptyValue' ,NaN,'HeaderLines' ,startRow-1,
'ReturnOnError', false);
        fclose(fileID);
        time(:,1) = dataArray{:, 1};
        pulse(:,1) = dataArray{:, 2};
        clearvars filename delimiter startRow formatSpec fileID
dataArray ans;

        intensity = zeros(length(time),length(specTime));
for i=1:(length(specTime)-1)
    if i<=10
        %% Import F3
        pause(.25)
        filename = ['Z:\Rehwoldt\MBMS
data\Calibrations\Krypton\F3',name,'0000',num2str(specNum),'.txt'];
        delimiter = ',';
        startRow = 6;
        formatSpec = '%*s%f%*s%*s%[^\n\r]';
        fileID = fopen(filename,'r');
```

```
        dataArray = textscan(fileID, formatSpec, 'Delimiter',
delimiter, 'EmptyValue' ,NaN,'HeaderLines' ,startRow-1,
'ReturnOnError', false, 'EndOfLine', '\r\n');
        fclose(fileID);
        intensityTemp(:,1) = dataArray{:, 1};

intensity(1:length(intensity),i)=intensityTemp(1:length(intensity),1);
        clearvars filename delimiter startRow formatSpec fileID
dataArray ans;
    end
    if i>10 && i<=100
        %% Import F3
        filename = ['Z:\Rehwoldt\MBMS
data\Calibrations\Krypton\F3',name,'000',num2str(specNum),'.txt'];
        delimiter = ',';
        startRow = 6;
        formatSpec = '%*s%f%*s%*s%[^\n\r]';
        fileID = fopen(filename,'r');
        dataArray = textscan(fileID, formatSpec, 'Delimiter',
delimiter, 'EmptyValue' ,NaN,'HeaderLines' ,startRow-1,
'ReturnOnError', false);
        fclose(fileID);
        intensityTemp(:,1) = dataArray{:, 1};

intensity(1:length(intensity),i)=intensityTemp(1:length(intensity),1);
        clearvars filename delimiter startRow formatSpec fileID
dataArray ans;
    end
    if i>100
        %% Import F3
        filename = ['Z:\Rehwoldt\MBMS
data\Calibrations\Krypton\F3',name,'00',num2str(specNum),'.txt'];
        delimiter = ',';
        startRow = 6;
        formatSpec = '%*s%f%*s%*s%[^\n\r]';
        fileID = fopen(filename,'r');
        dataArray = textscan(fileID, formatSpec, 'Delimiter',
delimiter, 'EmptyValue' ,NaN,'HeaderLines' ,startRow-1,
'ReturnOnError', false);
        fclose(fileID);
        intensityTemp(:,1) = dataArray{:, 1};

intensity(1:length(intensity),i)=intensityTemp(1:length(intensity),1);
        clearvars filename delimiter startRow formatSpec fileID
dataArray ans;
    end
    clearvars intensityTemp
     specNum = i;
end
%% Convert to m/z
startTimeIndex = 0;
endTimeIndex = 0;
loopStart = 1;
conv=5.5890e+10;
ts = 3.2739e-07;
dt = abs(time(2,1)-time(1,1));
```

```
    for i=1:length(time)
        if pulse(i) > 0.5 && startTimeIndex == 0
            startTimeIndex = i;
        end
    end

    for i=startTimeIndex:length(time)
        if pulse(i) < 0.5 && endTimeIndex == 0
            endTimeIndex = i;
        end
    end

    for j=1:length(specTime)
        ToF(1,j) = 0;
        spectra(1,j) = intensity(endTimeIndex,j);
        timeCount=2;
        for i=endTimeIndex:length(intensity)
            spectra(timeCount,j) = intensity(i,j);
            ToF(timeCount,j) = (timeCount-1)*dt;
            timeCount = timeCount +1;
        end

        mass(:,j)=conv.*((ToF(:,j)-ts).^2);
    end


figure()
plot(mass(:,1),spectra(:,:))

save([name,'-
MassSpec.mat'],'specTime','time','pulse','intensity','mass','spectra','
startSeg','stopSeg','AvgNum')
clear;
```

# Appendix C: Detailed ASSH Experimental Procedure

The image below depicts each of the components used to assemble the ASSH:

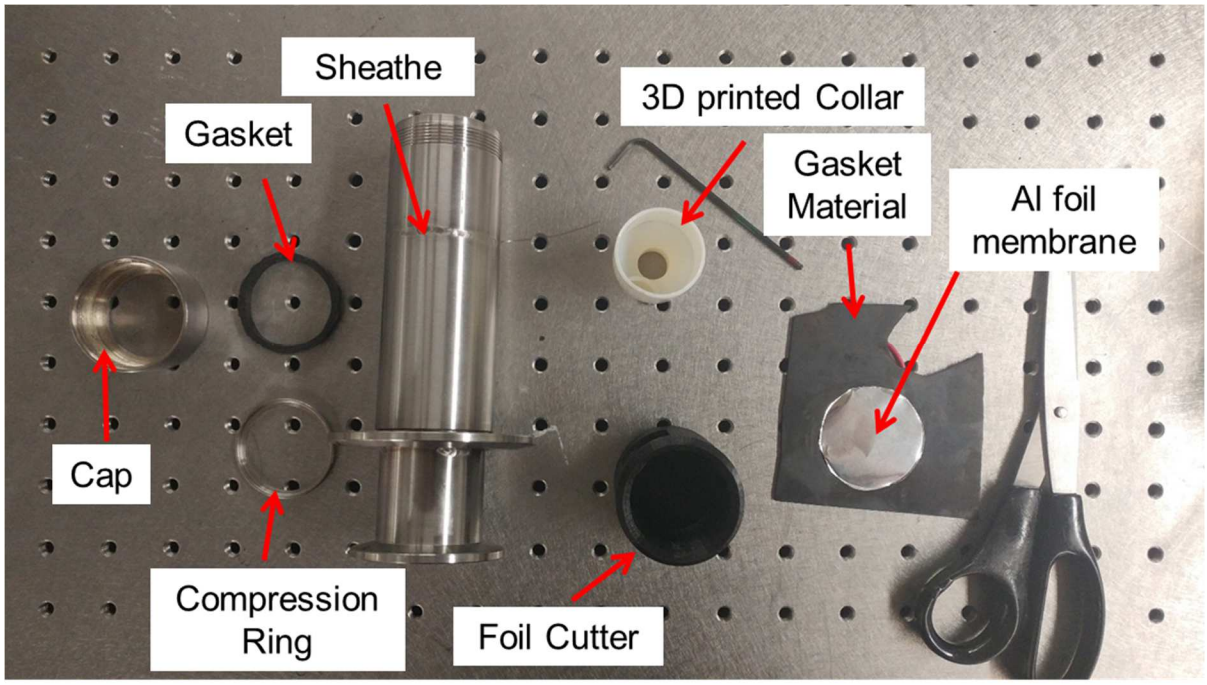


***Figure C-1.*** *ASSH components*

*Assembling the ASSH*

1. Solder Pt or Ir wires to the leads of the standard T-Jump probe as typically done for T-Jump TOFMS experiments.

2. Use the foil cutter to cut out a circular piece of Al foil from a roll of "heavy duty" Al foil.

   a. Press the foil cutter down on the gasket material with the Al foil in between so that the cutter can compress the gasket to punch out the circular piece of foil.

   b. You may need to use the scissors to trim the edges around the impression left by the foul cutter.

3. Insert the T-Jump probe into the sheathe and secure with clamp.

4. Extend the T-Jump probe so that the face of the flange is visible.

5. Press the 3D printed collar onto the electrical feedthrough on the face of the T-Jump probe.

a. Secure by tightening set screw.

b. Note: do not overtighten as you are screwing a metal screw into plastic and can easily strip the tapped hole.

c. Once collar is secured, fully retract the T-Jump probe.

6. Insert Al foil membrane into cap and press down with compression ring.

a. Compression ring is used to ensure even pressure around the outside rim of the foil to make for a better seal. It is removed after use.

7. Insert circular gasket into cap on top of the Al foil membrane and press down with compression ring as described above.

8. Remove compression ring and tighten cap onto sheathe.

*Experimental Procedure*

1. Seal the T-Jump probe port on the TOFMS with a blank flange and use the roughing pump to keep the roughing chamber at a low pressure. Cycle the system with nitrogen at least once while ASSH is being inserted into the glove box.

2. Cycle full ASSH, micropipette, and pipette tips wrapped in Al foil into glove box.

a. Make sure to remove cap of ASSH prior to cycling into the glove box.

b. The large port requires 90 minutes to cycle in the holder.

3. Once inside the glove box, use the pipette to dropper sample onto the T-Jump wires.

4. After the wires are coated, screw on the cap tightly to entrap the inert environment of the glove box within the ASSH.

5. Remove ASSH from glove box and immediately bring to TOFMS system.

6. Fill the roughing chamber with a positive pressure of nitrogen (argon interferes with the MS results if there is too much in the system)

7. Open the exhaust valve to allow nitrogen to flow through the sampling region.

8. Close the exhaust valve while simultaneously removing the blank flange on the T-Jump probe port.

9. Insert ASSH into T-Jump probe port and turn off nitrogen flow once clamp is fastened.

10. Puncture foil by extending the probe ~1" into the roughing chamber.

    a. Note: this is extremely important as the foil will get sucked into the system if it is not punctured prior to pumping down the roughing chamber.

11. Open gate valve to roughing port and proceed with standard T-Jump TOFMS operation.

# Appendix D: Nanocalorimetry Heat Capacity and Enthalpy Details

The heat of Enthalpy from an aluminum film was determined to demonstrate the measurement capability of nanocalorimetry to quantify changes in enthalpies. Aluminum was deposited over the nanocalorimeter sensor by e-beam evaporation using a custom designed shadow mask. The base pressure during deposition is less than 3 x $10^{-6}$ Torr and the deposition rate is 0.1 nm/s. A 10 nm thick layer of alumina was deposited before the aluminum sample as a barrier layer to prevent reactions between the aluminum sample and silicon nitride membrane.

The enthalpy of fusion is obained from the area under the heat capacity curve. The heat capacity ($C_p$) of a nanocalorimeter sensor, applied power (P), heat loss (WL) and heating rate (dT/dt) are related by the Equation 1.

$$C_p \frac{dT}{dt} = P - WL \qquad \text{(D-1)}$$

The key factors that must be addressed are accurate temperature and sample mass measurements, appropriate calculation of applied power and heat losses during an experiment. A fast temperature calibration procedure has been described previously that relates nanocalorimeter resistance to temperature. Applied voltage and current are measured during an experiment and converted to resistance and power. The sample thickness can be determnined by a variety of means. For this example, it was measured using a Bruker Dektak XT Profilometer. The thickness value for the sample below was 126 nm (Bruker specifies vertical resolution as 0.1 nm); the sample mass is 476 ng given the measured area of the film (3.5 mm x 0.4 mm) and bulk density (2.7 g $cm^{-3}$).

$$WL = A + C_C(T - 298) + C_R(T^4 - 298^4) \qquad \text{(D-2)}$$

In vacuum, the heat loss is dominated by conduction and radiation, and it is a function of temperature as in Equation D-2, where WL is the heat loss, T is the chip

temperature in K; A, $C_c$, and $C_R$ are fit parameters. Heat loss is rate independent so that the heat loss can be quantified with multiple baseline measurements at varying rates. To obtain these fit parameters, the empty nanocalorimeter sensors are measured at different heating rates and heat losses calculated following a method published previously.[22] Applied power and heat loss data are plotted as a function of temperature shown in Figure D-1.

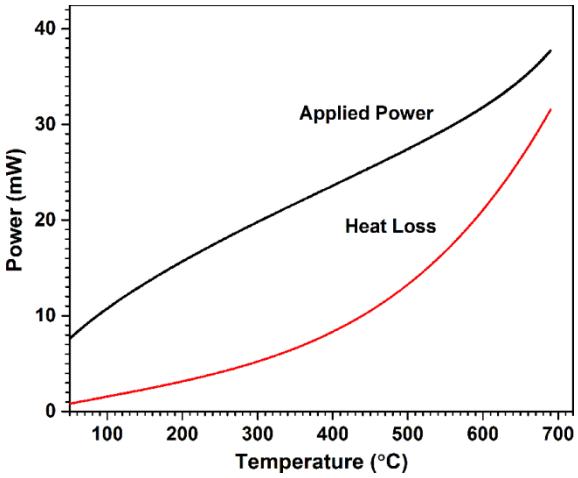


***Figure D-1.*** *Applied power and calculated heat loss for the nanocalorimeter sensor (calculated for operation in vacuum).*

The heat capacity of the nanocalorimeter was calculated using Equation D-1 as shown in Figure D-2(a). The heat capacity consists of three parts as shown in Equation D-3. Figure D-2(a) shows the heat capacity for the bare sensor, sensor with alumina and sensor with alumina and aluminum (the inserted window shows the details). Subtracting the heat capacity of the bare chip and alumina from the total heat capacity gives the heat capacity of aluminum, as shown in Figure D-2(b).

$$C_P^{Sensor} = C_P^{sample} + C_P^{bare\ sensor} + C_P^{Alumina} \qquad \text{(D-3)}$$

The area under the heat capacity curve gives the total enthalpy of fusion of aluminum film. The heat absorbed during melting was measured as 0.173 mJ and the calculated molar enthalpy for melting was 9.81 kJ $mol^{-1}$, which is slightly lower than the

reported molar enthalpy for melting of pure bulk Al (10.58 ± 0.15 kJ $mol^{-1}$)[23]. This difference may be associated with experimental uncertainty, and a difference in the density of e-beam deposited Al thin film compared to the bulk.

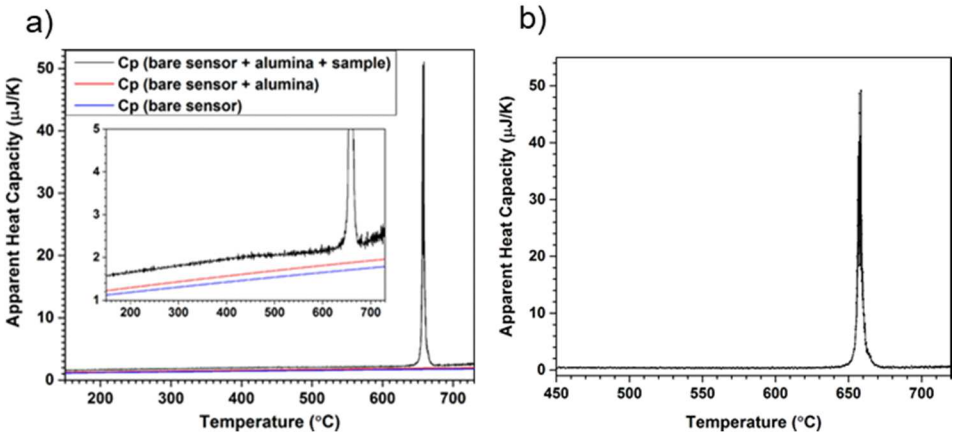


***Figure D-2.*** *(a) Apparent heat capacity of the sample and nanocalorimeter sensor during Al melting. An insert window shows greater detail. (b) Net apparent heat capacity of the Al film after subtracting baseline contributions.*

# Appendix E: Detailed MBMS Construction Guide

*Block Diagram of MBMS Setup*

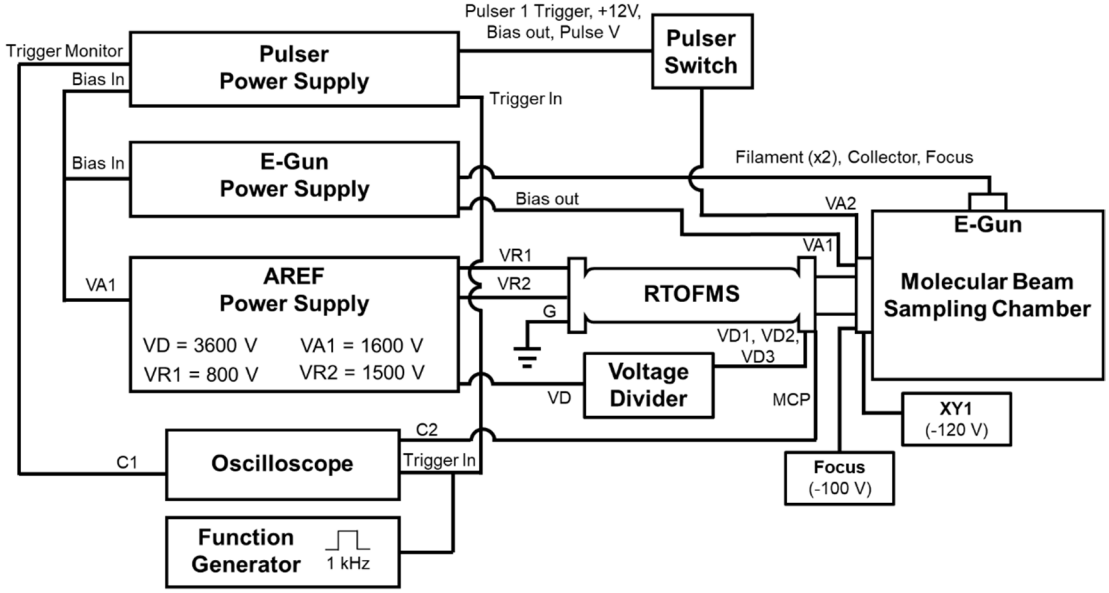


***Figure E-1.*** *Block diagram of MBMS with typically set parameters.*

*Film Burning Procedure*

1. Clean quartz reactor tube with acetone and sonicate to ensure sampling orifice is clear.

2. Using 1-2” long nichrome wires, twist and make into a single braid.

3. Wrap nichrome wire around copper leads so there is no more than 5-6 mm of separation between the leads and then solder on nichrome wires.

4. Sandwich film (2-5 mm by 2-6+ mm) in between the braided nichrome wire.

5. Test conductivity with a multimeter.

6. Insert flow tube with attached leads into the quartz reactor tube.

7. Optional: press leads to the “valley” of the tube to mitigate clogging during combustion.

8. Insert assembled reactor into XYZ manipulator attached to the sampling chamber.

9. Ensure tube is as close as possible to skimmer cone before tightening.

a. Note: you can check this using a camera with the mirror inserted into the base of the sampling chamber.

10. After sealing the chamber, turn on the mechanical bump attaching to the sampling region.

a. The pressure in this region should reach ~1 Torr.

11. Close valve to mechanical pump and open large gate valve to turbo pump.

a. The pressure in this region should now reach ~2-6 mTorr.

b. Tube may get sucked into the chamber during this process. You may need to re-align so that the tube is not touching the skimmer cone.

12. Once pumps are engaged, system triggering can commence and the small gate valve behind the skimmer cone can be opened forming the molecular beam.

13. Adjust tube position by hand to achieve maxiumum MS signal intensity

a. At 50 mV/div, signal should fill at least half of the window.

b. Alignment can be done with reactor flow open or under ambient conditions.

14. Fix tube in place with ring stand and clamp.

15. While preparing the experiment after aligning, take precautions to not disturb the reactor tube. It is best to re-check alignment prior to triggering the system.

# List of References

Format: [A-B]. A=Chapter number, and B=Reference number in each chapter.


[1-1] J. Akhavan, The Chemistry of Explosives, 2 ed., The Royal Society of Chemistry2004.
[1-2] T. Davis, The Chemistry of Powder and Explosives, 1943.
[1-3] J. Agrawal, High Energy Materials: Propellants, Explosives and Pyrotechnics, Wiley-VCH2010.
[1-4] R.A. Yetter, G.A. Risha, S.F. Son, Metal particle combustion and nanotechnology, Proceedings of the Combustion Institute 32 (2009) 1819-1838.
[1-5] E.L. Dreizin, Metal-based reactive nanomaterials, Progress in Energy and Combustion Science 35 (2009) 141-167.
[1-6] G.P. Sutton, O. Biblarz, Rocket Propulsion Elements, 8th ed., John Wiley & Sons, Inc., Hoboken, NJ, 2010.
[1-7] L. Zhou, N. Piekiel, S. Chowdhury, M.R. Zachariah, T-Jump/time-of-flight mass spectrometry for time-resolved analysis of energetic materials, Rapid Commun. Mass Spectrom. 23 (2009) 194-202.
[1-8] A.S. Rogachev, A.S. Mukasyan, Combustion of heterogeneous nanostructural systems (Review), Combustion Explosion and Shock Waves 46 (2010) 243-266.
[1-9] C.E. Aumann, G.L. Skofronick, J.A. Martin, Oxidation Behavior Of Aluminum Nanopowders, Journal of Vacuum Science & Technology B 13 (1995) 1178-1183.
[1-10] B.S. Bockmon, M.L. Pantoya, S.F. Son, B.W. Asay, J.T. Mang, Combustion velocities and propagation mechanisms of metastable interstitial composites, J. Appl. Phys. 98 (2005) 064903/064901-064903/064907.
[1-11] B.W. Asay, S.E. Son, J.R. Busse, D.M. Oschwald, Ignition characteristics of metastable intermolecular composites, Propellants Explosives Pyrotechnics 29 (2004) 216-219.
[1-12] G. Jian, J. Feng, R.J. Jacob, G.C. Egan, M.R. Zachariah, Super-reactive Nanoenergetic Gas Generators Based on Periodate Salts, Angew. Chem., Int. Ed. 52 (2013) 9743-9746.
[1-13] W. Zhou, J.B. DeLisio, X. Li, L. Liu, M.R. Zachariah, Persulfate salt as an oxidizer for biocidal energetic nano-thermites, Journal of Materials Chemistry A 3 (2015) 11838-11846.
[1-14] W. Zhou, J.B. DeLisio, X. Wang, M.R. Zachariah, Reaction mechanisms of potassium oxysalts based energetic composites, Combustion and Flame 177 (2017) 1-9.
[1-15] K.T. Sullivan, N.W. Piekiel, S. Chowdhury, C. Wu, M.R. Zachariah, C.E. Johnson, Ignition and Combustion Characteristics of Nanoscale Al/AgIO3: A Potential Energetic Biocidal System, Combust. Sci. Technol. 183 (2011) 285-302.
[1-16] H. Wang, G. Jian, W. Zhou, J.B. DeLisio, V.T. Lee, M.R. Zachariah, Metal Iodate-Based Energetic Composites and Their Combustion and Biocidal Performance, Acs Applied Materials & Interfaces 7 (2015) 17363-17370.
[1-17] E.-C. Koch, Metal-fluorocarbon-pyrolants: III. Development and application of magnesium/teflon/viton (MTV), Propellants, Explos., Pyrotech. 27 (2002) 262-266.

[1-18] D.T. Osborne, M.L. Pantoya, Effect of al particle size on the thermal degradation of Al/Teflon mixtures, Combustion Science and Technology 179 (2007) 1467-1480.
[1-19] M.L. Pantoya, S.W. Dean, The influence of alumina passivation on nano-Al/Teflon reactions, Thermochimica Acta 493 (2009) 109-110.
[1-20] N. Kubota, C. Serizawa, Combustion process of magnesium/polytetrafluoroethylene pyrotechnics, Propellants, Explos., Pyrotech. 12 (1987) 145-148.
[1-21] N.S. Cohen, R.W. Fleming, R.L. Derr, Role Of Binders In Solid-Propellant Combustion, Aiaa Journal 12 (1974) 212-218.
[1-22] G. Jian, S. Chowdhury, K. Sullivan, M.R. Zachariah, Nanothermite reactions: Is gas phase oxygen generation from the oxygen carrier an essential prerequisite to ignition?, Combust. Flame 160 (2013) 432-437.
[1-23] V.I. Levitas, Burn time of aluminum nanoparticles: Strong effect of the heating rate and melt-dispersion mechanism, Combustion and Flame 156 (2009) 543-546.
[1-24] K.T. Sullivan, N.W. Piekiel, C. Wu, S. Chowdhury, S.T. Kelly, T.C. Hufnagel, K. Fezzaa, M.R. Zachariah, Reactive sintering: An important component in the combustion of nanocomposite thermites, Combust. Flame 159 (2012) 2-15.
[1-25] G.C. Egan, K.T. Sullivan, T. LaGrange, B.W. Reed, M.R. Zachariah, In situ imaging of ultra-fast loss of nanostructure in nanoparticle aggregates, Journal of Applied Physics 115 (2014).
[1-26] G.C. Egan, T. LaGrange, M.R. Zachariah, Time-Resolved Nanosecond Imaging of Nanoscale Condensed Phase Reaction, Journal of Physical Chemistry C 119 (2015) 2792-2797.
[1-27] E.L. Dreizin, Phase changes in metal combustion, Progress in Energy and Combustion Science 26 (2000) 57-78.
[1-28] B.J. Henz, T. Hawa, M.R. Zachariah, On the role of built-in electric fields on the ignition of oxide coated nanoaluminum: Ion mobility versus Fickian diffusion, Journal of Applied Physics 107 (2010).
[1-29] V.I. Levitas, B.W. Asay, S.F. Son, M. Pantoya, Melt dispersion mechanism for fast reaction of nanothermites, Applied Physics Letters 89 (2006).
[1-30] M.A. Hobosyan, K.G. Kirakosyan, S.L. Kharatyan, K.S. Martirosyan, PTFE-Al2O3 reactive interaction at high heating rates, J. Therm. Anal. Calorim. 119 (2015) 245-251.
[1-31] O. Mulamba, M. Pantoya, Exothermic surface reactions in alumina-aluminum shell-core nanoparticles with iodine oxide decomposition fragments, J. Nanopart. Res. 16 (2014) 2310/2311-2310/2319, 2319 pp.
[1-32] J. McCollum, M.L. Pantoya, S.T. Iacono, Activating Aluminum Reactivity with Fluoropolymer Coatings for Improved Energetic Composite Combustion, Acs Applied Materials & Interfaces 7 (2015) 18742-18749.
[1-33] M. Tacke, H. Schnoeckel, Metastable aluminum chloride, AlCl, as a solid and in solution, Inorg. Chem. 28 (1989) 2895-2896.
[1-34] J.M. Lightstone, C. Stoltz, R.M. Wilson, J. Horn, J. Hooper, D. Mayo, B. Eichhorn, K. Bowen, M.G. White. 2012. Development Of Metal Cluster-Based Energetic Materials At Nswc-Ihd. In: editor^editors. AIP Conference Proceedings. 7th Biennial Conference of the American-Physical-Society-Topical-Group on Shock Compression of Condensed Matter; Jun 26-Jul 01 2011; Chicago, IL: Amer Inst Physics.

[1-35] C. Michaelsen, K. Barmak, T.P. Weihs, Investigating the thermodynamics and kinetics of thin film reactions by differential scanning calorimetry, Journal of Physics D-Applied Physics 30 (1997) 3167-3186.
[1-36] A.J. Gavens, D. Van Heerden, A.B. Mann, M.E. Reiss, T.P. Weihs, Effect of intermixing on self-propagating exothermic reactions in Al/Ni nanolaminate foils, Journal of Applied Physics 87 (2000) 1255-1263.
[1-37] C. Rossi, K. Zhang, D. Esteve, P. Alphonse, P. Tailhades, C. Vahlas, Nanoenergetic materials for MEMS: a review, J. Microelectromech. Syst. 16 (2007) 919-931.
[1-38] M. Bahrami, G. Taton, V. Conedera, L. Salvagnac, C. Tenailleau, P. Alphonse, C. Rossi, Magnetron Sputtered Al-CuO Nanolaminates: Effect of Stoichiometry and Layers Thickness on Energy Release and Burning Rate, Propellants Explosives Pyrotechnics 39 (2014) 365-373.
[1-39] M. Petrantoni, C. Rossi, L. Salvagnac, V. Conedera, A. Esteve, C. Tenailleau, P. Alphonse, Y.J. Chabal, Multilayered Al/CuO thermite formation by reactive magnetron sputtering: Nano versus micro, Journal of Applied Physics 108 (2010).
[1-40] K.T. Sullivan, C. Zhu, E.B. Duoss, A.E. Gash, D.B. Kolesky, J.D. Kuntz, J.A. Lewis, C.M. Spadaccini, Controlling Material Reactivity Using Architecture, Advanced Materials 28 (2016) 1934-+.
[1-41] N.W. Piekiel, W.A. Churaman, C.J. Morris, L.J. Currano, Combustion and material characterization of porous silicon nanoenergetics, IEEE Int. Conf. Micro Electro Mech. Syst., 26th (2013) 449-452.
[1-42] N.W. Piekiel, C.J. Morris, L.J. Currano, D.M. Lunking, B. Isaacson, W.A. Churaman, Enhancement of on-chip combustion via nanoporous silicon microchannels, Combust. Flame 161 (2014) 1417-1424.
[1-43] N.W. Piekiel, C.J. Morris, L.J. Currano, D.M. Lunking, B. Isaacson, W.A. Churaman, Enhancement of on-chip combustion via nanoporous silicon microchannels, Combustion and Flame 161 (2014) 1417-1424.
[2-1] V.I. Levitas, Burn time of aluminum nanoparticles: Strong effect of the heating rate and melt-dispersion mechanism, Combustion and Flame 156 (2009) 543-546.
[2-2] M.L. Pantoya, J.J. Granier, The effect of slow heating rates on the reaction mechanisms of nano and micron composite thermite reactions, Journal of Thermal Analysis and Calorimetry 85 (2006) 37-43.
[2-3] K.T. Sullivan, N.W. Piekiel, C. Wu, S. Chowdhury, S.T. Kelly, T.C. Hufnagel, K. Fezzaa, M.R. Zachariah, Reactive sintering: An important component in the combustion of nanocomposite thermites, Combust. Flame 159 (2012) 2-15.
[2-4] M.S.V. Dusen, Platinum-Resistance Thermometry At Low Temperatures1, Journal of the American Chemical Society 47 (1925) 326-332.
[2-5] L. Zhou, N. Piekiel, S. Chowdhury, M.R. Zachariah, T-Jump/time-of-flight mass spectrometry for time-resolved analysis of energetic materials, Rapid Commun. Mass Spectrom. 23 (2009) 194-202.
[2-6] L. Zhou, N. Piekiel, S. Chowdhury, M.R. Zachariah, T-Jump/Time-of-Flight Mass Spectrometry for Time Resolved Analysis of Energetic Materials, Rapid Communications in Mass Spectrometry 23 (2009) 194-202.
[2-7] L. Zhou, N. Piekiel, S. Chowdhury, D. Lee, M.R. Zachariah, Transient ion ejection during nanocomposite thermite reactions, Journal of Applied Physics 106 (2009) 083306.

[2-8] L. Zhou, N. Piekiel, S. Chowdhury, M.R. Zachariah, Time-Resolved Mass Spectrometry of the Exothermic Reaction between Nanoaluminum and Metal Oxides: The Role of Oxygen Release, Journal of Physical Chemistry C 114 (2010) 14269-14275.
[2-9] N.W. Piekiel, L. Zhou, K.T. Sullivan, S. Chowdhury, G.C. Egan, M.R. Zachariah, Initiation And Reaction In Al/Bi2o3 Nanothermites: Evidence For The Predominance Of Condensed Phase Chemistry, Combustion Science and Technology 186 (2014) 1209-1224.
[2-10] G. Jian, L. Zhou, N.W. Piekiel, M.R. Zachariah, Probing oxygen release kinetics of nanosized metal oxides by temperature-jump time of flight mass spectrometry, Chem. Phys. Processes Combust. (2011) 126-131.
[2-11] N. Piekiel, M.R. Zachariah, Decomposition of Aminotetrazole Based Energetic Materials under High Heating Rate Conditions, Journal of Physical Chemistry A 116 (2012) 1519-1526.
[2-12] G. Jian, L. Zhou, N.W. Piekiel, M.R. Zachariah, Low Effective Activation Energies for Oxygen Release from Metal Oxides: Evidence for Mass-Transfer Limits at High Heating Rates, Chemphyschem 15 (2014) 1666-1672.
[2-13] M.A. Hiskey, N. Goldman, J.R. Stine, High-nitrogen energetic materials derived from azotetrazolate, Journal of Energetic Materials 16 (1998) 119-127.
[2-14] E. Zhuravlev, C. Schick, Fast scanning power compensated differential scanning nano-calorimeter: 1. The device, Thermochimica Acta 505 (2010) 1-13.
[2-15] C. Baldasseroni, D.R. Queen, D.W. Cooke, K. Maize, A. Shakouri, F. Hellman, Heat transfer simulation and thermal measurements of microfabricated x-ray transparent heater stages, Review of Scientific Instruments 82 (2011) 093904.
[2-16] S.L. Lai, J.Y. Guo, V. Petrova, G. Ramanath, L.H. Allen, Size-dependent melting properties of small tin particles Nanocalorimetric measurements, Physical Review Letters 77 (1996) 99-102.
[2-17] V.H. Carreto-Vazquez, A.K. Wojcik, Y.S. Liu, D.B. Bukur, M.S. Mannan, Miniaturized calorimeter for thermal screening of energetic materials, Microelectronics Journal 41 (2010) 874-881.
[2-18] F. Yi, I.K. Kim, S. Li, D.A. LaVan, Hydrated/Dehydrated Lipid Phase Transitions Measured Using Nanocalorimetry, Journal of Pharmaceutical Science 103 (2014) 3442-3447.
[2-19] F. Yi, D.A. LaVan, Nanoscale thermal analysis for nanomedicine by nanocalorimetry, Wiley interdisciplinary reviews. Nanomedicine and nanobiotechnology 4 (2012) 31-41.
[2-20] G. Jian, N.W. Piekiel, M.R. Zachariah, Time-Resolved Mass Spectrometry of Nano-Al and Nano-Al/CuO Thermite under Rapid Heating: A Mechanistic Study, The Journal of Physical Chemistry C 116 (2012) 26881-26887.
[2-21] P. Swaminathan, B.G. Burke, A.E. Holness, B. Wilthan, L. Hanssen, T.P. Weihs, D.A. LaVan, Optical calibration for nanocalorimeter measurements, Thermochimica Acta 522 (2011) 60-65.
[2-22] F. Yi, D.A. LaVan, Electrospray-assisted nanocalorimetry measurements, Thermochimica Acta 569 (2013) 1-7.
[2-23] A.I. Lesnikovich, O.A. Ivashkevich, S.V. Levchik, A.I. Balabanovich, P.N. Gaponik, A.A. Kulak, Thermal Decomposition of Aminotetrazoles, Thermochimica Acta 388 (2002) 233-251.

[2-24] V.V. Boldyrev, Thermal decomposition of ammonium perchlorate, Thermochimica Acta 443 (2006) 1-36.
[2-25] I. Adanez-Rubio, P. Gayan, A. Abad, F. Garcia-Labiano, L.F. de Diego, J. Adanez, Kinetic analysis of a Cu-based oxygen carrier: Relevance of temperature and oxygen partial pressure on reduction and oxidation reactions rates in Chemical Looping with Oxygen Uncoupling (CLOU), Chem. Eng. J. 256 (2014) 69-84.
[2-26] N.J. Podraza, B.D. Gauntt, M.A. Motyka, E.C. Dickey, M.W. Horn, Electrical and optical properties of sputtered amorphous vanadium oxide thin films, Journal of Applied Physics 111 (2012) 9.
[2-27] D.R. Miller, S.A. Akbar, P.A. Morris, Nanoscale metal oxide-based heterojunctions for gas sensing: A review, Sens. Actuator B-Chem. 204 (2014) 250-272.
[2-28] D.W. Lee, B.R. Yoo, Advanced metal oxide (supported) catalysts: Synthesis and applications, J. Ind. Eng. Chem. 20 (2014) 3947-3959.
[2-29] S. Mansour, Thermoanalytical Investigations of Decomposition Course of Copper Oxysalts. 1. Basic Copper Carbonate, Journal of Thermal Analysis 42 (1994) 1251-1263.
[2-30] G. Jian, L. Zhou, N.W. Piekiel, M.R. Zachariah, Low effective activation energies for oxygen release from metal oxides: evidence for mass-transfer limits at high heating rates, Chemphyschem : a European journal of chemical physics and physical chemistry 15 (2014) 1666-1672.
[2-31] F. Yi, W. Osborn, J. Betz, D.A. LaVan, Interactions of Adhesion Materials and Annealing Environment on Resistance and Stability of MEMS Platinum Heaters and Temperature Sensors, Journal of Microelectromechanical Systems 10.1109/JMEMS.2015.2394483 (2015).
[2-32] K. Willeke, P.A. Baron, Aerosol Measurement: Principles Techniques and Applications, Van Nostrand Reinhold, 115 Fifth AvenueNew York, NY 10003, 1993.
[3-1] E.L. Dreizin, Metal-based reactive nanomaterials, Progress in Energy and Combustion Science 35 (2009) 141-167.
[3-2] N.H. Yen, L.Y. Wang, Reactive Metals in Explosives, Propellants Explosives Pyrotechnics 37 (2012) 143-155.
[3-3] L.L. Wang, Z.A. Munir, Y.M. Maximov, Thermite Reactions - Their Utilization In The Synthesis And Processing Of Materials, Journal of Materials Science 28 (1993) 3693-3708.
[3-4] M.R. Weismiller, J.Y. Malchi, J.G. Lee, R.A. Yetter, T.J. Foley, Effects of fuel and oxidizer particle dimensions on the propagation of aluminum containing thermites, Proceedings of the Combustion Institute 33 (2011) 1989-1996.
[3-5] S. Chowdhury, K. Sullivan, N. Piekiel, L. Zhou, M.R. Zachariah, Diffusive vs Explosive Reaction at the Nanoscale, Journal of Physical Chemistry C 114 (2010) 9191-9195.
[3-6] V.I. Levitas, Burn time of aluminum nanoparticles: Strong effect of the heating rate and melt-dispersion mechanism, Combustion and Flame 156 (2009) 543-546.
[3-7] M.A. Trunov, M. Schoenitz, E.L. Dreizin, Effect of polymorphic phase transformations in alumina layer on ignition of aluminium particles, Combustion Theory and Modelling 10 (2006) 603-623.
[3-8] V. Baijot, D.-R. Mehdi, C. Rossi, A. Esteve, A multi-phase micro-kinetic model for simulating aluminum based thermite reactions, Combustion and Flame 180 (2017) 10-19.

[3-9] K.T. Sullivan, N.W. Piekiel, C. Wu, S. Chowdhury, S.T. Kelly, T.C. Hufnagel, K. Fezzaa, M.R. Zachariah, Reactive sintering: An important component in the combustion of nanocomposite thermites, Combust. Flame 159 (2012) 2-15.
[3-10] A. Rai, K. Park, L. Zhou, M.R. Zachariah, Understanding the mechanism of aluminium nanoparticle oxidation, Combustion Theory and Modelling 10 (2006) 843-859.
[3-11] G. Jian, S. Chowdhury, K. Sullivan, M.R. Zachariah, Nanothermite reactions: Is gas phase oxygen generation from the oxygen carrier an essential prerequisite to ignition?, Combust. Flame 160 (2013) 432-437.
[3-12] V.I. Levitas, B.W. Asay, S.F. Son, M. Pantoya, Melt dispersion mechanism for fast reaction of nanothermites, Applied Physics Letters 89 (2006).
[3-13] W. Zhou, J.B. DeLisio, X. Wang, G.C. Egan, M.R. Zachariah, Evaluating free vs bound oxygen on ignition of nano-aluminum based energetics leads to a critical reaction rate criterion, Journal of Applied Physics 118 (2015).
[3-14] G.C. Egan, K.T. Sullivan, T. LaGrange, B.W. Reed, M.R. Zachariah, In situ imaging of ultra-fast loss of nanostructure in nanoparticle aggregates, Journal of Applied Physics 115 (2014).
[3-15] G.C. Egan, T. LaGrange, M.R. Zachariah, Time-Resolved Nanosecond Imaging of Nanoscale Condensed Phase Reaction, Journal of Physical Chemistry C 119 (2015) 2792-2797.
[3-16] E.L. Dreizin, Phase changes in metal combustion, Progress in Energy and Combustion Science 26 (2000) 57-78.
[3-17] D.A. Firmansyah, T. Kim, S. Kim, K. Sullivan, M.R. Zachariah, D. Lee, Crystalline Phase Reduction of Cuprous Oxide (Cu2O) Nanoparticles Accompanied by a Morphology Change during Ethanol-Assisted Spray Pyrolysis, Langmuir 25 (2009) 7063-7071.
[3-18] N. Kim, J.F. Stebbins, Structure of Amorphous Tantalum Oxide and Titania-Doped Tantala: O-17 NMR Results for Sol-Gel and Ion-Beam-Sputtered Materials, Chemistry of Materials 23 (2011) 3460-3465.
[3-19] J.D. Kuntz, O.G. Cervantes, A.E. Gash, Z.A. Munir, Tantalum-tungsten oxide thermite composites prepared by sol-gel synthesis and spark plasma sintering, Combustion and Flame 157 (2010) 1566-1571.
[3-20] O.G. Cervantes, J.D. Kuntz, A.E. Gash, Z.A. Munir, Heat of combustion of tantalum-tungsten oxide thermite composites, Combustion and Flame 157 (2010) 2326-2332.
[3-21] O.G. Cervantes, J.D. Kuntz, A.E. Gash, Z.A. Munir, Activation energy of tantalum-tungsten oxide thermite reactions, Combustion and Flame 158 (2011) 117-122.
[3-22] L. Zhou, N. Piekiel, S. Chowdhury, M.R. Zachariah, T-Jump/time-of-flight mass spectrometry for time-resolved analysis of energetic materials, Rapid Commun. Mass Spectrom. 23 (2009) 194-202.
[3-23] G. Jian, N.W. Piekiel, M.R. Zachariah, Time-Resolved Mass Spectrometry of Nano-Al and Nano-Al/CuO Thermite under Rapid Heating: A Mechanistic Study, J. Phys. Chem. C 116 (2012) 26881-26887.
[3-24] K. Sullivan, M.R. Zachariah, Simultaneous Pressure and Optical Measurements of Nanoaluminum Thermites: Investigating the Reaction Mechanism, Journal of Propulsion and Power 26 (2010) 467-472.

[3-25] G. Levesque, P. Vitello, W.M. Howard, Hot-spot contributions in shocked high explosives from mesoscale ignition models, Journal of Applied Physics 113 (2013).
[3-26] V.B. Voitovich, V.A. Lavrenko, V.M. Adejev, E.I. Golovko, HIGH-Temperature Oxidation Of Tantalum Of Different Purity, Oxidation of Metals 43 (1995) 509-526.
[3-27] B.E. Deal, A.S. Grove, GENERAL RELATIONSHIP FOR THERMAL OXIDATION OF SILICON, Journal of Applied Physics 36 (1965) 3770-&.
[3-28] R. Nakamura, T. Toda, S. Tsukui, M. Tane, M. Ishimaru, T. Suzuki, H. Nakajima, Diffusion of oxygen in amorphous Al2O3, Ta2O5, and Nb2O5, Journal of Applied Physics 116 (2014).
[3-29] R.J. Jacob, G.Q. Jian, P.M. Guerieri, M.R. Zachariah, Energy release pathways in nanothermites follow through the condensed state, Combustion and Flame 162 (2015) 258-264.
[3-30] A. Jain, O. Shyue Ping, G. Hautier, W. Chen, W.D. Richards, S. Dacek, S. Cholia, D. Gunter, D. Skinner, G. Ceder, K.A. Persson, Commentary: The Materials Project: A materials genome approach to accelerating materials innovation, Apl Materials 1 (2013).
[3-31] S.P. Ong, L. Wang, B. Kang, G. Ceder, Li-Fe-P-O-2 phase diagram from first principles calculations, Chemistry of Materials 20 (2008) 1798-1807.
[3-32] A. Jain, G. Hautier, S.P. Ong, C.J. Moore, C.C. Fischer, K.A. Persson, G. Ceder, Formation enthalpies by mixing GGA and GGA plus U calculations, Physical Review B 84 (2011).
[3-33] Y.C. Zong, R.J. Jacob, S.Q. Li, M.R. Zachariah, Size Resolved High Temperature Oxidation Kinetics of Nano-Sized Titanium and Zirconium Particles, Journal of Physical Chemistry A 119 (2015) 6171-6178.
[4-1] P.M. Guerieri, S. DeCarlo, B. Eichhorn, T. Connell, R.A. Yetter, X. Tang, Z. Hicks, K.H. Bowen, M.R. Zachariah, Journal of Physical Chemistry A 119 (2015) 11084.
[4-2] E.L. Dreizin, Progress in Energy and Combustion Science 35 (2009) 141.
[4-3] R.A. Yetter, G.A. Risha, S.F. Son, Proceedings of the Combustion Institute 32 (2009) 1819.
[4-4] C.E. Aumann, G.L. Skofronick, J.A. Martin, Journal of Vacuum Science & Technology B 13 (1995) 1178.
[4-5] J.M. Lightstone, C. Stoltz, R.M. Wilson, J. Horn, J. Hooper, D. Mayo, B. Eichhorn, K. Bowen, M.G. White, 7th Biennial Conference of the American-Physical-Society-Topical-Group on Shock Compression of Condensed Matter. Amer Inst Physics, Chicago, IL, 2011.
[4-6] K.S. Williams, J.P. Hooper, Journal of Physical Chemistry A 115 (2011) 14100.
[4-7] S. Alnemrat, J.P. Hooper, 18th Joint Int Conf of the APS Topical-Grp on Shock Compress of Condensed Matter / 24th Int Conf of the Int-Assoc-for-the-Advancement-of-High-Pressure-Sci-and-Technol. Iop Publishing Ltd, Seattle, WA, 2013.
[4-8] S. Alnemrat, J.P. Hooper, Journal of Chemical Physics 141 (2014) 7.
[4-9] S. Alnemrat, J.P. Hooper, Journal of Chemical Physics 140 (2014) 7.
[4-10] M. Schoenitz, S. Umbrajkar, E.L. Dreizin, Journal of Propulsion and Power 23 (2007) 683.
[4-11] S.M. Umbrajkar, M. Schoenitz, E.L. Dreizin, Thermochimica Acta 451 (2006) 34.
[4-12] T.B. Brill, M.C. Beckstead, J.E. Flanagan, M.C. Lin, T.A. Litzinger, R.H.W. Waesche, C.A. Wight, Journal of Propulsion and Power 18 (2002) 824.

[4-13] L. Zhou, N. Piekiel, S. Chowdhury, M.R. Zachariah, Rapid Commun. Mass Spectrom. 23 (2009) 194.
[4-14] L. Zhou, N. Piekiel, S. Chowdhury, M.R. Zachariah, Journal of Physical Chemistry C 114 (2010) 14269.
[4-15] G. Jian, L. Zhou, N.W. Piekiel, M.R. Zachariah, Chem. Phys. Processes Combust. (2011) 126.
[4-16] G. Jian, N.W. Piekiel, M.R. Zachariah, J. Phys. Chem. C 116 (2012) 26881.
[4-17] G. Jian, S. Chowdhury, K. Sullivan, M.R. Zachariah, Combust. Flame 160 (2013) 432.
[4-18] G. Jian, L. Zhou, N.W. Piekiel, M.R. Zachariah, Chemphyschem 15 (2014) 1666.
[4-19] P.L. Timms, Accounts of Chemical Research 6 (1973) 118.
[4-20] M. Tacke, H. Schnoeckel, Inorg. Chem. 28 (1989) 2895.
[4-21] M. Mocker, C. Robl, H. Schnoeckel, Angew. Chem. 106 (1994) 1860.
[4-22] G. Jian, J. Feng, R.J. Jacob, G.C. Egan, M.R. Zachariah, Angew. Chem., Int. Ed. 52 (2013) 9743.
[4-23] S.E. Stein, " Mass Spectra" in NIST Chemistry WebBook, NIST Standard Reference Database Number 69, Eds. P.J. Linstrom and W.G. Mallard, National Institute of Standards and Technology, Gaithersburg MD, 20899, http://webbook.nist.gov, (retrieved March 28, 2016).
[4-24] N.W. Piekiel, L. Zhou, K.T. Sullivan, S. Chowdhury, G.C. Egan, M.R. Zachariah, Combustion Science and Technology 186 (2014) 1209.
[5-1] A. Pivkina, P. Ulyanova, Y. Frolov, S. Zavyalov, J. Schoonman, Nanomaterials for heterogeneous combustion, Propellants Explosives Pyrotechnics 29 (2004) 39-48.
[5-2] E.L. Dreizin, Metal-based reactive nanomaterials, Progress in Energy and Combustion Science 35 (2009) 141-167.
[5-3] A. Rai, K. Park, L. Zhou, M.R. Zachariah, Understanding the mechanism of aluminium nanoparticle oxidation, Combustion Theory and Modelling 10 (2006) 843-859.
[5-4] C. Dohmeier, D. Loos, H. Schnockel, Aluminum(I) and gallium(I) compounds: Syntheses, structures, and reactions, Angewandte Chemie-International Edition in English 35 (1996) 129-149.
[5-5] P.M. Guerieri, S. DeCarlo, B. Eichhorn, T. Connell, R.A. Yetter, X. Tang, Z. Hicks, K.H. Bowen, M.R. Zachariah, Molecular Aluminum Additive for Burn Enhancement of Hydrocarbon Fuels, Journal of Physical Chemistry A 119 (2015) 11084-11093.
[5-6] J.B. DeLisio, D.H. Mayo, P.M. Guerieri, S. DeCarlo, R. Ives, K. Bowen, B.W. Eichhorn, M.R. Zachariah, Oxidation and decomposition mechanisms of air sensitive aluminum clusters at high heating rates, Chem. Phys. Lett. 661 (2016) 168-172.
[5-7] S. Schulz, T. Schoop, H.W. Roesky, L. Haming, A. Steiner, R. Herbstirmer, Synthesis and structure of organometallic compounds with (Al2Si)(2) and Al3Sb2 frameworks, Angewandte Chemie-International Edition in English 34 (1995) 919-920.
[5-8] C.M. Cui, H.W. Roesky, H.G. Schmidt, M. Noltemeyer, H.J. Hao, F. Cimpoesu, Synthesis and structure of a monomeric aluminum(I) compound {HC(CMeNAr)(2)}Al (Ar=2,6-iPr(2)C(6)H(3)): A stable aluminum analogue of a carbene, Angewandte Chemie-International Edition 39 (2000) 4274-+.

[5-9] C. Ganesamoorthy, S. Loerke, C. Gemel, P. Jerabek, M. Winter, G. Frenking, R.A. Fischer, Reductive elimination: a pathway to low-valent aluminium species, Chemical Communications 49 (2013) 2858-2860.
[5-10] G. Jian, S. Chowdhury, K. Sullivan, M.R. Zachariah, Nanothermite reactions: Is gas phase oxygen generation from the oxygen carrier an essential prerequisite to ignition?, Combust. Flame 160 (2013) 432-437.
[5-11] L. Zhou, N. Piekiel, S. Chowdhury, M.R. Zachariah, T-Jump/time-of-flight mass spectrometry for time-resolved analysis of energetic materials, Rapid Commun. Mass Spectrom. 23 (2009) 194-202.
[5-12] L. Zhou, N. Piekiel, S. Chowdhury, M.R. Zachariah, Time-Resolved Mass Spectrometry of the Exothermic Reaction between Nanoaluminum and Metal Oxides: The Role of Oxygen Release, Journal of Physical Chemistry C 114 (2010) 14269-14275.
[6-1] E.L. Dreizin, Metal-based reactive nanomaterials, Progress in Energy and Combustion Science 35 (2009) 141-167.
[6-2] A.S. Rogachev, A.S. Mukasyan, Combustion of heterogeneous nanostructural systems (Review), Combustion Explosion and Shock Waves 46 (2010) 243-266.
[6-3] R.A. Yetter, G.A. Risha, S.F. Son, Metal particle combustion and nanotechnology, Proceedings of the Combustion Institute 32 (2009) 1819-1838.
[6-4] K.J. Blobaum, M.E. Reiss, J.M.P. Lawrence, T.P. Weihs, Deposition and characterization of a self-propagating CuOx/Al thermite reaction in a multilayer foil geometry, Journal of Applied Physics 94 (2003) 2915-2922.
[6-5] M. Petrantoni, C. Rossi, L. Salvagnac, V. Conedera, A. Esteve, C. Tenailleau, P. Alphonse, Y.J. Chabal, Multilayered Al/CuO thermite formation by reactive magnetron sputtering: Nano versus micro, Journal of Applied Physics 108 (2010).
[6-6] C. Rossi, K. Zhang, D. Esteve, P. Alphonse, P. Tailhades, C. Vahlas, Nanoenergetic materials for MEMS: a review, J. Microelectromech. Syst. 16 (2007) 919-931.
[6-7] K. Zhang, C. Rossi, G.A.A. Rodriguez, C. Tenailleau, P. Alphonse, Development of a nano-Al/CuO based energetic material on silicon substrate, Applied Physics Letters 91 (2007).
[6-8] G.A.A. Rodriguez, S. Suhard, C. Rossi, D. Esteve, P. Fau, S. Sabo-Etienne, A.F. Mingotaud, M. Mauzac, B. Chaudret, A microactuator based on the decomposition of an energetic material for disposable lab-on-chip applications: fabrication and test, Journal of Micromechanics and Microengineering 19 (2009).
[6-9] Y.Q. Fu, H.J. Du, W.M. Huang, S. Zhang, M. Hu, TiNi-based thin films in MEMS applications: a review, Sensors and Actuators a-Physical 112 (2004) 395-408.
[6-10] C. Rossi, D. Esteve, Micropyrotechnics, a new technology for making energetic microsystems: review and prospective - Review, Sensors and Actuators a-Physical 120 (2005) 297-310.
[6-11] M. Bahrami, G. Taton, V. Conedera, L. Salvagnac, C. Tenailleau, P. Alphonse, C. Rossi, Magnetron Sputtered Al-CuO Nanolaminates: Effect of Stoichiometry and Layers Thickness on Energy Release and Burning Rate, Propellants Explosives Pyrotechnics 39 (2014) 365-373.
[6-12] G.C. Egan, E.J. Mily, J.P. Maria, M.R. Zachariah, Probing the Reaction Dynamics of Thermite Nanolaminates, Journal of Physical Chemistry C 119 (2015) 20401-20408.

[6-13] C. Michaelsen, K. Barmak, T.P. Weihs, Investigating the thermodynamics and kinetics of thin film reactions by differential scanning calorimetry, Journal of Physics D-Applied Physics 30 (1997) 3167-3186.
[6-14] J. Kwon, J.M. Ducere, P. Alphonse, M. Bahrami, M. Petrantoni, J.F. Veyan, C. Tenailleau, A. Esteve, C. Rossi, Y.J. Chabal, Interfacial Chemistry in Al/CuO Reactive Nanomaterial and Its Role in Exothermic Reaction, Acs Applied Materials & Interfaces 5 (2013) 605-613.
[6-15] F. Yi, D.A. LaVan, Electrospray-assisted nanocalorimetry measurements, Thermochim. Acta 569 (2013) 1-7.
[6-16] F. Yi, J.B. DeLisio, M.R. Zachariah, D.A. LaVan, Nanocalorimetry-Coupled Time-of-Flight Mass Spectrometry: Identifying Evolved Species during High-Rate Thermal Measurements, Analytical Chemistry 87 (2015) 9740-9744.
[6-17] P. Swaminathan, B.G. Burke, A.E. Holness, B. Wilthan, L. Hanssen, T.P. Weihs, D.A. LaVan, Optical calibration for nanocalorimeter measurements, Thermochimica Acta 522 (2011) 60-65.
[6-18] P. Swaminathan, D.A. LaVan, T.P. Weihs, Dynamics of solidification in Al thin films measured using a nanocalorimeter, Journal of Applied Physics 110 (2011) 6.
[6-19] L. Zhou, N. Piekiel, S. Chowdhury, M.R. Zachariah, T-Jump/time-of-flight mass spectrometry for time-resolved analysis of energetic materials, Rapid Commun. Mass Spectrom. 23 (2009) 194-202.
[6-20] G. Jian, N.W. Piekiel, M.R. Zachariah, Time-Resolved Mass Spectrometry of Nano-Al and Nano-Al/CuO Thermite under Rapid Heating: A Mechanistic Study, J. Phys. Chem. C 116 (2012) 26881-26887.
[7-1] K.S. Mulage, R.N. Patkar, V.D. Deuskar, S.M. Pundlik, S.D. Kakade, M. Gupta, Studies on a novel thermoplastic polyurethane as a binder for extruded composite propellants, Journal of Energetic Materials 25 (2007) 233-245.
[7-2] L. Meda, G. Marra, L. Galfetti, S. Inchingalo, F. Severini, L. De Luca, Nano-composites for rocket solid propellants, Compos. Sci. Technol. 65 (2005) 769-773.
[7-3] R.M. Shankar, T.K. Roy, T. Jana, Terminal Functionalized Hydroxyl-Terminated Polybutadiene: An Energetic Binder for Propellant, Journal of Applied Polymer Science 114 (2009) 732-741.
[7-4] N.W. Piekiel, C.J. Morris, L.J. Currano, D.M. Lunking, B. Isaacson, W.A. Churaman, Enhancement of on-chip combustion via nanoporous silicon microchannels, Combustion and Flame 161 (2014) 1417-1424.
[7-5] K.T. Sullivan, C. Zhu, E.B. Duoss, A.E. Gash, D.B. Kolesky, J.D. Kuntz, J.A. Lewis, C.M. Spadaccini, Controlling Material Reactivity Using Architecture, Advanced Materials 28 (2016) 1934-+.
[7-6] M. Dole, H.L. Cox, J. Gieniec, Electrospray Mass-Spectroscopy, Advances in Chemistry Series (1973) 73-84.
[7-7] M.S. Wilm, M. Mann, Electrospray And Taylor-Cone Theory, Doles Beam Of Macromolecules At Last, International Journal of Mass Spectrometry 136 (1994) 167-180.
[7-8] S. Yan, G. Jian, M.R. Zachariah, Electrospun Nanofiber-Based Thermite Textiles and their Reactive Properties, ACS Appl. Mater. Interfaces 4 (2012) 6432-6435.

[7-9] Z.-M. Huang, Y.Z. Zhang, M. Kotaki, S. Ramakrishna, A review on polymer nanofibers by electrospinning and their applications in nanocomposites, Composites Science and Technology 63 (2003) 2223-2253.
[7-10] H. Wang, G. Jian, S. Yan, J.B. DeLisio, C. Huang, M.R. Zachariah, Electrospray Formation of Gelled Nano-Aluminum Microspheres with Superior Reactivity, ACS Appl. Mater. Interfaces 5 (2013) 6797-6801.
[7-11] H. Wang, J.B. DeLisio, G. Jian, W. Zhou, M.R. Zachariah, Electrospray formation and combustion characteristics of iodine-containing Al/CuO nanothermite microparticles, Combustion and Flame 162 (2015) 2823-2829.
[7-12] C. Huang, G. Jian, J.B. DeLisio, H. Wang, M.R. Zachariah, Electrospray Deposition of Energetic Polymer Nanocomposites with High Mass Particle Loadings: A Prelude to 3D Printing of Rocket Motors, Advanced Engineering Materials 17 (2015) 95-101.
[7-13] X.L. Hu, J.B. DeLisio, X.Y. Li, W.B. Zhou, M.R. Zachariah, Direct Deposit of Highly Reactive Bi(IO3)(3)- Polyvinylidene Fluoride Biocidal Energetic Composite and its Reactive Properties, Advanced Engineering Materials 19 (2017).
[7-14] P.M. Guerieri, J.B. DeLisio, M.R. Zachariah, Nanoaluminum/Nitrocellulose microparticle additive for burn enhancement of liquid fuels, Combustion and Flame 176 (2017) 220-228.
[7-15] G. Young, H.Y. Wang, M.R. Zachariah, Application of Nano-Aluminum/Nitrocellulose Mesoparticles in Composite Solid Rocket Propellants, Propellants Explosives Pyrotechnics 40 (2015) 413-418.
[7-16] W. Zhou, M.W. Orr, G. Jian, S.K. Watt, V.T. Lee, M.R. Zachariah, Inactivation of bacterial spores subjected to sub-second thermal stress, Chemical Engineering Journal 279 (2015) 578-588.
[7-17] K.T. Sullivan, C.W. Wu, N.W. Piekiel, K. Gaskell, M.R. Zachariah, Synthesis and reactivity of nano-Ag2O as an oxidizer for energetic systems yielding antimicrobial products, Combustion and Flame 160 (2013) 438-446.
[7-18] W.B. Zhou, M.W. Orr, V.T. Lee, M.R. Zachariah, Synergistic effects of ultrafast heating and gaseous chlorine on the neutralization of bacterial spores, Chemical Engineering Science 144 (2016) 39-47.
[7-19] H. Wang, G. Jian, G.C. Egan, M.R. Zachariah, Assembly and reactive properties of Al/CuO based nanothermite microparticles, Combust. Flame 161 (2014) 2203-2208.
[8-1] A. Pivkina, P. Ulyanova, Y. Frolov, S. Zavyalov, J. Schoonman, Nanomaterials for heterogeneous combustion, Propellants Explosives Pyrotechnics 29 (2004) 39-48.
[8-2] E.L. Dreizin, Metal-based reactive nanomaterials, Progress in Energy and Combustion Science 35 (2009) 141-167.
[8-3] N.S. Cohen, R.W. Fleming, R.L. Derr, ROLE OF BINDERS IN SOLID-PROPELLANT COMBUSTION, Aiaa Journal 12 (1974) 212-218.
[8-4] K.S. Mulage, R.N. Patkar, V.D. Deuskar, S.M. Pundlik, S.D. Kakade, M. Gupta, Studies on a novel thermoplastic polyurethane as a binder for extruded composite propellants, Journal of Energetic Materials 25 (2007) 233-245.
[8-5] N. Kubota, C. Serizawa, Combustion process of magnesium/polytetrafluoroethylene pyrotechnics, Propellants, Explos., Pyrotech. 12 (1987) 145-148.
[8-6] E.-C. Koch, Metal-fluorocarbon-pyrolants: III. Development and application of magnesium/teflon/viton (MTV), Propellants, Explos., Pyrotech. 27 (2002) 262-266.

[8-7] D.T. Osborne, M.L. Pantoya, Effect of al particle size on the thermal degradation of Al/Teflon mixtures, Combustion Science and Technology 179 (2007) 1467-1480.
[8-8] M.L. Pantoya, S.W. Dean, The influence of alumina passivation on nano-Al/Teflon reactions, Thermochimica Acta 493 (2009) 109-110.
[8-9] C. Huang, G. Jian, J.B. DeLisio, H. Wang, M.R. Zachariah, Electrospray Deposition of Energetic Polymer Nanocomposites with High Mass Particle Loadings: A Prelude to 3D Printing of Rocket Motors, Adv. Eng. Mater. 17 (2015) 95-101.
[8-10] X. Li, P. Guerieri, W. Zhou, C. Huang, R. Zachariah Michael, Direct deposit laminate nanocomposites with enhanced propellent properties, ACS Appl Mater Interfaces 7 (2015) 9103-9109.
[8-11] J. McCollum, M.L. Pantoya, S.T. Iacono, Activating Aluminum Reactivity with Fluoropolymer Coatings for Improved Energetic Composite Combustion, Acs Applied Materials & Interfaces 7 (2015) 18742-18749.
[8-12] O. Mulamba, M. Pantoya, Exothermic surface reactions in alumina-aluminum shell-core nanoparticles with iodine oxide decomposition fragments, J. Nanopart. Res. 16 (2014) 2310/2311-2310/2319, 2319 pp.
[8-13] M.A. Hobosyan, K.G. Kirakosyan, S.L. Kharatyan, K.S. Martirosyan, PTFE-Al2O3 reactive interaction at high heating rates, J. Therm. Anal. Calorim. 119 (2015) 245-251.
[8-14] L. Zhou, N. Piekiel, S. Chowdhury, M.R. Zachariah, T-Jump/time-of-flight mass spectrometry for time-resolved analysis of energetic materials, Rapid Commun. Mass Spectrom. 23 (2009) 194-202.
[8-15] O. Mulamba, M.L. Pantoya, Exothermic surface chemistry on aluminum particles promoting reactivity, Applied Surface Science 315 (2014) 90-94.
[8-16] S. Zulfiqar, M. Zulfiqar, M. Rizvi, A. Munir, I.C. McNeill, Study of the thermal degradation of poly(chlorotrifluoroethylene), poly(vinylidene fluoride) and copolymers of chlorotrifluoroethylene and vinylidene fluoride, Polym. Degrad. Stab. 43 (1994) 423-430.
[8-17] Z. Sarbak, Effect of fluoride and sodium ions on structural and thermal properties of gamma-Al2O3, Crystal Research and Technology 32 (1997) 491-497.
[8-18] S. Zhang, E.L. Dreizin, Reaction Interface for Heterogeneous Oxidation of Aluminum Powders, Journal of Physical Chemistry C 117 (2013) 14025-14031.
[8-19] A. Rai, K. Park, L. Zhou, M.R. Zachariah, Understanding the mechanism of aluminium nanoparticle oxidation, Combustion Theory and Modelling 10 (2006) 843-859.
[9-1] A. Pivkina, P. Ulyanova, Y. Frolov, S. Zavyalov, J. Schoonman, Nanomaterials for Heterogeneous Combustion. Propellants, Explos., Pyrotech. 2004, 29, 39−48.
[9-2] N. S. Cohen, R. W. Fleming, R. L. Derr, Role of Binders in Solid-Propellant Combustion, AIAA J. 1974, 12, 212−218.
[9-3] X. Li, P. Guerieri, P. Zhou, W. Huang, M.R. Zachariah, Direct Deposit Laminate Nano-Composites with Enhanced Propellent Properties, ACS Applied Materials & Interfaces 7, 9103 (2015)
[9-4] DeLisio, X.Hu, T.Wu, G. Egan, G.Young and M.R. Zachariah, Probing the Reaction Mechanism of Aluminum/poly(vinylidene fluoride) Composites, J. Physical Chem. B 120, 5534 (2016)
[9-5] http://www.rmjordan.com/reflectron-tof.html , Date Accessed: 2/27/2017

[9-6] H. Wang, J. Delisio, G. Jian, W. Zhou and M.R. Zachariah, Electrospray Formation and Combustion Characteristics of Iodine-Containing Al/CuO Nanothermite Microparticles, Combustion and Flame 162, 2823 (2015)
[9-7] H. Wang, Zachariah Research Group, University of Maryland, Work in Preparation
[9-8] S-H. Kim, B. Liu and M.R. Zachariah, Synthesis of Nanoporous Metal Oxide Particles by a New Inorganic Filler Spray Pyrolysis Method, Chemistry of Materials 4(7), 2889-2899 (2002)
[9-9] J. Fernandez, J. F. de la Mora, J. Navascues, F. Fernandez, J. Rosell-Llompart, Generation of Submicron Monodisperse Aerosols in Electrosprays. J. Aerosol. Sci. 1990, 21, S673−S676
[9-10] Nils Hansen, Terrill A. Cool, Phillip R. Westmoreland, Karthina Kohse-Höinghaus, Recent contributions of flame-sampling molecular beam mass spectrometry to a fundamental understanding of combustion chemistry, Progress in Energy and Combustion Science 35 (2009) 168-191
[9-11] Wei Chen, William L. Hase, and H. Bernhard Schlegel, Ab Initio MO Calculations of the Thermochemistry of BX, AlX, OBX, and OAlX (X=O, F, Cl), Gas-Phase Metal Reactions, Elsevier Science Publishers B.V., 1992 pp. 179-187.